ISSN 1694-7398
journals.manas.edu.kg

JUNE 2025
Volume 13, Issue 1

MANAS JOURNAL OF ENGINEERING

MJEN

BISHKEK 2025

KYRGYZ TURKISH MANAS UNIVERSITY
MANAS JOURNAL OF ENGINEERING (MJEN)

ISSN: 1694- 7398
Year: 2025
Volume: 13
Special Issue: 1
http://journals.manas.edu.kg
journals@manas.edu.kg

PUBLICATION PERIOD

Manas Journal of Engineering (MJEN) is published twice year, MJEN is a peer reviewed journal.

CORRESPONDENCE ADDRESS
Kyrgyz Turkish Manas University
Chyngyz Aitmatov Avenue 56 Bishkek, KYRGYZSTAN
URL: http://journals.manas.edu.kg
e-mail: journals@manas.edu.kg
Tel : +996 312 492763- Fax: +996 312 541935

KYRGYZ TURKISH MANAS UNIVERSITY
MANAS JOURNAL OF ENGINEERING (MJEN)

ISSN: 1694- 7398
Year: 2025
Volume: 13
Special Issue: 1
http://journals.manas.edu.kg
journals@manas.edu.kg

CONTENT

Corrigendum

Turgut Hanoymak, Ömer Küsmüş	*A glance at blockchain technology and cryptocurrencies as an application*	*1*

Research article

Güzide Pekcan, Tuğba Karaca Erol, Hayrettin Bulum	*Analysis of the binary mixtures of amlodipine and atorvastatin by chemometric-spectophotometric method*	*2-7*
Süleyman Senyurt, Davut Canlı, Kebire Hilal Ayvacı	*Ruled Surfaces with Bishop vectors via Smarandache geometry*	*8-17*
Muhammad Lawan Kaurangini, Umar Muhammad Abubakar, Enes Ata	*Generalized Pathway Fractional Integral Formulas Involving Extended Multi-Index Mittag-Leffler Function in Kernel of SUM Transform*	*18-22*
Ahmet Bulut, Ümit Tayfun, Mehmet Yurderi	*Experimental characterization of thermal, mechanical, physical and morphological performance of thermoplastic polyurethane composites containing acidic pumice*	*23-29*
Yener ALTUN	*An investigation into the asymptotic stability analysis of delayed q-fractional neutral systems*	*30-39*
Aysegul Yagmur Goren	*An atmospheric impact assessment of water-based hydrogen production methods: Sustainability evaluation*	*40-51*
Nawid Ahmad Akhtar, Mehmet Kobya	*Efficient degradation of phenol by electrooxidation process at boron-doped diamond anode system*	*52-63*
Muhammet Kaan Yeşilyurt Mansur Mustafaoğlu	*A Numerical Analysis of the Effect of Corrugated Surface Profile on Heat Transfer in Turbulent Flow Through a Rectangular Mini-Channel*	*64-78*

MANAS Journal of Engineering
ISSN 1694-7398 | e-ISSN 1694-7398

Volume 13, Issue 1, (20215) Pages - 1

Corrigendum

Corrigendum to 'A glance at blockchain technology and cryptocurrencies as an application'

Turgut Hanoymak[1,*], Ömer Küsmüş[2]

[1] Van Yüzüncü Yıl University, Van, Turkey, hturgut@yyu.edu.tr, ORCID: 0000-0002-3822-2202
[2] Van Yüzüncü Yıl University, Van, Turkey, omerkusmus@yyu.edu.tr, ORCID: 0000-0001-7397-0735

ABSTRACT

This corrigendum note provides a clarification regarding the correction of a citation error in one of our previously published articles entitled 'A glance at blockchain technology and cryptocurrencies as an application'.

In the article entitled "A Glance at Blockchain Technology and Cryptocurrencies as an Application", published in Volume 10, Issue 1 (2022) of Manas Journal of Engineering, a citation was inadvertently omitted due to an unintentional oversight during the peer-review and/or publication process. With this corrigendum, we formally acknowledge and cite the source

[21]. Güven V., Şahinöz E., Blokzincir- Kripto Paralar-Bitcoin: Satoshi Dünyayı Değiştiriyor, Kronik Kitabevi, 5., 2020.
Particularly in relation to the content presented in Table 1 and Table 2. We sincerely apologize for this unintentional omission and any inconvenience it may have caused.

MANAS Journal of Engineering
ISSN 1694-7398 | e-ISSN 1694-7398

Volume 13, Issue 1, (2025) Pages 2-7
https://doi.org/10.51354/mjen.1389474

Analysis of the binary mixtures of amlodipine and atorvastatin by chemometric-spectophotometric method

Güzide Pekcan[1,*], Tuğba Karaca Erol[2], Hayrettin Bulum[3]

[1] Suleyman Demirel University, Faculty of Engineering and Natural Science, Isparta, Turkiye, guzideertokus@sdu.edu.tr, ORCID: 0000-0001-9230-5634
[2] Suleyman Demirel University, Faculty of Engineering and Natural Science, Isparta, Turkiye, tugbakaraca32@gmail.com, ORCID: 0000-0001-5065-2531
[3] Suleyman Demirel University, Faculty of Engineering and Natural Science, Isparta, Turkiye, hayrettinbulum@hotmail.com, ORCID: 0000-0001-9841-2473

ABSTRACT

In this study, the simultaneous quantification of amlodipine and atorvastatin in pharmaceutical preparations was successfully accomplished without the need for a separation process by using chemometric calibration methods (principal component analysis method (PCA), principal component regression method (PCR), and partial least squares method (PLS). Additionally, chemometric evaluation was performed on the data obtained from UV visible field spectroscopy methods. 16 mixes containing the chemicals atorvastatin and amlodipine were created as a calibration (concentration) set to assess the validity of the designated chemometric procedures. The calibration set's absorption spectrum was captured between 200 and 500 nm. The link between the calibration set and the absorption data collected in the 215–355 nm region was used to produce three chemometric calibrations. Amlodipine and atorvastatin synthetic mixtures were analyzed to assess the validity of the PCA, PCR, and PLS approaches. The percentage (%) recovery average for atorvastatin and amlodipine was determined for both the drug sample and the synthetic mixture using the approach we used. It was discovered that the computed values were fairly high.The methodologies were controlled, and the ANOVA test was run using the results of the PLS and PCR calibration techniques. The enhanced technique might be suggested for the examination of medication samples containing atorvastatin and amlodipine since it is among the most sensitive, accurate, and repeatable techniques available.

ARTICLE INFO

Research article

Received: 11/11/2023
Accepted: 12/03/2025

Keywords:
amlodipine,
atorvastatin,
chemometry

**Corresponding author*

1. Introduction

One definition of high blood pressure is hypertension, or high blood pressure. A person with hypertension has a systolic blood pressure of 140 mmHg and a diastolic blood pressure of 90 mmHg or higher.Hypertension is described as the usage of antihypertensive medications.Hypertension is linked to cardiac problems, kidney function, and stroke.It is also possible to see disorders [1].

Amplodipine (AML) belongs to the dihydropyridine class of calcium channel blockers (Figure 1.1). It blocks the smooth muscle cell membrane's and myocardium's calcium channels from allowing calcium ions to enter the cell. AML targets smooth muscle cells specifically. AML reduces peripheral resistance and systemic blood pressure by depressing peripheral carterioles and blocking transmembrane calcium flow. After oral administration, AML is well absorbed, reaching peak plasma concentrations in 6–12 hours [2].

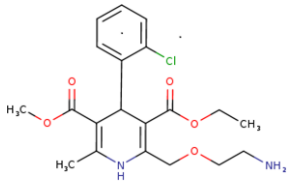

Figure 1. *Chemical Structure of Amlodipine*

The chemical formula of the active ingredient atorvastatin is [R-(R*, R*)]. -2-(4-fluorophenyl)-β, δ-dihydroxy-5-(1-methylethyl) -3-phenyl-4-[(phenylamino)carbonyl] 1-Hpyrrole-1-heptanoic acid, Atorvastatin [3] is a 3-hydroxy-3-methylglutaryl-coenzyme A (HMG-CoA) reductase inhibitor. This enzyme catalyzes HMG-CoA conversion through an early and rate-limiting step in cholesterol biosynthesis. Atorvastatin has been used to reduce low-density lipoprotein (LDL) cholesterol, total cholesterol, apo-B, triglyceride levels, and C-reactive protein and increase lipoprotein levels.

Atorvastatin is used along with weight loss, diet, and exercise to reduce the risk of heart attack, heart disease, stroke, and the likelihood of developing heart disease [4].

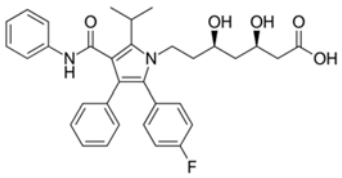

Figure 2. *Chemical Structure of Atorvasvatin*

Spectrophotometric techniques are frequently employed for the simultaneous measurement of several compounds in mixtures. It is claimed that the approach is affordable and that the outcomes are exact and accurate [5]. The two most popular chemometric techniques are principal component regression (PCR) and partial least squares regression (PLS) [6]. These techniques are widely acknowledged for the examination of pharmaceutical goods with many components [7].

In this study, chemometric determinations of cholesterol drugs were made by evaluating spectrophotometric data. The method used chemometrically is the Partial Least Squares Method (PLS). The method applied by chemometry has been given sensitivity, and both active drug substances can be analyzed next to each other without any preliminary separation. The data obtained from the method were evaluated analytically as statistical (RSD, LOD, LOQ, PRESS, SEC, RMSEC) in order to express the data more meaningfully and with higher quality.

2. Aim and method

In this study, drugs used to hypertension were evaluated in terms of UV/VIS spectrophotometric and chemometric aspects. Chemometric analysis was performed to evaluate the results. The UV 1700 Pharmaspec Shimadzu (Shimadzu, Kyoto, Japan) device was used for UV measurements in the analysis. In the first step, single spectra of substances were taken, and then the appropriate synthetic mixture was examined in the tablet sample prepared in certain proportions. Finally, measurements of commercially purchased drug tablets (Caduet) were taken. In chemometric calculations, the Minitab 17 program [8] (Inova Consulting) was used.

In this study, spectra of amlodipine, atorvastatin, and systematically prepared synthetic mixtures were taken by spectrophotometric measurements, first in single form and then in a ratio identical to the drug mixture. As a final procedure, measurements were made on the drug tablet sample obtained from the pharmacy. The spectrophotomerically collected data were calculated and evaluated by different multivariate calibration methods. In the first step, the calibration (resetting process) of the UV spectrophotometer device was performed. The calibration process was first performed against the air by leaving both cells blank. Then, the same process was done by placing a blind sample prepared with our solvent that we used in both light paths. In all readings, the blind is always prepared in this way. In order to eliminate the interference effects while choosing the blind, the blind solvent was preferred. In the last step, the commercial tablet (Caduet) is examined. While preparing the drug sample, all the tablets included in the package are crushed in an agate mortar, thinned and mixed. Weighing the weight of a tablet, it is dissolved in solvent, mixed in a magnetic stirrer to homogenize and absorbance reading is performed.

3. Findings and application

3.1. Absorption Spectra of Amlodipine and Atorvastatin Drug Active Ingredients

100 µg/mL (ppm) solutions were prepared by using 0.1 M methanol as solvent in 25 mg/250 mL of amlodipine and atorvastatin active ingredients. In the next stage, the solutions prepared to analyze the spectroscopic properties of each substance were prepared in the range of 5-50 µg/mL for each substance. The wavelength at which the active ingredients amlodipine and atorvastatin give the maximum spectrum (amplodipine: 237 nm; atorvastatin: 247 nm) was determined (Figure 3. and 4.)

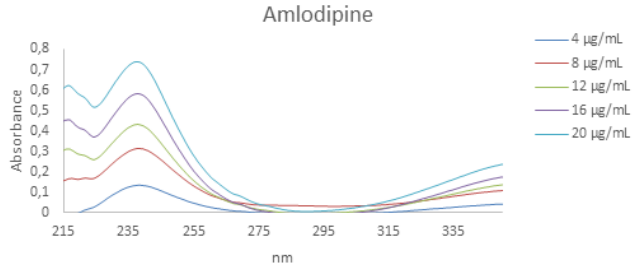

Figure 3. *Absorption spectrum of amplodipine active ingredient in the range of 4-20 µg/mL*

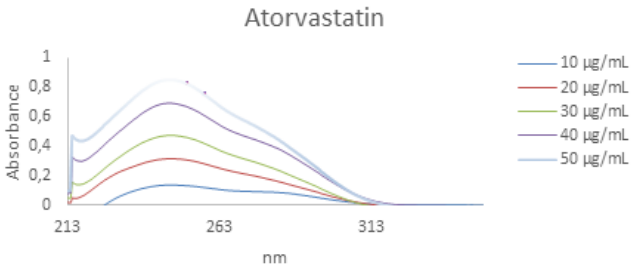

Figure 4. *Absorption spectrum of atorvastatin active ingredient in the range of 10-50 µg/mL*

The absorbance value rises with increasing concentration, as can be seen by examining the absorbance-wavelength graphs for atorvastatin and amlodipine.

Amlodipine and Atorvastatin were prepared in the range of 5-50 µg/mL (Table 1.) in 16 synthetic mixture solutions.

Table 1. *Calibration set with Amlodipine and Atorvastatin*

	Atorvastatin µg/mL	Amplodipine µg/mL
1	10	5
2	20	10
3	30	15
4	40	20
5	50	25
6	10	5
7	20	10
8	30	15
9	40	20
10	50	25
11	10	5
12	20	10
13	30	15
14	40	20
15	50	25
16	10	5

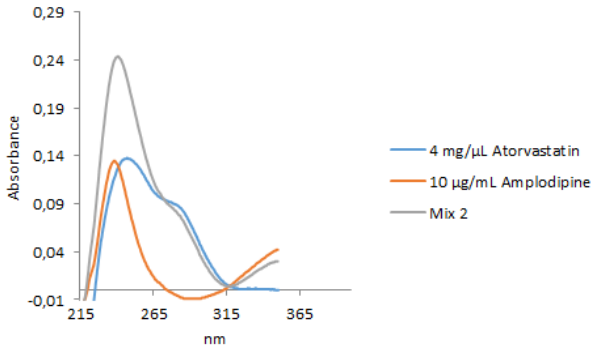

Figure 5. *Absorption-wavelength graph of the synthetic mixture containing amlodipine and atorvastatin.*

UV spectroscopy was used to determine the absorbance values of these combination solutions (Figure 5). The chemometry method was then used to analyze the obtained data. Chemometric calculations are the most widely used, dependable, and expedient techniques for figuring out how much of each component is present in multicomponent mixtures. The idea behind the relationship between absorbance and concentration is that when the principal component is analyzed using the regression approach, the absorbance values measured for the concentration set can be broken down into orthogonal lines. The computations are predicated on the correctness of these lines, which represent the coordinate order of the calibration that needs to be established [9].

In this study, partial least squares method (PLS) and principal component regression (PCR) were used as chemometric methods. The correlation matrix created with the help of the principal components obtained by principal component analysis guides other chemometric regressions. Among the chemometric methods, the methods used in this study are partial least squares method (PLS) and principal component regression (PCR) [10,11, 12,13].

Table 2. *Results calculated by principal component regression of each substance in the mixture containing Amlodipine and Atorvastatin.*

	Atorvastatin			**Amplodipine**		
No	Added (ppm)	Found (ppm)	Recovery %	Added (ppm)	Found (ppm)	Recovery %
1	10	9.95	99.50	5	4.97	99.4
2	20	19.92	99.60	10	9.89	98.9
3	30	29.87	99.57	15	14.79	98.6
4	40	38.97	97.43	20	19.97	99.85
5	50	49.98	99.96	25	24.69	98.76
6	10	9.05	90.50	5	4.95	99
7	20	19.88	99.40	10	9.89	98.9
8	30	29.96	99.87	15	14.97	99.8
9	40	39.95	99.88	20	19.94	99.7
10	50	49.86	99.72	25	24.45	97.8
11	10	9.97	99.70	5	5.01	100.2
12	20	18.96	94.80	10	9.97	99.7
13	30	29.95	99.83	15	14.96	99.73
14	40	39.97	99.93	20	19.98	99.9
15	50	48.99	97.98	25	24.98	99.92
16	10	9.67	96.70	5	4.97	99.4
			Mean=98.40			Mean=99.35
			% RSD=0.026			%RSD=0.063

Table 3. *Results calculated by the method of partial least squares of each substance in the mixture containing Amlodipine and Atorvastatin.*

	Atorvastatin			Amplodipine		
No	Added (ppm)	Found (ppm)	Recovery %	Added (ppm)	Found (ppm)	Recovery %
1	10	9.89	98.9	5	5.01	100.20
2	20	20.02	100.1	10	9.94	99.40
3	30	28.99	96.63	15	15.04	100.27
4	40	39.87	99.68	20	19.96	99.80
5	50	49.56	99.12	25	24.88	99.52
6	10	9.94	99.4	5	4.97	99.40
7	20	19.47	97.35	10	9.97	99.70
8	30	29.86	99.53	15	14.98	99.87
9	40	39.97	99.93	20	19.92	99.60
10	50	49.81	99.62	25	24.89	99.56
11	10	9.98	99.8	5	4.97	99.40
12	20	19.97	99.85	10	9.89	98.90
13	30	30.01	100.03	15	14.99	99.93
14	40	39.95	99.88	20	19.87	99.35
15	50	49.98	99.96	25	24.92	99.68
16	10	9.98	98.90	5	5.05	101.00
			Mean=99.35			Mean=99.72
			%RSD=0.01			%RSD=0.048

3.2. Chemometric Approaches

To validate calibrations for drug mixes that are synthetic, certain statistical factors were added. Tables 2, 3, and 4 display the recovery and relative standard deviation (rsd) values that were determined for each chemometric method 1. To avoid inaccuracies in the drug sample, the cross-validation process was used while the concentrations versus the additional concentrations were determined [14,15].

The ICH criteria [16,17,18] were followed in the validation process of the chemometric approach with regards to linearity, accuracy, intraday and interday precision, limit of detection, and limit of quantitation. For calibration, the following formula was used to forecast the residual error sum-of-squares (PRESS) and standard error of prediction (SEC) (Table 4) based on the actual and anticipated concentrations of the samples:

$$PRESS = \sum_{i=1}^{n} \left(C_i^{added} - C_i^{found} \right)^2 \quad (1)$$

where C_i^{added} – actual concentration, the added concentration of the drug; C_i^{found} : predicted concentration, the calculated concentration of the drug.

$$SEC = \sqrt{\frac{\sum_{i=1}^{n} (C_i^{added} - C_i^{found})^2}{n-1}} \quad (2)$$

where n – the total number of synthetic mixtures.

Another validation parameter is RMSEC [19]. It is given in the below equation 3.

$$RMSEC = \sqrt{PRESS/n} \quad (3)$$

The equations of the observable limit (LOD) and detection limit (LOQ) parameters are shown below. These expressions are interrelated but have different equations (equation 4 and 5) [20].

$$LOD = 3Sa/m \quad (4)$$
$$LOQ = 10Sa/m \quad (5)$$

m: Slope

LOQ> LOD and LOQ = LOD were taken into consideration while evaluating the calculated LOD values [21].

Table 4. *Calculated Analytical Parameters*

Parameters	Method	Atorvastatin	Amplodipine
λ_{max} (nm)		247.0 nm	237.0 nm
Correlation Coefficient (R^2)		0.9997	0.9997
SEC	PLS	0.059	0.020
	PCR	0.106	0.036
PRESS	PLS	0.099	0.0051
	PCR	0.280	0.032
RMSEC	PLS	0.081	0.019
	PCR	0.136	0.046
LOD (µg/mL)	PLS	0.512	0.083
	PCR	0.789	0.240
LOQ(µg/mL)	PLS	1.552	0.251
	PCR	2.390	0.719

Table 5. *PLS and PCR techniques were used to extract the pharmaceutical formulation's paracetamol and amoxicillin contents.*

	Atorvastatin (gram)	
NO	PLS	PCR
1	9.89	9.98
2	9.91	9.95
3	9.97	9.89
4	9.92	10.01
5	9.85	9.94
Mean±SD*	9.908±0.004	9.954±0.005

	Amplodipine (gram)	
NO	**PLS**	**PCR**
1	4.97	5.01
2	4.89	4.96
3	4.95	4.92
4	4.82	4.97
5	4.86	4.90
Mean±SD*	4.898±0.0013	0.4952±0.009

4. Conclusion

In this study, the data obtained by UV spectrophotometry were calculated using multivariate calibration methods. Thus, theoretical and experimental calculations were evaluated together. Considering the calculations, a quantitative determination of the active ingredients of atorvastatin and amplodipine in the drug sample obtained from the pharmacy was made.

Individual UV spectra for the recognition of the active ingredients atorvastatin and amplodipine primarily Below. In the next stage, the spectrum was obtained by preparing a synthetic mixture identical to the drug sample obtained from the pharmacy. For atorvastatin and amplodipine, using the chemometric method (PCR and PLS), the method was calculated statistically.

The recovery values were acceptably large, and the standard deviations were calculated in accordance with the study. In the establishment of PLS and PCR calibrations for the quantification of these substances in mixtures containing binary drug substances, the sum of the squares of the predicted errors in the cross-validation process (Predicted Resudiual Error Some of Squares→ PRESS) and the standard error of calibration (SEC) values close to zero increase the accuracy and reliability. It has been observed that the PRESS and SEC values are small enough, or even close to zero. LOQ values are also small compared to LOD values.

The methods developed are reproducible, have high sensitivity and accuracy, produce fast results, and can be recommended for the analysis of different drug samples containing atorvastatin and amplodipine.

Acknowledgements

This research work has been supported by research grants from Suleyman Demirel University Scientific Research Project FYL-2021-8323.

References

[1]. Kalan M.K., "Hipertansiyon Hastalarında Antihipertansif İlaç Değişimleri, Bu Değişimlerin Nedenleri ve İlaç Değişimleri ile Hedef Tedavi Değerlerine Ulaşma Oranlarının İncelenmesi". Sağlık Bakanlığı Şişli Etfal Eğitim ve Araştırma Hastanesi Aile Hekimliği Koordinatörlüğü, Uzmanlık Tezi, İstanbul, 2007, pp.98.

[2]. Yılmaz N., "Amlodipin ve Rosuvastatin Etkin Maddelerinin Farmasötik Preparatlarda Kare Dalga Voltametri Yöntemi ile Aynı Anda Miktar Tayini". Atatürk Üniversitesi Sağlık Bilimleri Enstitüsü, Yüksek Lisans Tezi, Erzurum, 2018, pp. 2-3.

[3]. Tomikj M., Božinovska, Anevska-Stojanovska N., Lazova J., Acevska J., Brezovska K., Tonich-Ribarska J., Nakov N., "Sustainable and white HPLC method for simultaneous determination of amlodipine and atorvastatin in film-coated tablet",Green Analytical Chemistry, 8, 100103.

[4]. Reid I.O.A., Mohamed M.E., "Chemometric Simultaneous Determination of Atorvastatin and Amlodipine in Bulk and Tablets", International Journal Pharmacy and Chemistry, 5(4), (2019), 42-47.

[5]. Mansour F.R, "A New Innovative Spectrophotometric Method For The Simultaneous Determination of Sofosbuvir and Ledipasvir". Spectrochimica Acta Part A:Molecular and Biomolecular Spectroscopy 18(188), (2018), 626-632.

[6]. Dinç E., Baleanu D., "Spectrophotometric Quantitative Determination of Cilazapril and Hydrochlorothiazide in Tablets By Chemometric Methods". J. Pharmaceut. Biomed, 30, (2002), 715-723.

[7]. Kenneth R, Chemometrics: A practical Guide. John Wiley & Sons. Inc., New York, 1997.

[8]. "Minitab 17 Statistical Programme" http://www.inovadanismanlik.com.tr (06.11.2023).

[9]. Dinç E., , "Kemometrik İşlem ve Yöntemlerin Analitik Kimyadaki Tipik Uygulamaları", Uygulamalı Kemometri Yaz Okulu Notları, 2009, pp. 13-17.

[10]. Dinç E., Baleanu D., " Spectrophotometric quantitative determination of cilazapril and hydrochlorothiazide in tablets by chemometric methods" Journal of pharmaceutical and biomedical analysis, 30, (2002), 715-723.

[11]. Dinç E., ,Özdemir, A., Baleanu, D., "Comparative study of the continuous wavelent transform, derivative and partial least squares methods applied to the overlapping spectra for the simultaneous quantitative resolution of ascorbic acid and asetilsalicylic acid in effervescent tablets, Journal of pharmaceutical and biomedical analysis, 37, (2005), 715-723.

[12]. Ustündağ, O., & Dinç, E., "Simultaneous resolution of a binary mixture of captopril and hydrochlorothiazide in tablets by bivariate and multivariate spectral calibrations". Die Pharmazie, 58 (9), (2003), 623-8 .

[13]. Dinç, E., Ustündağ, O., & Baleanu, D. (2010). "Simultaneous chemometric determination of pyridoxine hydrochloride and isoniazid in tablets by

multivariate regression methods“.. *Drug testing and analysis*, 2 (8), (2010), 383-387.

[14]. Porfire A, Muntean D, Achim M, Vlase L, Tomuta, I, “Simultaneous Quantification of Simvastatin and Excipients in Liposomes Using Near Infrared Spectroscopy and Chemometry”. Journal of Pharmaceutical and Biomedical Analysis 107, (2015), 40-49.

[15]. Tarhan I, Kara AAIH, “Quantitative Determination of Free Fatty Acids in Extra Virgin Olive Oils by Multivariate Methods and Fourier Transform Infrared Spectroscopy Considering Different Absorption Modes”. International Journal of Food Properties (2017), 1-8.

[16]. Abbai N, Parameswari SA, “Stability Indicating RP-HPLC Method Development and Validation for Simultaneous Estimation od Salbutamol and Beclomethasone in Bulk and Tablet Dosage Form”, IJPSR 9(5), (2009), 1980-1988.

[17]. Aravind D, Kamarapu SK, “Method Development and Validation of RP-HPLC Method for Simultaneous Estimation of Clidinium Bromide, Chlordiazepoxide and Dicylomine Hydrochloride in Bulk and Combined Tablet Dosage Forms”, IJPBS 3(3), (2013), 152-161.

[18]. Deshpande P, Mandawad V, “Development and Validation of Stability Indicating HPTLC Method for Determination of Azelastine Hydrochloride as Bulk Drug and in Pharmaceutical Liquid Dosage Form”, IAJPS 05(06), (2018), 5107-5113.

[19]. Bilgili AV, Çullu MA, Aydemir S, “Tuzdan Etkilenmiş Toprakların Yakın Kızılötesi Yansıma Spektroradyometre ve Elektromanyetik Indüksiyon Tekniği Yardımıyla Karakterize Edilebilme Potansiyelinin Araştırılması”. Harran Tarım ve Gıda Bilimleri Dergisi 18(1), (2014), 32-45.

[20]. Shrivastava A, Gupta VB, “Methods For The Determination of Limit of Detection and Limit of Quantitation of The Analytical Methods”. Chronicles of Young Scientist 2(1), (2011), 21-25.

[21]. Armbruster DA, Pty T, “Limit of Blank, Limit of Detection and Limit of Quantitation”. Clin. Niochem Rev. 29, (2008), 49-52.

MANAS Journal of Engineering
ISSN 1694-7398 — e-ISSN 1694-7398

Volume 13 (Issue 1) (2025) Pages 8-17
https://doi.org/10.51354/mjen.1440372

Ruled Surfaces with Bishop vectors via Smarandache geometry

Süleyman Şenyurt[1], Davut Canlı [2,*], Kebire Hilal Ayvacı[3]
[1]Ordu University, Ordu, Türkiye, senyurtsuleyman52@gmail.com, ORCID: 0000-0003-1097-5541,
[2]Ordu University, Ordu, Türkiye, davutcanli@odu.edu.tr, ORCID: 0000-0003-0405-9969,
[2]Ordu University, Ordu, Türkiye, hilal.ayvaci55@gmail.com, ORCID: 0000-0002-5114-5475

ABSTRACT

The objective of the present study is to examine the novel ruled surfaces that are generated by Bishop frame vectors through the conceptual framework of Smarandache geometry. The fundamental forms and the associated curvatures were determined for each ruled surface, thereby establishing its developability and minimality characteristics. Furthermore, the properties of the base curve and the corresponding striction curves of each surface were discussed through asymptoticity, geodesicity, and principal line. It has been observed that the characteristics of certain constructed ruled surfaces are directly influenced by a ruled surface designed by Bishop vectors of a slant helix-like curve.

ARTICLE INFO

Research article

Received: 20.02.2024
Accepted: 17.06.2025

Keywords: Bishop frame, Smarandache ruled surfaces, fundamental forms, mean and Gaussian curvatures, developable and minimal surfaces

**Corresponding author*

1. Introduction

Ruled surfaces are engaged to a broader range of areas such as engineering, computational constructions, architectural structures, computer graphics, works of art, textile, automobile industry, etc. Since they are mostly referred in computer aided geometric designs (CAGDs) to deal with real world problems and to model the real objects, introducing new ruled surfaces generated by different methods will lead new potentials to the related fields. Providing their characteristics may also enable easy adaptations for interested researchers. The basic theory on ruled surfaces is discussed in many differential geometry textbooks such as [1–4]. Generalization of ruled surfaces can however, be found in [5]. Moreover, some properties of the ruled surfaces with Frenet frame of a non-cylindrical ruled surface were investigated in [6]. The characteristics for the ruled surfaces according to Bishop frame ([7]) were examined in [8] and in [9], separately, whereas the main properties of ruled surfaces according to alternative frame were studied in [10]. Sannia frame based ruled surfaces were studied in [11] while quasi ruled surfaces were defined and examined in [12]

Recently, a new notion for generating new ruled surfaces has been given in [13] by taking the advantage of the idea of Smarandache geometry which was introduced in [14, 15]. By assigning the base curve as one of the Smarandache curves and assigning the other vector element of Frenet frame as ruling, the new ruled surfaces are named as the Smarandache ruled surfaces according to Frenet frame. The same method of generating such ruled surfaces is applied to the Darboux frame in [16], and according to the alternative frame in [17]. In [18–20], new ruled surfaces are examined and their characteristics are discussed by benefiting the similar techniques.

In this study, the novel concept of Smarandache ruled surfaces according to the Bishop frame was examined. Subsequently, certain characteristics were outlined, including developability and minimality, under the specified conditions. Furthermore, the constraints that a curve be asymptotic, geodesic, or principal line on each surface

were investigated. Finally, the research was supported by the presentation of illustrative graphs of corresponding Smarandache ruled surfaces.

2. Preliminaries

This section reviews some fundamental concepts that are referenced throughout the paper.
Let $\gamma : R \to R^3$ be a regular *unit speed* curve in three dimensional Euclidean space and denote $\{T,\ N,\ B\}$ as the Frenet frame and $\{T,\ N_1,\ N_2\}$ as the Bishop frame of γ. Then, the corresponding Frenet and Bishop formulae are given as

$$\begin{array}{ll} T' = \kappa N & T' = k_1 N_1 + k_2 N_2 \\ N' = -\kappa T + \tau B, & {N_1}' = -k_1 T, \\ B' = -\tau N & {N_2}' = -k_2 T \end{array} \tag{2.1}$$

where $'$ stands for the derivative with respect to the arc length parameter s. The relations among the components and the curvatures of two frames are given as:

$$\begin{aligned} T &= \gamma', \\ N &= cos\theta N_1 + sin\theta N_2, \\ B &= -sin\theta N_1 + cos\theta N_2, \end{aligned} \tag{2.2}$$

and

$$\begin{aligned} &k_1 = \kappa cos\theta, \qquad k_2 = \kappa sin\theta, \qquad \kappa = \sqrt{k_1^2 + k_2^2}, \\ &\theta = arctan\left(\frac{k_2}{k_1}\right), \qquad \tau = \theta'. \end{aligned} \tag{2.3}$$

On the other hand, a surface is said to be ruled if it is formed with a straight line $X(s)$ that moves along the curve $\gamma(s)$. The parametric representation for a ruled surface is given by the following:

$$\chi(s, v) = \gamma(s) + vX(s), \tag{2.4}$$

where $\gamma(s)$ is the base curve, whereas $X(s)$ is the generator (ruling). The unit normal vector field of $\chi = \chi(s, v)$ is computed as

$$n_\chi = \frac{\chi_s \times \chi_v}{\|\chi_s \times \chi_v\|}, \tag{2.5}$$

where χ_s and χ_v are the partial derivatives of χ with respect to s and v, respectively. The striction curve of the ruled surface χ is defined to be as

$$\bar{\gamma} = \gamma - \frac{\langle \gamma', X' \rangle}{\|X'\|^2} X. \tag{2.6}$$

Moreover, the first and second fundamental forms are defined by

$$\begin{aligned} I &= Eds^2 + 2Fdsdv + Gdv^2, \\ II &= Lds^2 + 2Mdsdv + Ndv^2, \end{aligned} \tag{2.7}$$

where the corresponding coefficients are

$$\begin{array}{lll} E = \langle \chi_s, \chi_s \rangle, & \mathrm{F} = \langle \chi_s, \chi_v \rangle, & \mathrm{G} = \langle \chi_v, \chi_v \rangle, \\ L = \langle \chi_{ss}, n \rangle, & \mathrm{M} = \langle \chi_{sv}, n \rangle, & \mathrm{N} = \langle \chi_{vv}, n \rangle. \end{array} \tag{2.8}$$

Regarding to the given coefficients, the Gaussian K and the mean H curvatures for a ruled surface are defined by

$$K = -\frac{M^2}{EG - F^2}, \qquad H = \frac{LG - 2MF}{2(EG - F^2)}, \tag{2.9}$$

respectively. In relation to the Gaussian and mean curvatures, the following proposition exists:

Proposition 2.1 *([1–3]) A surface is developable (resp., minimal), if the Gaussian (resp., mean) curvature vanishes.*

Furthermore, the normal curvature, the geodesic curvature and the geodesic torsion of a ruled surface $\chi(s, v)$ are defined as:

$$\begin{array}{ll} \kappa_n = \langle \gamma'', n_\chi \rangle, & \kappa_g = \langle n_\chi \times T, T' \rangle, \\ \tau_g = \langle n_\chi \times {n_\chi}', T' \rangle, & \end{array} \tag{2.10}$$

respectively. According to the given relations above, the following propositions exist for the ruled surface $\chi(s, v)$:

Proposition 2.2 *([1–3])*

- *The curve γ is an asymptotic line on the surface χ, if the normal curvature κ_n vanishes,*
- *The curve γ is a geodesic on the surface χ, if the geodesic curvature κ_g vanishes,*
- *The curve γ is a principal line on the surface χ, if the geodesic torsion τ_g vanishes.*

The following theorem is also needed since it is referred on characterization of the constructed surface in the next sections:

Theorem 2.1 *([8, 21]) If N_1 has a constant angle with a fixed unit vector, then the curve γ is said to be a slant helix. Correspondingly, γ is a slant helix if and only if $\frac{k_1}{k_2} = constant$.*

3. Smarandache ruled surfaces according to Bishop frame

In this section, new ruled surfaces will be defined according to Bishop frame by referring to Smarandache geometry. The characteristics for each surface will also be outlined in the context.

3.1. The characteristics of TN_1 Smarandache ruled surface

Definition 3.1 *Let $\gamma(s) : s \in I \subset R \to R^3$ be a unit speed curve in E^3, and denote $\{T(s),\ N_1(s),\ N_2(s)\}$ as the Bishop frame of γ. The ruled surface with base TN_1 Smarandache curve and with ruling N_2 is called a TN_1 Smarandache ruled surface which is defined by*

$$\xi(s,v) = \frac{T(s)+N_1(s)}{\sqrt{2}} + vN_2(s). \tag{3.1}$$

Theorem 3.1 *The Gaussian and mean curvature of the TN_1 ruled surface ξ defined at* (3.1) *are given as*

$$K_\xi = -\frac{1}{2}\left(\frac{k_1k_2}{k_1^2+v^2k_2^2+vk_1k_2\sqrt{2}}\right)^2,$$

and

$$H_\xi = \frac{\left(\begin{array}{c} k_1k_2^2\left(1-2v^2\right)+vk_2\left(k_1'\sqrt{2}-2k_1^2\sqrt{2}\right) \\ -vk_1k_2'\sqrt{2}-2k_1^3 \end{array}\right)}{4\left(k_1^2+v^2k_2^2+vk_1k_2\sqrt{2}\right)^{\frac{3}{2}}},$$

respectively.

Proof By considering the relations given at (2.1) and (2.2), the first and second order partial derivatives of ξ with respect to s and v, results

$$\begin{aligned}
\xi_s =& -\left(\frac{\sqrt{2}}{2}k_1+vk_2\right)T+\frac{\sqrt{2}}{2}k_1N_1+\frac{\sqrt{2}}{2}k_2N_2,\\
\xi_{ss} =& \left(-\frac{\sqrt{2}}{2}\left(\kappa^2+k_1'\right)-vk_2'\right)T\\
&+\left(\frac{\sqrt{2}}{2}k_1'-\left(\frac{\sqrt{2}}{2}k_1+vk_2\right)k_1\right)N_1\\
&+\left(\frac{\sqrt{2}}{2}k_2'-\left(\frac{\sqrt{2}}{2}k_1+v\,k_2\right)k_2\right)N_2,\\
\xi_v =& N_2, \quad \xi_{sv} = -k_2T, \quad \xi_{vv} = 0.
\end{aligned}$$

Thus, from (2.5), the normal vector field of the ruled surface ξ can be given

$$n_\xi = \frac{\sqrt{2}k_1T+(\sqrt{2}k_1+2vk_2)N_1}{2\sqrt{{k_1}^2+v^2{k_2}^2+vk_1k_2\sqrt{2}}}. \tag{3.2}$$

Moreover, from (2.8),

$$\begin{aligned}
E_\xi =& \left(\frac{\sqrt{2}k_1}{2}+vk_2\right)^2+\frac{{k_1}^2+{k_2}^2}{2},\\
F_\xi =& \frac{\sqrt{2}k_2}{2}, \qquad G_\xi = 1,\\
L_\xi =& -\frac{\left(\begin{array}{c} 2k_1vk_2\left(\sqrt{2}k_1+k_2v\right)+v\sqrt{2}\left(k_1k_2'-k_1'k_2\right) \\ +k_1\left(2{k_1}^2+{k_2}^2\right) \end{array}\right)}{2\sqrt{\sqrt{2}k_1vk_2+v^2{k_2}^2+{k_1}^2}},\\
M_\xi =& \frac{-\sqrt{2}k_1k_2}{2\sqrt{\sqrt{2}k_1vk_2+v^2{k_2}^2+{k_1}^2}}, \qquad N_\xi = 0.
\end{aligned}$$

By substituting these coefficients into (2.9), the proof is completed. □

Corollary 3.1 *The TN_1 Smarandache ruled surface is developable if and only if the main curve γ is a planar curve,*

Proof If TN_1 Smarandache ruled surface is developable, then $K_\xi = 0$, that is $k_1k_2 = 0$. If $k_1 = 0$, then from equations (2.3), $\theta = \frac{\pi}{2}k,\ k \in Z$. Similarly, if $k_2 = 0$, then $\theta = \pi k,\ k \in Z$. Since $\tau = \theta'$ and $\theta = constant$ for either case, this gives $\tau = 0$ meaning that γ is a planar curve. □

Corollary 3.2 *The TN_1 Smarandache ruled surface is either minimal or Constant-Mean-Curvature (CMC in short) surface if and only if the curve γ is a planar curve.*

Proof The proof follows the similar steps as of (ii), that is if $k_1 = 0$ then, $H_\xi = 0$, accordingly ξ is minimal, however if $k_2 = 0$, then $H_\xi = -\frac{1}{2}$ which means ξ is a (CMC) surface. □

Theorem 3.2 *The striction curve ς_ξ of the TN_1 Smarandache ruled surface is given as*

$$\zeta_\xi = \frac{T+N_1}{\sqrt{2}} - \frac{k_1k_2}{\sqrt{2}}N_2.$$

Proof The derivatives of the base and the ruling of TN_1 Smarandache ruled surface ξ are

$$\begin{aligned}
\left(\frac{T+N_1}{\sqrt{2}}\right)' &= \frac{1}{\sqrt{2}}\left(-k_1T+k_1N_1+k_2N_2\right),\\
N_2' &= -k_2T.
\end{aligned}$$

From relation (2.6), the proof is completed. □

Theorem 3.3 *The normal curvature, geodesic curvature and the geodesic torsion of the TN_1 Smarandache ruled surface are given in respective order as follows:*

$$\kappa_{n\xi} = \frac{k_1\left(k_2' + {k_1}^2 + k_2k_1 + \left(\sqrt{2}v+1\right){k_2}^2\right) - k_1'\left(k_2\sqrt{2}v + k_1\right)}{2\sqrt{v^2{k_2}^2 + k_1k_2v\sqrt{2} + {k_1}^2}},$$
$$\kappa_{g\xi} = \frac{{k_1}^2\sqrt{2}\left({k_2}^2v\sqrt{2} - k_2'\right) + k_1\sqrt{2}\left(2{k_2}^3 + k_1'k_2\right) + k_2\left(4{k_2}^3v + {k_1}^3\sqrt{2}\right)}{2\left(2{k_2}^2 + {k_1}^2\right)\sqrt{v^2{k_2}^2 + k_1k_2v\sqrt{2} + {k_1}^2}}, \tag{3.3}$$
$$\tau_{g\xi} = \frac{\eta_1\lambda_3\left(\sqrt{2}k_1 + 2k_2v\right) - \eta_3\lambda_1\left(k_1\sqrt{2} + 2k_2v\right) + k_1\sqrt{2}\left(\eta_3\lambda_2 - \lambda_3\eta_2\right)}{2\sqrt{v^2{k_2}^2 + k_1k_2v\sqrt{2} + {k_1}^2}}.$$

Proof

By referring the relations in (2.2), the tangent and the derivative of the tangent vector of TN_1- Smarandache curve are given as

$$T_{TN_1} = \frac{-k_1T + k_1N_1 + k_2N_2}{\sqrt{{k_2}^2 + 2{k_1}^2}}, \tag{3.4}$$
$${T_{TN_1}}' = \eta_1T + \eta_2N_1 + \eta_3N_2$$

where

$$\begin{bmatrix}\eta_1\\ \eta_2\\ \eta_3\end{bmatrix} = \frac{1}{\left({k_2}^2 + 2{k_1}^2\right)^{\frac{3}{2}}}\begin{bmatrix}-{k_2}^2\left({k_2}^2 + 3{k_1}^2\right) - 2{k_1}^4 + k_2\left(k_1k_2' - k_2k_1'\right)\\ -{k_1}^2\left({k_2}^2 + 2{k_1}^2\right) + k_2\left(k_2k_1' - k_1k_2'\right)\\ k_1\left(-{k_2}^3 - 2\left(k_2{k_1}^2 - k_1k_2' + k_2k_1'\right)\right)\end{bmatrix}.$$

□

On the other hand, the second order derivative of TN_1 Smarandache curve results

$$\left(\frac{T+N_1}{\sqrt{2}}\right)'' = \frac{1}{\sqrt{2}}\begin{bmatrix}-{k_1}^2 - {k_2}^2 - k_1'\\ k_1' - {k_1}^2\\ k_2' - k_1k_2\end{bmatrix}\begin{bmatrix}T\\ N_1\\ N_2\end{bmatrix}.$$

Moreover, the derivative of the normal vector field of TN_1 Smarandache ruled surface is:

$$\left(n_\xi\right)' = \lambda_1T + \lambda_2N_1 + \lambda_3N_2,$$

where

$$\begin{bmatrix}\lambda_1\\ \lambda_2\\ \lambda_3\end{bmatrix} = \frac{\begin{bmatrix}k_1'k_2v\left(k_2v\sqrt{2} + k_1\right) - k_1k_2'v\left(k_2\sqrt{2}v + k_1\right) - k_1{k_2}^2v\left(3k_1v\sqrt{2} + 2k_2v^2\right) - {k_1}^3\left(k_1\sqrt{2} + 4k_2v\right)\\ k_1\left(k_1{k_2}^2\sqrt{2}v^2 + 2k_2{k_1}^2v - k_2k_1'v + {k_1}^3\sqrt{2} + k_1k_2'v\right)\\ k_1k_2\sqrt{2}\left(v^2{k_2}^2 + k_1k_2v\sqrt{2} + {k_1}^2\right)\end{bmatrix}}{2\left(v^2{k_2}^2 + k_1k_2v\sqrt{2} + {k_1}^2\right)^{\frac{3}{2}}}.$$

Upon substituting these into (2.10), the proof is completed. According to the Theorem 3.3, the following two corollaries can ve given without the need for proof.

Corollary 3.3

(i) The TN_1 Smarandache curve is asymptotic on TN_1 Smarandache ruled surface if $k_1 = 0$ that is $\theta = \frac{\pi}{2}k,\ k \in Z$.

(ii) The TN_1 Smarandache curve is geodesic on TN_1 Smarandache ruled surface if $k_2 = 0$ that is $\theta = \pi k,\ k \in Z$.

3.2. The characteristics of TN_2 Smarandache ruled surface

Definition 3.2 *Let $\gamma(s) : s \in I \subset R \to R^3$ be a unit speed curve in E^3, and denote $\{T(s),\ N_1(s),\ N_2(s)\}$ as the Bishop frame of γ. The ruled surface with a base TN_2 Smarandache curve and with ruling N_1 is called a TN_2 Smarandache ruled surface which is defined by*

$$\delta(s,v) = \frac{T(s)+N_2(s)}{\sqrt{2}} + vN_1(s). \tag{3.5}$$

Theorem 3.4 *The Gaussian and mean curvature of the TN_2 ruled surface δ defined at (3.5) are given as*

$$K_\delta = -\frac{1}{2}\left(\frac{k_1k_2}{k_2^2+v^2k_1^2+vk_1k_2\sqrt{2}}\right)^2,$$

$$H_\delta = \frac{\left(\begin{array}{c} k_1^2k_2\left(1-2\,v^2\right)+vk_1\left(k_2'\sqrt{2}-2k_2^2\sqrt{2}\right) \\ -vk_1'k_2\sqrt{2}-2k_2^3 \end{array}\right)}{4\left(k_2^2+v^2k_1^2+vk_1k_2\sqrt{2}\right)^{\frac{3}{2}}}.$$

Proof By using (2.1) and (2.2), the first and second order partial derivatives of δ with respect to s and v is computed as follows:

$$\delta_s = -\left(\frac{\sqrt{2}}{2}k_2+vk_1\right)T+\frac{\sqrt{2}}{2}k_1N_1+\frac{\sqrt{2}}{2}k_2N_2,$$

$$\delta_{ss} = \begin{bmatrix} -\frac{\sqrt{2}}{2}\left(\kappa^2+k_2'\right)-vk_1' \\ \frac{\sqrt{2}}{2}k_1'-\left(\frac{\sqrt{2}}{2}k_2+vk_1\right)k_1 \\ \frac{\sqrt{2}}{2}k_2'-\left(\frac{\sqrt{2}}{2}k_2+vk_1\right)k_2 \end{bmatrix}^T \begin{bmatrix} T \\ N_1 \\ N_2 \end{bmatrix}$$

$$\delta_v = N_1, \qquad \delta_{sv} = -k_1T, \qquad \delta_{vv} = 0.$$

Thus, from (2.5), the normal vector field of the ruled surface δ can be given

$$n_\delta = -\frac{\sqrt{2}k_2T+(\sqrt{2}k_2+2vk_1)N_2}{2\sqrt{k_2{}^2+v^2k_1{}^2+vk_1k_2\sqrt{2}}}. \tag{3.6}$$

Moreover, from (2.8),

$$E_\delta = \left(\frac{\sqrt{2}k_2}{2}+vk_1\right)^2+\frac{k_1{}^2+k_2{}^2}{2},$$

$$F_\delta = \frac{\sqrt{2}k_1}{2}, \qquad G_\delta = 1,$$

$$L_\delta = \frac{\left(\begin{array}{c} 2k_2vk_1\left(k_2\sqrt{2}+vk_1\right)-v\sqrt{2}\left(k_2'k_1-k_1'k_2\right) \\ +k_2\left(2k_2{}^2+k_1{}^2\right) \end{array}\right)}{2\sqrt{\sqrt{2}k_2vk_1+v^2k_1{}^2+k_2{}^2}},$$

$$M_\delta = \frac{\sqrt{2}k_2k_1}{2\sqrt{\sqrt{2}k_2vk_1+v^2k_1{}^2+k_2{}^2}}, \qquad N_\delta = 0.$$

By substituting these coefficients into (2.9), the proof is completed. □

From Proposition 2.1 and Theorem 3.4, similar corollaries can be obtained as like below:

Corollary 3.4 *The TN_2 Smarandache ruled surface is developable if and only if the main curve γ is a planar curve,*

Proof The proof is similar as of the proof for Corollary 3.1. □

Corollary 3.5 *The TN_2 Smarandache ruled surface is either minimal or constant-mean-curvature (CMC) surface if and only if the curve γ is a planar curve.*

Proof The proof is slightly different from the proof for Corollary 3.2, that is if $k_2 = 0$, then $H_\delta = 0$, and if $k_1 = 0$, then $H_\delta = \frac{1}{2}$. □

Theorem 3.5 *The striction curve of the TN_2 Smarandache ruled surface is given as*

$$\zeta_\delta = \frac{T+N_2}{\sqrt{2}} - \frac{k_1k_2}{\sqrt{2}}N_1.$$

Proof The derivatives of the base and the ruling of TN_2 Smarandache ruled surface δ are

$$\left(\frac{T+N_2}{\sqrt{2}}\right)' = \frac{\sqrt{2}}{2}\left(-k_2T+k_1N_1+k_2N_2\right),$$

$$N_1' = -k_1T.$$

By considering relation (2.6), the proof is completed. □

Theorem 3.6 *The normal curvature, geodesic curvature and the geodesic torsion of the TN_2 Smarandache ruled surface are given in respective order as follows:*

$$\kappa_{n\,\delta} = \frac{k_1 v\sqrt{2}\left({k_2}^2 - {k_2}'\right) + k_2\left({k_1}^2 + 2{k_2}^2\right)}{2\sqrt{v^2{k_1}^2 + k_2 k_1 v\sqrt{2} + {k_2}^2}},$$

$$\kappa_{g\,\delta} = \frac{2\left({k_1}'k_2 - k_1{k_2}'\right)\left(\sqrt{2}k_2 + k_1 v\right) - k_1 k_2\sqrt{2}\left(2{k_2}^2 + {k_1}^2\right) - 2{k_1}^2 v\left({k_1}^2 + 4{k_2}^2\right)}{2\left(2{k_2}^2 + {k_1}^2\right)\sqrt{k_1 k_2 v\sqrt{2} + v^2{k_1}^2 + {k_2}^2}},$$

$$\tau_{g\,\delta} = \frac{\left(\alpha_2\omega_1 - \alpha_1\omega_2\right)\left(k_2\sqrt{2} + 2k_1 v\right) + k_2\sqrt{2}\left(\alpha_3\omega_2 - \alpha_2\omega_3\right)}{2\sqrt{k_1 k_2 v\sqrt{2} + v^2{k_1}^2 + {k_2}^2}},$$

Proof By using the relations in 2.2, the tangent and the derivative of the tangent vector of TN_2 Smarandache curve are given as

$$\begin{aligned} T_{TN_2} &= \frac{-k_2 T + k_1 N_1 + k_2 N_2}{\sqrt{{k_1}^2 + 2{k_2}^2}}, \\ {T_{TN_2}}' &= \omega_1 T + \omega_2 N_1 + \omega_3 N_2, \end{aligned} \tag{3.7}$$

where

$$\begin{bmatrix} \omega_1 \\ \omega_2 \\ \omega_3 \end{bmatrix} = \frac{1}{\left(2{k_2}^2 + {k_1}^2\right)^{\frac{3}{2}}} \begin{bmatrix} k_1\left({k_1}'k_2 - {k_2}'k_1\right) - 2{k_2}^4 - 3{k_1}^2{k_2}^2 - {k_1}^4 \\ k_2\left(2\left({k_1}'k_2 - {k_2}'k_1\right) - 2{k_2}^2 k_1 - {k_1}^3\right) \\ k_1\left({k_2}'k_1 - {k_1}'k_2\right) - 2{k_2}^4 - {k_1}^2{k_2}^2 \end{bmatrix}.$$

On the other hand, the second order derivative of TN_2 Smarandache curve is

$$\left(\frac{T + N_2}{\sqrt{2}}\right)'' = \frac{1}{\sqrt{2}} \begin{bmatrix} -\left({k_1}^2 + {k_2}^2 + {k_2}'\right) \\ \left({k_1}' - k_1 k_2\right) \\ \left({k_2}' - {k_2}^2\right) \end{bmatrix} \begin{bmatrix} T \\ N_1 \\ N_2 \end{bmatrix}.$$

Lastly, the derivative of the normal vector field of the TN_2 Smarandache ruled surface is given as follows:

$$(n_\delta)' = \alpha_1 T + \alpha_2 N_1 + \alpha_3 N_2,$$

where

$$\begin{bmatrix} \alpha_1 \\ \alpha_2 \\ \alpha_3 \end{bmatrix} = \frac{\begin{bmatrix} \left(\sqrt{2}k_1 v + k_2\right)\left({k_1}'k_2 - k_1 k_2\right)v + {k_1}^2 k_2 v^2\left(3k_2\sqrt{2} + 2k_1 v\right) + {k_2}^3\left(k_2\sqrt{2} + 4k_1 v\right) \\ -k_1 k_2\sqrt{2}\left(k_1 k_2 v\sqrt{2} + v^2{k_1}^2 + {k_2}^2\right) \\ -{k_2}^2\left(\sqrt{2}\left({k_1}^2 v^2 + {k_2}^2\right) + v\left(2k_1 k_2 - k_1 + {k_1}'\right)\right) \end{bmatrix}}{2\left(k_1 k_2 v\sqrt{2} + v^2{k_1}^2 + {k_2}^2\right)^{\frac{3}{2}}}$$

Upon substituted the given relations into (2.10), the proof is completed.

As a result of this theorem, two corollaries can be easily given without the need for proof as follows:

Corollary 3.6

(i) The TN_2 Smarandache curve is asymptotic on TN_2 Smarandache ruled surface if $k_2 = 0$ that is $\theta = \pi k$, $k \in Z$.

(ii) The TN_2 Smarandache curve is geodesic on TN_2 Smaran-

dache ruled surface if $k_1 = 0$ *that is* $\theta = \frac{\pi}{2}k,\ k \in Z$.

3.3. The N_1N_2 Smarandache ruled surface

Definition 3.3 *Let* $\gamma(s) : s \in I \subset R \to R^3$ *be a unit speed curve in* E^3*, and denote* $\{T(s),\ N_1(s),\ N_2(s)\}$ *as the Bishop frame of* γ*. The ruled surface with a base* N_1N_2 *Smarandache curve and with ruling* T *is called a* N_1N_2 *Smarandache ruled surface which is defined by*

$$\varepsilon(s,v) = \frac{N_1(s) + N_2(s)}{\sqrt{2}} + vT(s). \tag{3.8}$$

Theorem 3.7 *The Gaussian curvature of* ε *defined at* (3.8) *vanishes, whereas its mean curvature is given by*

$$H_\varepsilon = \frac{k_1'k_2 - k_1k_2'}{2v\kappa^3}.$$

Proof The first and second order partial derivatives of ε with respect to s and v, from the relations given at (2.1) and (2.2), it is clear to have

$$\varepsilon_s = -\frac{\sqrt{2}}{2}(k_1 + k_2)T + vk_1N_1 + vk_2N_2, \qquad \varepsilon_v = T,$$

$$\varepsilon_{ss} = \begin{bmatrix} -\left(v\kappa^2 + \frac{\sqrt{2}}{2}(k_1' + k_2')\right) \\ \left(vk_1' - \frac{\sqrt{2}}{2}k_1(k_1 + k_2)\right) \\ \left(vk_2' - \frac{\sqrt{2}}{2}k_2(k_1 + k_2)\right) \end{bmatrix} \begin{bmatrix} T \\ N_1 \\ N_2 \end{bmatrix}$$

$$\varepsilon_{sv} = k_1N_1 + k_2N_2, \qquad \varepsilon_{vv} = 0.$$

Thus, from (2.5), the normal vector field of the ruled surface ε can be given

$$n_\varepsilon = \frac{k_2N_1 - k_1N_2}{\kappa}. \tag{3.9}$$

Moreover, from (2.8),

$$E_\varepsilon = \frac{(k_1 + k_2)^2}{2} + v^2\left({k_1}^2 + {k_2}^2\right), \quad F_\varepsilon = -\frac{\sqrt{2}(k_1 + k_2)}{2},$$
$$G_\varepsilon = 1, \quad L_\varepsilon = \frac{v(k_2{k_1}' - k_1{k_2}')}{\sqrt{{k_2}^2 + {k_1}^2}}, \quad M_\varepsilon = N_\varepsilon = 0.$$

By substituting these coefficients into (2.9), the proof is completed. □

Remark 3.1 *From the given proposition 2.1, the* N_1N_2 *Smarandache ruled surface is always developable.*

Proof The proof is clear by given the Proposition 2.1. □

Corollary 3.7 *The* N_1N_2 *Smarandache ruled surface is minimal if and only if the curve* γ *is a slant helix.*

Proof Let us recall the Theorem 2.1 that γ is a slant helix if and only if $\left(\frac{k_1}{k_2}\right)' = 0$. From Theorem 3.7, this corresponds to that $H_\varepsilon = 0$, which means the ruled surface ε is minimal.
Conversely, if ε is minimal ($H_\varepsilon = 0$), then by Theorem 3.7, $k_1'k_2 - k_1k_2' = 0$. Thus, $\frac{k_1}{k_2} = constant$ meaning that γ is a slant helix. □

Theorem 3.8 *The striction curve of the* N_1N_2 *Smarandache ruled surface is given as*

$$\zeta_\varepsilon = \frac{N_1 + N_2}{\sqrt{2}}.$$

The derivatives of the base and the ruling of N_1N_2 Smarandache ruled surface ε are

$$\left(\frac{N_1 + N_2}{\sqrt{2}}\right)' = -\left(\frac{k_1 + k_2}{\sqrt{2}}\right)T,$$
$$T' = k_1N_1 + k_2N_2.$$

By considering relation (2.6), the proof is completed.

Remark 3.2 *Note that the striction curve coincides with the base curve for* N_1N_2 *Smarandache ruled surface.*

Theorem 3.9 *The normal curvature, geodesic curvature and the geodesic torsion of the* N_1N_2 *Smarandache ruled surface is*

$$\kappa_{n\,\varepsilon} = 0, \qquad \kappa_{g\,\varepsilon} = -\kappa, \qquad \tau_{g\,\varepsilon} = 0, \tag{3.10}$$

respectively.

Proof By considering both (2.2) and (2.3), the tangent and the derivative of the tangent vector of N_1N_2 Smarandache curve are given as

$$\begin{aligned} T_{N_1N_2} &= -T, \\ {T_{N_1N_2}}' &= -k_1N_1 - k_2N_2. \end{aligned} \tag{3.11}$$

Moreover, the second order derivative of N_1N_2 Smarandache curve is

$$\left(\frac{N_1 + N_2}{\sqrt{2}}\right)'' = -\frac{\begin{matrix}(k_1' + k_2')T + (k_1^2 + k_1k_2)N_1 \\ + (k_1k_2 + k_2^2)N_2\end{matrix}}{\sqrt{2}}.$$

Lastly, the derivative of the normal vector field of the TN_2 Smarandache ruled surface is given as follows:

$$(n_\varepsilon)' = \frac{k_1(k_1k_2' - k_1'k_2)N_1 + k_2(k_1k_2 - k_1'k_2)N_2}{\kappa^3}.$$

When the given relations substituted into (2.10), the proof is completed. □

The following two corollaries can be expressed as a result of Theorem 3.9 without the need for proof.

Corollary 3.8

(i) The N_1N_2 Smarandache curve is always asymptotic and principal line on N_1N_2 Smarandache ruled surface.

(ii) The geodesic curvature of N_1N_2 Smarandache ruled surface is negative of the curvature of the main curve γ.

Example 3.1 *Let us consider the standard unit helix curve parameterized as*

$$\gamma(s) = \frac{\sqrt{2}}{2}(cos(s), sin(s), s),$$

then, the Frenet curvatures of γ are $\kappa = \tau = \frac{\sqrt{2}}{2}$. Since $\tau = \theta'$, this results $\theta = \int \tau ds = \frac{s\sqrt{2}}{2}$. Thus the Bishop curvatures can be established as $k_1 = \frac{\sqrt{2}}{2} cos\left(\frac{s\sqrt{2}}{2}\right)$, and $k_2 = \frac{\sqrt{2}}{2} sin\left(\frac{s\sqrt{2}}{2}\right)$. Thus the vectors of Bishop frame can be provided as follows:

$$T(s) = \frac{\sqrt{2}}{2}\left(-sin(s), cos(s), 1\right),$$

$$N_1(s) = \begin{pmatrix} -\cos\left(\frac{s\sqrt{2}}{2}\right)\cos(s) - \frac{\sqrt{2}}{2}\sin\left(\frac{s\sqrt{2}}{2}\right)\sin(s), \\ -\cos\left(\frac{s\sqrt{2}}{2}\right)\sin(s) + \frac{\sqrt{2}}{2}\sin\left(\frac{s\sqrt{2}}{2}\right)\cos(s), \\ \frac{\sqrt{2}}{2}\sin\left(\frac{s\sqrt{2}}{2}\right), \end{pmatrix},$$

$$N_2(s) = \begin{pmatrix} -\sin\left(\frac{s\sqrt{2}}{2}\right)\cos(s) + \frac{\sqrt{2}}{2}\cos\left(\frac{s\sqrt{2}}{2}\right)\sin(s), \\ -\sin\left(\frac{s\sqrt{2}}{2}\right)\sin(s) - \frac{\sqrt{2}}{2}\cos\left(\frac{s\sqrt{2}}{2}\right)\cos(s), \\ \frac{\sqrt{2}}{2}\cos\left(\frac{s\sqrt{2}}{2}\right) \end{pmatrix}.$$

By referring to the definitions for TN_1, TN_2 and N_1N_2 Smarandache ruled surfaces, the graphs are provided in Fig. 1, Fig. 2 and Fig.3 3 where $s \in [-\pi, \pi]$ and $v \in [-1, 1]$.

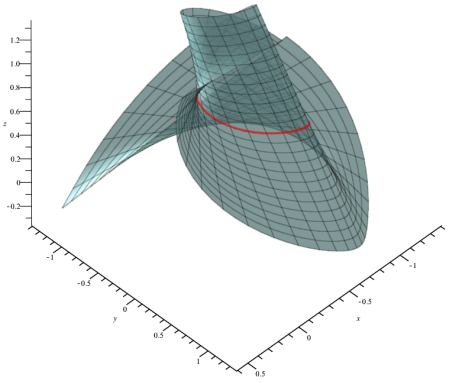

Figure 1: The ruled surface $\xi(s, v)$

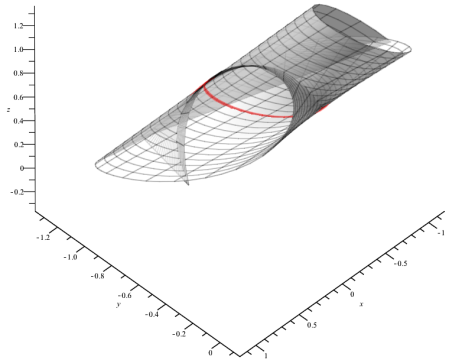

Figure 2: The ruled surface $\delta(s, v)$

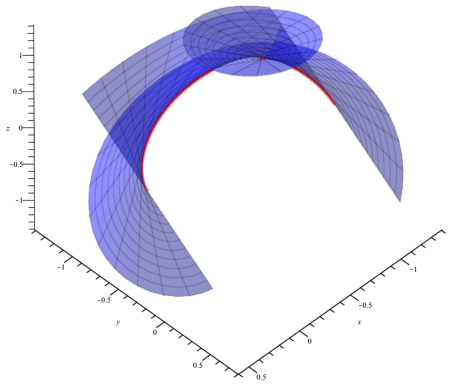

Figure 3: The ruled surface $\varepsilon(s, v)$

4. Conclusion

The paper introduced new ruled surfaces via Smarandache geometry using Bishop frame vectors. The characteristics of each surface, such as developability and minimality, were discussed. Furthermore, the characteristic curves on these surfaces were determined by providing the required conditions. It is shown that the special slant helix curve

defines the minimality condition for the ruled surface $\varepsilon(s,v)$. Finally, regardless of the choice of main curve, if the base curve of the ruled surface is considered to be N_1N_2 Smarandache curve, the developability characteristic remains valid This is analogous to the fact that tangent ruled surfaces are always developable.

Conflict of interests statement

The authors declare no conflict of interests.

Data availability statement

The manuscript has no associated data.

Acknowledgements

The authors would sincerely like to thank the reviewers, who improved the quality of the paper, with the generous comments and contributions. Authors also appreciate the editors of the journal taking care of the manuscript.

References

[1] P. Do-Carmo, "Differential geometry of curves and surfaces: revised and updated second edition", Courier Dover Publications, 2016.

[2] E. Abbena, S. Salamon and A. Gray, "Modern differential geometry of curves and surfaces with Mathematica", Chapman and Hall/CRC, 2017.

[3] H. H. Hacısalihoğlu , "Differential geometry II", Ankara University Press, 2000.

[4] D. J. Struik, "Lectures on classical differential geometry", Courier Corporation, 2012.

[5] M. Juza, "Ligne de striction sur unegeneralisation a plusierurs dimensions d'une surface regle", Czechoslovak Mathematical Journal 12(87) (1962), 243-250.

[6] S. Ouarab and A. O. Chahdi, "Some characteristic properties of ruled surface with Frenet frame of an arbitrary non-cylindrical ruled surface in Euclidean 3-space", International Journal of Applied Physics and Mathematics 10(1) (2020), 16-24.

[7] R. L. Bishop, "There is more than one way to frame a curve", The American Mathematical Monthly 82 (1975), 246-251.

[8] M. Masal and A. Z. Azak, "Ruled surfaces according to Bishop frame in the Euclidean 3-space", Proceedings of the National Academy of Sciences, India Section A: Physical Sciences 89(2) (2019), 415-424.

[9] Y. Tunçer, "Ruled surfaces with the Bishop frame in Euclidean 3–space", Gen. Math. Notes 26 (2015), 74-83.

[10] S. Ouarab, A. O. Chahdi, M. Izid, "Ruled surfaces with alternative moving frame in Euclidean 3-space", International Journal of Mathematical Sciences and Engineering Applications 12(2) (2018), 43-58.

[11] S. Şenyurt and K. Eren, "On ruled surfaces with Sannia frame in Euclidean 3-space", Kyungpook Mathematical Journal 62 (2022), 509-531.

[12] S. Şenyurt and K. Eren, "On ruled surfaces with Sannia frame in Euclidean 3-space", Kyungpook Mathematical Journal 62 (2022), 509-531.
A. Elsharkawy, H. Elsayied, and A. Refaat, "Quasi Ruled Surfaces in Euclidean 3-space", European Journal of Pure and Applied Mathematics, 18(1), 5710-5710.

[13] S. Ouarab, "Corrigendum to Smarandache Ruled Surfaces according to Frenet-Serret Frame of a Regular Curve in E^3", Abstract and Applied Analysis 2022 (2022).

[14] M. Turgut and S. Yılmaz, "Smarandache Curves in Minkowski Spacetime", International Journal of Mathematical Combinatorics 3 (2008), 51-55.

[15] A.T. Ali, "Special Smarandache curves in the Euclidean space", International Journal of Mathematical Combinatorics 2 (2010), 30-36.

[16] S. Ouarab, "Smarandache Ruled Surfaces according to Darboux Frame in E^3", Journal of Mathematics 2021 (2021).

[17] S. Ouarab, "NC-Smarandache Ruled Surface and NW-Smarandache Ruled Surface according to Alternative Moving Frame in E^3", Journal of Mathematics 2021 (2021).

[18] S. Şenyurt, D. Canlı and Ç. Elif, "Smarandache-Based Ruled Surfaces with the Darboux Vector According to Frenet Frame in E^3", Journal of New Theory, 39, (2022), 8-18.

[19] S. Şenyurt, D. Canlı and Ç. Elif, "Some special Smarandache ruled surfaces by Frenet Frame in E^3 - I", Turkish Journal of Science, 7, (2022), 31-42.

[20] S. Şenyurt, D. Canlı, Ç. Elif and S. G. Mazlum, "Some special Smarandache ruled surfaces by Frenet frame in E^3 -II", Honam Mathematical Journal, 44(4), (2022), 594-617.

[21] B. Bükcü, M. K. Karacan, "The slant helices according to Bishop frame", World Academy of Science, Engineering and Technology International Journal of Mathematical and Computational Sciences, 3 (2009), 67-70.

Appendix

The following figures Fig. 4, Fig. 5 and Fig. 6 are also presented to examine the view of each surface from different angles. The orientations are fixed to the x, y and z axis, respectively.

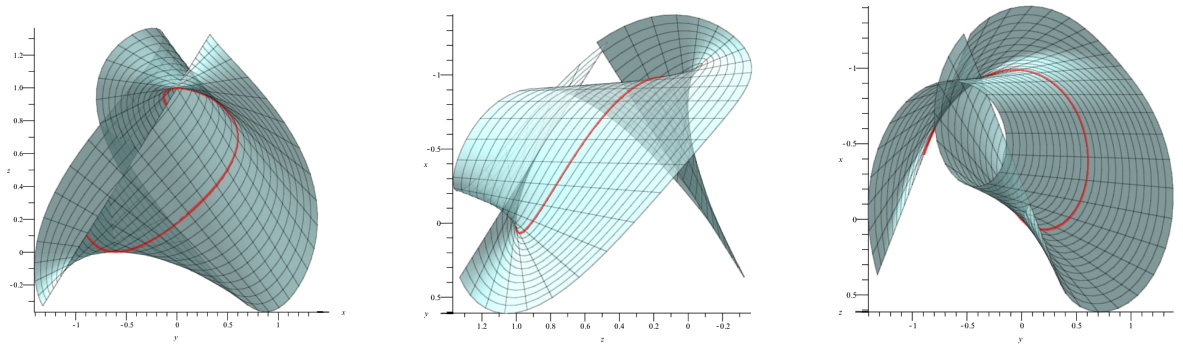

(a) oriented to x axis (b) oriented to y axis (c) oriented to z axis

Figure 4: The TN_1 Smarandache ruled surface $\xi(s,v)$

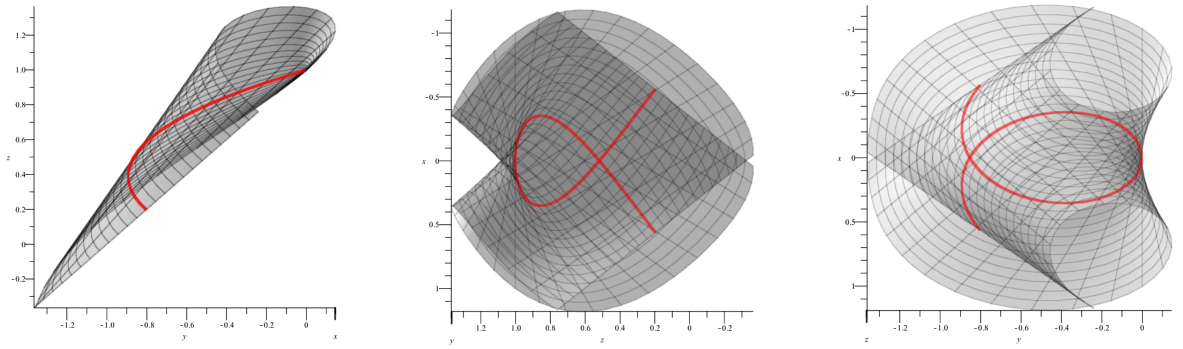

(a) oriented to x axis (b) oriented to y axis (c) oriented to z axis

Figure 5: The TN_2 Smarandache ruled surface $\delta(s,v)$

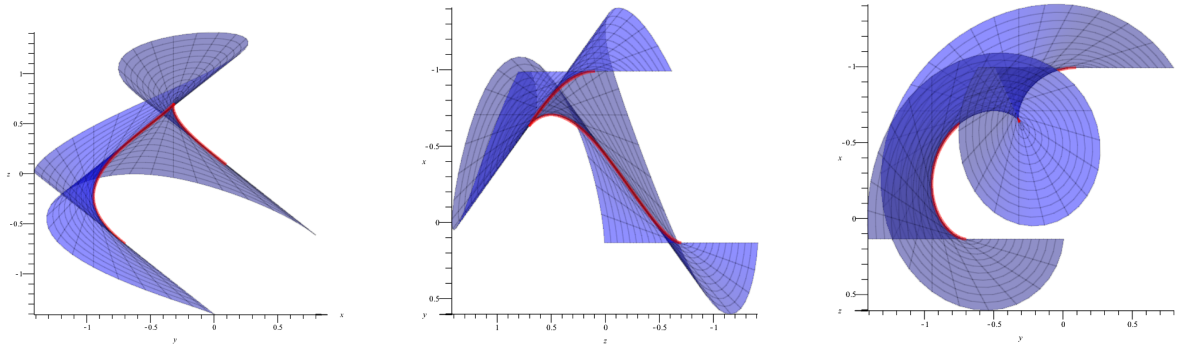

(a) oriented to x axis (b) oriented to y axis (c) oriented to z axis

Figure 6: The N_1N_2 Smarandache Ruled surface $\varepsilon(s,v)$

MANAS Journal of Engineering
ISSN 1694-7398 — e-ISSN 1694-7398

Volume 13 (Issue 1) (2025) Pages 18-22
https://doi.org/10.51354/mjen.1543383

Generalized Pathway Fractional Integral Formulas Involving Extended Multi-Index Mittag-Leffler Function in Kernel of SUM Transform

Muhammad Lawan Kaurangini[1], Umar Muhammad Abubakar[2,*], Enes Ata[3] ,

[1] Aliko Dangote University of Science and Technology, Wudil P.M.B.: 3244 Kano, Kano State-Nigeria , kaurangini@kustwudil.edu.ng, ORCID: 0000-0001-9144-9433,

[2]Aliko Dangote University of Science and Technology, Wudil P.M.B.: 3244 Kano, Kano State-Nigeria , uabubakar@kustwudil.edu.ng, ORCID: 0000-0003-3935-4829,

[3]Department of Mathematics, Faculty of Arts and Science, Kirsehir Ahi Evran University, Kirsehir, Turkey, enesata.tr@gmail.com, ORCID: 0000-0001-6893-8693

ABSTRACT

The generalized pathway fractional integral formulas for the newly extended multi-index Mittag-Leffler function defined by using two Fox-Wright functions as its kernel is studied. Moreover, the SUM integral transform of the composition formula for the pathway fractional integral and extended multi-index Mittag-Leffler function is also presented.

ARTICLE INFO

Research article

Received: 04.09.2024
Accepted: 26.02.2025

Keywords: SUM transform, Laplace transform, Mittag-Leffler function, Pathway fractional integral operator, Wright function

**Corresponding author*

1. Introduction

Fractional calculus deal with the study of derivative and integration of arbitrary order such as fractional, irrational and complex, it is also applicable in almost all area of real life such as epidemic model, reaction-diffusion, drying model, control theory, economics, fluid dynamics, etc (see for example, [1–4]). The following pathway fractional integral operator was introduced in [5]:

$$\left(P_{0^+}^{\tau,\rho;b}\right)(x) = x^{-\tau}\int_0^{\left[\frac{x}{b(1-\rho)}\right]}\left(1-\frac{b(1-\rho)t}{x}\right)^{\frac{\tau}{1-\rho}} f(t)dt,$$

where $f(t) \in L(a,b)$ and $\tau \in \mathbb{C}$, $x \in \mathbb{R}^+$ such that $b > 0$, $Re(\tau) > 0$ and $\rho < 1$ (ρ is a pathway parameter).

In 2013, Nair [6] introduced the following generalized pathway hypergeometric fractional integral operator:

$$\left(P_{0^+}^{\tau,\vartheta,\mu,\rho;b}\right)(x) = x^{-\tau}\int_0^{\left[\frac{x}{b(1-\rho)}\right]}\left(1-\frac{b(1-\rho)t}{x}\right)^{\frac{\tau-1}{1-\rho}} \times {}_2F_1\left(\frac{\tau-1}{1-\rho}+\vartheta+1,-\mu;\frac{\tau-1}{1-\rho}+1;1-\frac{b(1-\rho)t}{x}\right) \times f(t)dt, \quad (1)$$

where $f(t) \in \mathbb{R}^+$ and $\tau, \vartheta, \mu, \rho \in \mathbb{C}$, $x \in \mathbb{R}^+$ such that $b > 0$, $Re\left(\frac{\tau-1}{1-\rho}+1\right) > 0$, $Re(\mu-\vartheta) > 0$ and $\rho < 1$.

Remark 1: The following are also reported in [7]:

(i) If $Re(\tau) > 0$ when $\rho = 0$ and $b = 1$, Eq. (1) reduces to the following Saigo fractional integral operator:

$$\left(P_{0^+}^{\tau,\vartheta,\mu,0;1}\right)(x) = x\Gamma(\tau)\left(I_{0^+}^{\tau,\vartheta,\mu}\right)(x).$$

(ii) If $Re(\tau) > 0$ when $\rho = 0$, $b = 1$ and $\vartheta = -\tau$, Eq. (1) reduces to the following Riemann-Liouville fractional integral operator:

$$\left(P_{0^+}^{\tau,-\tau,\mu,0;1}\right)(x) = x\Gamma(\tau)\left(I_{0^+}^{\tau}\right)(x).$$

(iii) If $\rho = 0$, $\vartheta = 0$ and $b = 1$, Eq. (1) reduces to the following Kober fractional integral operator:

$$\left(P_{0^+}^{\tau,0,\mu,0;1}\right)(x) = x\Gamma(\tau)\left(I_{0^+}^{\tau,\mu}\right)(x).$$

(iv) If $\mu = 0$, $Re(\tau - 1) > 0$, Eq. (1) reduces to the following classical pathway fractional integral operator:

$$\left(P_{0^+}^{\tau-1,\vartheta,0,\rho;b}\right)(x) = x^{1-\tau-\vartheta}\Gamma(\tau)\left(P_{0^+}^{\tau-1,\rho}\right)(x).$$

(v) If $\mu = 0$, $\rho \to 1_-$, Eq. (1) reduces to the following Laplace integral transform:

$$\lim_{\rho\to 1_-}\left(P_{0^+}^{\tau,\vartheta,0,\rho;b}\right)(x) = x^{1-\vartheta}L\{f(t)\}\left(\frac{x}{b(1-\rho)}\right).$$

Recently, Kaurangini et al., [8] studied the following multi-index Mittag-Leffler function:

$$\begin{aligned}
&{}^{\Psi}E^{\lambda,\delta,p,q;\omega,\varpi}_{(\varrho_i,\sigma_i)_\eta,\ell,\varrho}(z;\Phi,\Omega)\\
&= {}^{\Psi}E^{\lambda,\delta,p,q;\omega,\varpi}_{(\varrho_i,\sigma_i)_\eta,\ell,\varrho}\left[\begin{array}{c|c|c}(B_k,b_k)_{1,\alpha} & (E_m,e_m)_{1,\gamma} & \\ (D_j,d_j)_{1,\beta} & (G_n,g_n)_{1,\delta} & z;\Phi,\Omega\end{array}\right]\\
&= \sum_{r=0}^{\infty}\frac{{}^{\Psi}B^{\omega,\varpi}_{\Phi,\Omega}(\lambda+pr,\delta-\lambda)}{B(\lambda,\delta-\lambda)}\frac{(\delta)_{qr}z^r}{\prod_{i=1}^{\eta}\Gamma(\varrho_i r+\sigma_i)(\phi)_{\kappa r}},
\end{aligned} \tag{2}$$

where $\varrho_i, \sigma_i, \phi, \kappa, \lambda, \delta, \Phi, \Omega\omega, \varpi, z \in \mathbb{C}$, $\Phi, \Omega > 0$, $Re(\delta) > Re(\lambda) > 0, Re(\sigma_i) > 0, i = 1, 2, \ldots, \eta$, $Re(\varrho_{i=0}^{\eta}\aleph_i) > \max\{0, Re(q) - 1\}, Re(\phi) > 0$.

Here denotes ${}^{\Psi}B^{\omega,\varpi}_{\Phi,\Omega}(x, y)$ is the extended beta function [9, 10] and defined by

$$\begin{aligned}
&{}^{\Psi}B^{\omega,\varpi}_{\Phi,\Omega}(x,y)\\
&= {}^{\Psi}B^{\omega,\varpi}_{\Phi,\Omega}\left[\begin{array}{c|c|c}(B_k,b_k)_{1,\alpha} & (E_m,e_m)_{1,\gamma} & \\ (D_j,d_j)_{1,\beta} & (G_n,g_n)_{1,\delta} & x,y\end{array}\right]\\
&= \int_0^1 t^{x-1}(1-t)^{y-1}{}_{\alpha}\Psi_{\beta}\left(-\frac{\Phi}{t^{\omega}}\right){}_{\gamma}\Psi_{\delta}\left(-\frac{\Omega}{(1-t)^{\varpi}}\right)dt,
\end{aligned}$$

where ${}_{\alpha}\Psi_{\beta}(.)$ is the Fox-Wright function [11] defined by

$$\begin{aligned}
{}_{\alpha}\Psi_{\beta}(z) &= {}_{\alpha}\Psi_{\beta}\left[\begin{array}{c|c}(B_k,b_k)_{1,\alpha} & \\ (D_j,d_j)_{1,\beta} & z\end{array}\right]\\
&= \sum_{r=0}^{\infty}\frac{\prod_{k=1}^{\alpha}\Gamma(B_k n+b_k)}{\prod_{j=1}^{\beta}\Gamma(D_j r+d_j)}\frac{z^r}{r!},
\end{aligned} \tag{3}$$

$$(z, b_k, d_j \in \mathbb{C}, B_k, D_j \in \mathbb{R}).$$

2. The Generalized Pathway Fractional Integral Formulas involving Extended Multi-Index Mittag-Leffler Function in the Kernel

The generalized pathway fractional integral formula for the new extended multi-index Mittag-Leffler function is studied.

Lemma 1: [7] The following result holds true

$$\begin{aligned}
\left(P_{0^+}^{\tau,\vartheta,\mu,\rho;b}\nu^{\wp-1}\right)(x) &= \frac{1}{[b(1-\rho)]^{\wp}}\\
&\times\frac{\Gamma(\wp)\Gamma(\wp-\vartheta+\mu)\Gamma\left(1+\frac{\tau-1}{1-\rho}\right)}{\Gamma(\wp-\vartheta)\Gamma\left(1+\wp+\mu+\frac{\tau-1}{1-\rho}\right)}x^{\wp-\vartheta},
\end{aligned} \tag{4}$$

where $f(t) \in \mathbb{R}^+$ and $\tau, \vartheta, \mu, \rho \in \mathbb{C}, x \in \mathbb{R}^+$ such that $b > 0$, $Re\left(\frac{\tau-1}{1-\rho}+1\right) > 0$, $Re(\wp) > \max\{0, Re(\mu-\vartheta)\} > 0$ and $\rho < 1$.

Theorem 1: The following pathway fractional formula holds

$$\begin{aligned}
&\left(P_{0^+}^{\tau,\vartheta,\mu,\rho;b}\nu^{\wp-1}{}^{\Psi}E^{\lambda,\delta,p,q;\omega,\varpi}_{(\varrho_i,\sigma_i)_\eta,\ell,\varrho}(z\nu^{\ell};\rho,\sigma)\right)(x)\\
&= \frac{x^{\wp-\vartheta}\Gamma\left(1+\frac{\tau-1}{\rho-1}\right)}{[b(1-\rho)]^{\wp}}{}^{\Psi}E^{\lambda,\delta,p,q;\omega,\varpi}_{(\varrho_i,\sigma_i)_\eta,\ell,\varrho}\left(\frac{z\nu^{\ell}}{[b(1-\rho)]^{\wp}};\Phi,\Omega\right)\\
&* {}_3\Psi_2\left[\begin{array}{c|c}(\wp,\ell),(\wp-\vartheta+\mu,\ell),(1,1) & \\ (\wp-\vartheta,\ell),\left(1+\wp\mu+\frac{\tau-1}{1-\rho},\ell\right) & \frac{zx^{\ell}}{[b(1-\rho)]^{\ell}}\end{array}\right],
\end{aligned} \tag{5}$$

where $*$ represent Hadamard (convolution) product defined in Pohlen [12].

Proof: Letting the right hand side of Eq. (6) be P and using (2), changing the order of summation and pathway fractional integral operator, we have

$$\begin{aligned}
P = &\sum_{r=0}^{\infty}\frac{{}^{\Psi}B^{\omega,\varpi}_{\Phi,\Omega}(\lambda+pr,\delta-\lambda)}{B(\lambda,\delta-\lambda)}\frac{(\delta)_{qr}z^r}{\prod_{i=1}^{\eta}\Gamma(\varrho_i r+\sigma_i)(\phi)_{\kappa r}}\\
&\times\left(P_{0^+}^{\tau,\vartheta,\mu,\rho;b}\nu^{\wp+\ell r-1}\right)(x).
\end{aligned}$$

Applying Eq. (4) to the above equation, gives

$$\begin{aligned}
P = &\frac{x^{\wp-\vartheta}\Gamma\left(1+\frac{\tau-1}{\rho-1}\right)}{[b(1-\rho)]^{\wp}}\sum_{r=0}^{\infty}\frac{{}^{\Psi}B^{\omega,\varpi}_{\Phi,\Omega}(\lambda+pr,\delta-\lambda)}{B(\lambda,\delta-\lambda)}\\
&\times\frac{(\delta)_{qr}z^r}{\prod_{i=1}^{\eta}\Gamma(\varrho_i r+\sigma_i)(\phi)_{\kappa r}}\frac{\Gamma(\wp+\ell r)}{\Gamma(\wp-\vartheta+\ell r)}\\
&\times\frac{\Gamma(\wp-\vartheta+\mu+\ell r)}{\Gamma\left(1+\wp+\mu+\frac{\tau-1}{1-\rho}+\ell r\right)}\left(\frac{zx^{\ell}}{[b(1-\rho)]^{\ell}}\right)^r.
\end{aligned} \tag{6}$$

Using the multi-index Mittag-Leffler function in Eq. (2) and the Wright function in (3) to (6), the required result in (5) is obtained.

As a consequence of Theorem 1 the following corollaries are obtained:

Corollary 1: The following equility is true

$$\left(P_{0^+}^{\tau,\vartheta,\mu,0;1}\nu^{\wp-1}\Psi E^{\lambda,\delta,p,q;\omega,\varpi}_{(\varrho_i,\sigma_i)_\eta,\ell,\varrho}(z\nu^\ell;\Phi,\Omega)\right)(x)$$
$$= x^{\wp-\vartheta}\Gamma(\tau)\,{}^{\Psi}E^{\lambda,\delta,p,q;\omega,\varpi}_{(\varrho_i,\sigma_i)_\eta,\ell,\varrho}\left(z\nu^\ell;\Phi,\Omega\right)$$
$$*\,{}_3\Psi_2\left[\begin{matrix}(\wp,\ell),(\wp-\vartheta+\mu,\ell),(1,1)\\(\wp-\vartheta,\ell),(\wp+\tau\mu+\tau,\ell)\end{matrix}\middle|\, zx^\ell\right].$$

Corollary 2: The following result holds

$$\left(P_{0^+}^{\tau,-\tau,\mu,0;1}\nu^{\wp-1}\Psi E^{\lambda,\delta,p,q;\omega,\varpi}_{(\varrho_i,\sigma_i)_\eta,\ell,\varrho}(z\nu^\ell;\Phi,\Omega)\right)(x)$$
$$= x^{\wp+\tau}\Gamma(\tau)\,{}^{\Psi}E^{\lambda,\delta,p,q;\omega,\varpi}_{(\varrho_i,\sigma_i)_\eta,\ell,\varrho}\left(z\nu^\ell;\Phi,\Omega\right)$$
$$*\,{}_2\Psi_1\left[\begin{matrix}(\wp,\ell),(1,1)\\(\wp+\tau,\ell)\end{matrix}\middle|\, zx^\ell\right].$$

Corollary 3: The following formula is true

$$\left(P_{0^+}^{\tau,0,\mu,0;1}\nu^{\wp-1}\Psi E^{\lambda,\delta,p,q;\omega,\varpi}_{(\varrho_i,\sigma_i)_\eta,\ell,\varrho}(z\nu^\ell;\Phi,\Omega)\right)(x)$$
$$= x^{\wp}\Gamma(\tau)\,{}^{\Psi}E^{\lambda,\delta,p,q;\omega,\varpi}_{(\varrho_i,\sigma_i)_\eta,\ell,\varrho}\left(z\nu^\ell;\Phi,\Omega\right)$$
$$*\,{}_2\Psi_1\left[\begin{matrix}(\wp,\ell),(1,1)\\(\wp+\tau+\mu,\ell)\end{matrix}\middle|\, zx^\ell\right].$$

Corollary 4: The following result holds true

$$\left(P_{0^+}^{\tau,\vartheta,0,\rho;b}\nu^{\wp-1}\Psi E^{\lambda,\delta,p,q;\omega,\varpi}_{(\varrho_i,\sigma_i)_\eta,\ell,\varrho}(z\nu^\ell;\Phi,\Omega)\right)(x)$$
$$= \frac{x^{\wp-\vartheta}\Gamma\left(1+\frac{\tau-1}{\rho-1}\right)}{[b(1-\rho)]^{\wp}}$$
$$\times\,{}^{\Psi}E^{\lambda,\delta,p,q;\omega,\varpi}_{(\varrho_i,\sigma_i)_\eta,\ell,\varrho}\left(\frac{z\nu^\ell}{[b(1-\rho)]^{\wp}};\Phi,\Omega\right)$$
$$*\,{}_2\Psi_1\left[\begin{matrix}(\wp,\ell),(1,1)\\\left(1+\wp\mu+\frac{\tau-1}{1-\rho},\ell\right)\end{matrix}\middle|\, \frac{zx^\ell}{[b(1-\rho)]^\ell}\right].$$

Corollary 5: The following formula holds true

$$\left(P_{0^+}^{\tau,\vartheta,0,1;b}\nu^{\wp-1}\Psi E^{\lambda,\delta,p,q;\omega,\varpi}_{(\varrho_i,\sigma_i)_\eta,\ell,\varrho}(z\nu^\ell;\Phi,\Omega)\right)(x)$$
$$= \frac{x^{\wp-\vartheta}}{[b(1-\rho)]^{\wp}}\,{}^{\Psi}E^{\lambda,\delta,p,q;\omega,\varpi}_{(\varrho_i,\sigma_i)_\eta,\ell,\varrho}\left(\frac{z\nu^\ell}{[b(1-\rho)]^{\wp}};\Phi,\Omega\right)$$
$$*\,{}_2\Psi_0\left[\begin{matrix}(\wp,\ell),(1,1)\\-\end{matrix}\middle|\, \frac{zx^\ell}{[b(1-\rho)]^\ell}\right].$$

3. Generalized Pathway Fractional Integral Formulas involving Extended Multi-Index Mittag-Leffler Function in the Kernel of the SUM transform

The SUM (Sameer-Umar-Muhammad) integral transform is defined by the following formula [13, 14]:

$$S_\Lambda\{f(t)\}(p) = \frac{1}{p^\hbar}\int_0^\infty f(t)\Lambda^{pt}dt, \tag{7}$$

where $t \geq 0, \hbar \in \mathbb{N}$, $\Lambda > 0$, $m_1 \leq p \leq m_2$, $m_1, m_2 > 0$ and $f(t)$ is piecewise continuous and exponential order. The SUM transform of power function is given by

$$S_\Lambda\{t^\wp\}(p) = \frac{\Gamma(\wp+1)}{p^\hbar[plog(\Lambda)]^{\wp+1}}, \quad (\wp \in \mathbb{C}). \tag{8}$$

Theorem 2: The following result holds

$$S_\Lambda\left\{\left(t\cdot P_{0^+}^{\tau,\vartheta,\mu,\rho;b}\nu^{\wp-1}\Psi E^{\lambda,\delta,p,q;\omega,\varpi}_{(\varrho_i,\sigma_i)_\eta,\ell,\varrho}(t\nu^\ell;\Phi,\Omega)\right)(x)\right\}(p)$$
$$= \frac{x^{\wp-\vartheta}\Gamma\left(1+\frac{\tau-1}{\rho-1}\right)}{p^\hbar[b(1-\rho)]^{\wp}[plog(\Lambda)]^2}$$
$$\times\,{}^{\Psi}E^{\lambda,\delta,p,q;\omega,\varpi}_{(\varrho_i,\sigma_i)_\eta,\ell,\varrho}\left(\frac{z\nu^\ell}{[b(1-\rho)]^{\wp}[plog(\Lambda)]};\Phi,\Omega\right)$$
$$*\,{}_4\Psi_2\left[\begin{matrix}(\wp,\ell),(\wp-\vartheta+\mu,\ell),(1,1),(2,1)\\(\wp-\vartheta,\ell),\left(1+\wp\mu+\frac{\tau-1}{1-\rho},\ell\right)\end{matrix}\middle|\, \frac{x^\ell}{[b(1-\rho)]^\ell[plog(\Lambda)]}\right]. \tag{9}$$

Proof: Letting the right hand side of Eq. (8) be S and using (6) and (7), changing the order of summation and pathway fractional integral operator, we have

$$S = \frac{x^{\wp-\vartheta}\Gamma\left(1+\frac{\tau-1}{\rho-1}\right)}{[b(1-\rho)]^{\wp}}\sum_{r=0}^{\infty}\frac{{}^{\Psi}B^{\omega,\varpi}_{\Phi,\Omega}(\lambda+pr,\delta-\lambda)}{B(\lambda,\delta-\lambda)}$$
$$\times\frac{(\delta)_{qr}z^r}{\prod_{i=1}^{\eta}\Gamma(\varrho_i r+\sigma_i)(\phi)_{\kappa r}}\frac{\Gamma(\wp+\ell r)}{\Gamma(\wp-\vartheta+\ell r)}$$
$$\times\frac{\Gamma(\wp-\vartheta+\mu+\ell r)}{\Gamma\left(1+\wp+\mu+\frac{\tau-1}{1-\rho}+\ell r\right)}\left(\frac{zx^\ell}{[b(1-\rho)]^\ell}\right)^r S_\Lambda\{t^{r+1}\}(p).$$

Using Eq. (8) to the above equation, we obtain

$$S = \frac{x^{\wp-\vartheta}\Gamma\left(1+\frac{\tau-1}{\rho-1}\right)}{p^\hbar[b(1-\rho)]^{\wp}[plog(\Lambda)]^2}\sum_{r=0}^{\infty}\frac{{}^{\Psi}B^{\omega,\varpi}_{\Phi,\Omega}(\lambda+pr,\delta-\lambda)}{B(\lambda,\delta-\lambda)}$$
$$\times\frac{(\delta)_{qr}z^r}{\prod_{i=1}^{\eta}\Gamma(\varrho_i r+\sigma_i)(\phi)_{\kappa r}}\frac{\Gamma(\wp+\ell r)}{\Gamma(\wp-\vartheta+\ell r)}$$
$$\times\frac{\Gamma(\wp-\vartheta+\mu+\ell r)}{\Gamma\left(1+\wp+\mu+\frac{\tau-1}{1-\rho}+\ell r\right)}\left(\frac{zx^\ell}{[b(1-\rho)]^\ell[plog(\Lambda)]}\right)^r. \tag{10}$$

Using the multi-index Mittag-Leffler function in Eq. (2) and the Wright function in (3) to (10) , the required result in (9) is obtained.

Corollary 6: The following result is also true

$$S_\Lambda\left\{\left(t\cdot P_{0^+}^{\tau,\vartheta,\mu,0;1}\nu^{\wp-1}{}^{\Psi}E^{\lambda,\delta,p,q;\omega,\varpi}_{(\varrho_i,\sigma_i)_\eta,\ell,\varrho}(t\nu^\ell;\Phi,\Omega)\right)(x)\right\}(p)$$
$$=\frac{x^{\wp-\vartheta}\Gamma(\tau)}{p^\hbar[plog(\Lambda)]^2}$$
$$\times{}^{\Psi}E^{\lambda,\delta,p,q;\omega,\varpi}_{(\varrho_i,\sigma_i)_\eta,\ell,\varrho}\left(\frac{z\nu^\ell}{[b(1-\rho)]^\wp[plog(\Lambda)]};\Phi,\Omega\right)$$
$$*\,{}_4\Psi_2\left[\begin{matrix}(\wp,\ell),(\wp-\vartheta+\mu,\ell),(1,1),(2,1)\\(\wp+\tau+\mu,\ell),(\wp-\vartheta,\ell)\end{matrix}\middle|\,\frac{x^\ell}{[plog(\Lambda)]}\right].$$

Corollary 7: The following formula holds

$$S_\Lambda\left\{\left(t\cdot P_{0^+}^{\tau,-\tau,\mu,0;1}\nu^{\wp-1}{}^{\Psi}E^{\lambda,\delta,p,q;\omega,\varpi}_{(\varrho_i,\sigma_i)_\eta,\ell,\varrho}(t\nu^\ell;\Phi,\Omega)\right)(x)\right\}(p)$$
$$=\frac{x^{\wp+\tau}\Gamma(\tau)}{p^\hbar[plog(\Lambda)]^2}{}^{\Psi}E^{\lambda,\delta,p,q;\omega,\varpi}_{(\varrho_i,\sigma_i)_\eta,\ell,\varrho}\left(\frac{\nu^\ell}{[plog(\Lambda)]};\Phi,\Omega\right)$$
$$*\,{}_3\Psi_1\left[\begin{matrix}(\wp,\ell),(1,1),(2,1)\\(\wp+\tau,\ell)\end{matrix}\middle|\,\frac{x^\ell}{[plog(\Lambda)]}\right].$$

Corollary 8: The following results equation is true

$$S_\Lambda\left\{\left(t\cdot P_{0^+}^{\tau,0,\mu,0;1}\nu^{\wp-1}{}^{\Psi}E^{\lambda,\delta,p,q;\omega,\varpi}_{(\varrho_i,\sigma_i)_\eta,\ell,\varrho}(t\nu^\ell;\Phi,\Omega)\right)(x)\right\}(p)$$
$$=\frac{x^{\wp}\Gamma(\tau)}{p^\hbar[plog(\Lambda)]^2}{}^{\Psi}E^{\lambda,\delta,p,q;\omega,\varpi}_{(\varrho_i,\sigma_i)_\eta,\ell,\varrho}\left(\frac{\nu^\ell}{[plog(\Lambda)]};\Phi,\Omega\right)$$
$$*\,{}_3\Psi_1\left[\begin{matrix}(\wp,\ell),(1,1),(2,1)\\(\wp+\mu,\ell)\end{matrix}\middle|\,\frac{x^\ell}{[plog(\Lambda)]}\right].$$

Corollary 9: The following equility holds

$$S_\Lambda\left\{\left(t\cdot P_{0^+}^{\tau,\vartheta,0,\rho;b}\nu^{\wp-1}{}^{\Psi}E^{\lambda,\delta,p,q;\omega,\varpi}_{(\varrho_i,\sigma_i)_\eta,\ell,\varrho}(t\nu^\ell;\Phi,\Omega)\right)(x)\right\}(p)$$
$$=\frac{x^{\wp-\vartheta}\Gamma\left(1+\frac{\tau-1}{\rho-1}\right)}{p^\hbar[b(1-\rho)]^\wp[plog(\Lambda)]^2}$$
$$\times{}^{\Psi}E^{\lambda,\delta,p,q;\omega,\varpi}_{(\varrho_i,\sigma_i)_\eta,\ell,\varrho}\left(\frac{z\nu^\ell}{[b(1-\rho)]^\wp[plog(\Lambda)]};\Phi,\Omega\right)$$
$$*\,{}_3\Psi_1\left[\begin{matrix}(\wp,\ell),(1,1),(2,1)\\\left(1+\wp\mu+\frac{\tau-1}{1-\rho},\ell\right)\end{matrix}\middle|\,\frac{x^\ell}{[b(1-\rho)]^\ell[plog(\Lambda)]}\right].$$

Corollary 10: The following result is true

$$S_\Lambda\left\{\left(t\cdot P_{0^+}^{\tau,\vartheta,0,1;b}\nu^{\wp-1}\right.\right.$$
$$\left.\left.\times{}^{\Psi}E^{\lambda,\delta,p,q;\omega,\varpi}_{(\varrho_i,\sigma_i)_\eta,\ell,\varrho}\left(\frac{\nu^\ell}{[b(1-\rho)]^\ell[plog(\Lambda)]};\Phi,\Omega\right)\right)(x)\right\}(p)$$
$$=\frac{x^{\wp-\vartheta}}{[b(1-\rho)]^\wp[plog(\Lambda)]^2}$$
$$\times{}^{\Psi}E^{\lambda,\delta,p,q;\omega,\varpi}_{(\varrho_i,\sigma_i)_\eta,\ell,\varrho}\left(\frac{z\nu^\ell}{[b(1-\rho)]^\wp[plog(\Lambda)]};\Phi,\Omega\right)$$
$$*\,{}_3\Psi_0\left[\begin{matrix}(\wp,\ell),(1,1),(2,1)\\-\end{matrix}\middle|\,\frac{x^\ell}{[b(1-\rho)]^\ell}\right].$$

4. Conclusion

The SUM integral transform is applied on generalized pathway fractional integral operator with extended multi-index Mittag-Leffler function in the kernel. Our result is general in nature which in some of it special cases include the recent results obtained by in [15, 16] follows. It is hope that the result obtained here will have potential applications in science, technology and engineering.

References

[1] Singh A., Kumar S., Vigo-Angular, J., On New Approximations of Caputo-Prabhakar Fractional Derivative and their Application to Reaction-diffusion Problems with Variable Coefficients, Mathematical Method in the Applied Sciences 47, (2023), 268-296.

[2] Yadav P., Johan S., Shah K., Peter O.M., Fractional-order Modeling and Analysis of Debates Mellitus: Utilizing the Atangana-Baleanu Caputo (ABC) operator, Alexandria Engineering Journal, 81, (2023), 200-209.

[3] Kaur, D., A details study on fractional calculus, In: Conference Proceeding of International Multidisplinary Conference, pp. 54-59, 2022.

[4] Turkyilmazoglu, M., Altanji, M., "Fractional Models of Falling Object with Linear and Quadratic Frictional Forces Considering Caputo Derivatives," Chaos, Solitons and Fractals, 166:112980, 2023.

[5] Nair, S.S., Pathway Fractional Integration Operator, Fractional Calculus and Applied Analysis, 12, (2009), 237-259.

[6] Nair, D.H., On a class of Fractional Integral Operator through Pathway Ideas, Proceeding of $12th$ Annual Conference Society for Special Functions and Their Applications, 12, pp. 91-109, 2013.

[7] Pal, A., Jana, R.K., Shukla, A.K., Generalized Integral Transform and Fractional Calculus involving Extended ${}_qR_q(\alpha,\beta;z)$ Function, Journal of the Indian Mathematical Society, 89, (2022), 100-116.

[8] Kaurangini, M.L., Abubakar, U.M., Ata, E., New Extended Multi-index Mittag-Leffler Function and Application of Double Mellin Integral Transform and Riemann-Liouville Fractional Operators, Submitted for Publication, 2024.

[9] Kaurangini, M.L., Chaudhary, M.P., Abubakar, U.M., Kiymaz, I.O., Ata, E., On Some Special Functions with Bi-Fox-Wright Function Kernel," Submitted for Publication 2024.

[10] Chaudhary, M.P., M.L. Kaurangini, M.L., Kiymaz, I.O., Abubakar, U.M., Ata, E., Fractional Integrations for the New Generalized Hypergeometric Functions, Journal of Ramanujan Society of Mathematical Science, 10, (2023), 77-100.

[11] Ghanim, F., Al-Janaby, H.F., Al-Momani, M., A New Euler-Beta Function Model with Statistical Implementation Related to the Mittag-Leffler-Kumar Function, Kuwait Journal of Science, 2023, (2023), 1-27.

[12] Pohlen, T., The Hadamard Product and Universal Power Series, PhD Dissertation, Unviversitat Trier, Trier, Germany, 2009.

[13] Hasan, S.Q., Abubakar, U.M., Kaurangini, M.L., The New Integral Transform "SUM Transform" and its Properties, Palestine Journal Mathematics, 12(2023), 30-45.

[14] Hassan,S. Q., Mansour, A.I., Abubakar,U.M., Applications of the SUM Integral Transform in Science and Technolog, Wasit Journal for Pure sciences, 2, (2023), 29-40.

[15] Rahman, G., Nisar, K.S., Choi, J., Mubeen, S., Arshad, M., Pathway fractional Integral Formulas involving Extended Mittag-Leffler Functions in the Kernel, Kyungpook Mathematical Journal, 59, (2019), 125-134.

[16] Agarwal, P., Akhtar, H.M., Khan, A., Momani, S., Abdel-Aty, M., Pathway Fractional Formula involving Extended Mittag-Leffler Function in the Kernel of Generalized Elzaki Transform, Progress in Fractional Differential and Applications, 9, (2023), 25-32.

MANAS Journal of Engineering
ISSN 1694-7398 | e-ISSN 1694-7398

Volume 13, Issue 1, (2025) Pages 23-29
https://doi.org/10.51354/mjen.1543960

Experimental characterization of thermal, mechanical, physical and morphological performance of thermoplastic polyurethane composites containing acidic pumice

Ahmet Bulut[1], Ümit Tayfun[2], Mehmet Yurderi[3,*]

[1] Bartın University, Faculty of Science, Bartın, Türkiye, abulut@bartin.edu.tr, ORCID: 0000-0002-1697-8623
[2] Bartın University, Faculty of Engineering, Architecture and Design, Bartın, Türkiye, utayfun@bartin.edu.tr, ORCID: 0000-0001-5978-5162
[3] Bartın University, Bartın Vocational School, Bartın, Türkiye, myurderi@bartin.edu.tr, ORCID: 0000-0002-0233-8940

ABSTRACT

Pumice powder, with its porous structure and low density, is a metal support material in water purification, catalysis manufacturing, and light construction materials. Acidic pumice has a significant proportion of silica. In this study, it was aimed to increase the mechanical and physical performances, as well as the reduction in the specific gravity and cost values, with the addition of acidic pumice to the thermoplastic polyurethane (TPU) polymer, which is used in various sectors such as textile, logistics, construction, and medical applications. Acidic pumice powder was blended with TPU at 2.5, 5.0, 7.5, and 10.0 weight percentages via the melt blending technique for this aim. In addition to mechanical testing such as tensile and hardness, thermal gravimetric analysis, melt flow rate, and electron microscopy (SEM) characterization methods were used on injection-molded composite samples. The structure of the pumice powder was studied using SEM/energy diffraction X-rays. Results revealed that the inclusion of pumice reduces the tensile strength and percent elongation values of TPU, but the composite sample with 2.5% pumice produced virtually equal values to the reference polymer. The hardness of the pumice increased with the loading rate. The low percentage of pumice reinforcement improved TPU's thermal stability. The melt flow rate produced varying results at different pumice ratios. As the morphological qualities were studied using electron microscopy, it was determined that the pumice particles were homogeneously disseminated in the TPU phase when reinforced at 2.5% and 5.0%. Based on these findings, TPU-based composites with the lowest addition quantity of 2.5% pumice produced the best outcomes. The use of pumice-filled TPU composites in automotive and construction applications can be established effectively thanks to performance improvement in the properties of examined samples.

ARTICLE INFO

Research article

Received: 05/09/2024
Accepted: 13/02/2025

Keywords:
acidic pumice, polymer composites, melt blending, thermoplastic polyurethane

*Corresponding author

1. Introduction

Porous and amorphous, pumice is a volcanic rock containing SiO_2 in its structure. The precipitation of dissolved gases forms its porous structure during the cooling of lava as it moves rapidly in the air [1,2]. Türkiye has approximately 3 billion m^3 reserves and has important acidic pumice deposits around Nevşehir, Van, and Kayseri regions [3,4]. Pumice powder is used to produce soap, toothpaste, insulation plaster, detergent, and as a cheap filling material in the plastic industry [5-7]. Pumice containing building materials such as concrete, mortar, fiber-board, phase-change, and catalysis-support materials were developed [8-12]. In these cases, weight reduction is the main strategy thanks to the characteristic microporous morphology of the pumice structure.

Pumice was compounded with various polymers for performance improvement of composite materials corresponding to the literature survey. Polymer matrices involving acidic pumice particles are epoxy resin [13-15], polypropylene [16-18], polyethylene [19-21], polyethylene terephthalate (PET) [22,23], poly (vinyl alcohol) [24,25], polyethylene glycol (PEG) [26,27], poly (lactic acid) [28], hydroxyapatite [29], poly (phenylene sulfide) [30-33], poly (hydroxyethyl methacrylate) [34], polyaniline [35,36], ethylene propylene diene rubber (EPDM) [37], poly (vinyl pyrrolidone) [38], nitrile rubber [39], poly (β-hydroxybutyrate) [40], and acrylonitrile-styrene-butadiene copolymer (ABS) [41], based on the literature. In most of these studies, the mechanical performances of resulted polymeric materials were investigated. Additionally, phase-change behavior, weight-reduction, thermal stability, fire

and wear resistance properties were enhanced in related research works.

Thermoplastic polyurethane (TPU) is preferred in industrial applications due to its recyclability, ease of processing, and high wear resistance. TPU has been used in several sectors, such as film and packaging, textiles, pharmaceuticals, sports equipment, transportation, electronics, and cables.

According to the literature, pumice additions improved thermoset polyurethane's acoustic and thermal insulation properties published by Soyaslan [42]. This study aimed to increase mechanical and physical performances and decline specific gravity and production costs via acidic pumice inclusion to TPU polymer, which is used in various application fields such as textile, logistics, construction, and medical equipment. Performance enhancement in mechanical and thermal behaviors of TPU via the pumice inclusion contributes to achieving requirements in related applications. In addition to mechanical tests, such as tensile and hardness, force measurement, thermal gravimetric analysis (TGA), melt flow rate, and scanning electron microscope (SEM) characterization methods were applied to the composite samples shaped by injection molding.

2. Materials and method

2.1.Materials

Ester-based TPU with the trade name Ravathane® R130A85 was supplied by Ravago Petrochemical, İzmir, Türkiye. Acidic pumice was supplied in ground powder form in 25-micron grain size from Yoltaş Pomza Ürünleri A.Ş., Nevşehir, Türkiye.

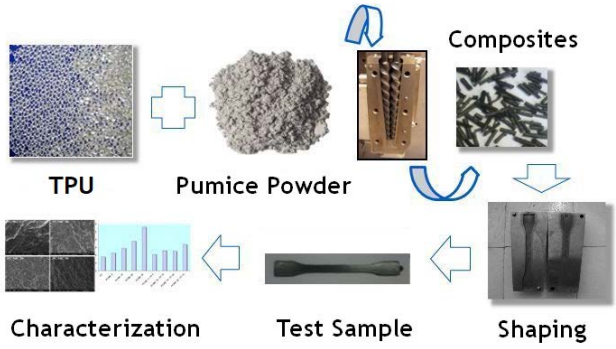

Figure 1. *Melt-compounding, injection molding, and characterization steps of composites*

2.2.Composite fabrication

TPU-based composites were produced using MC15HT (Xplore Instruments) extruder. Mixing temperature, mixing speed, and time were set as 200 ˚C, 100 rpm, and 5 min, respectively. During the preparation of the composites, acidic pumice powder was blended with TPU at 2.5, 5.0, 7.5, and 10.0 weight percent ratios using the melt blending technique. The preparation and shaping steps of the study are visualized in Fig. 1.

2.3.Characterization techniques

The particle size of basic pumice powder was analyzed with the Malvern Mastersizer 3000 particle size measuring device. Tensile test was performed to determine the stress-deformation behavior of the material. In this study, according to the ASTM D-638 standard and with the Lloyd LR 30 K tensile test device, using dog bone-shaped composites with a 5 kN load chamber and a speed of 5 cm/min. Shore hardness measurements were carried out by the Tronic brand Shore hardness device according to the ISO 7619-1 standard. The fracture surfaces of the composite samples obtained from the tensile strength test were subjected to TESCAN MAIA3 analytical scanning electron microscope, and SEM images were taken with x1000, x2500, and x5000 magnifications. X-ray fluorescence (XRF) and energy diffraction X-ray (EDS) analyses of pumice powders were also performed using the same device. Hitachi STA 7300 brand thermogravimetric analyzer was utilized to evaluate thermogravimetric analysis (TGA) of composites in the range of 25-600 °C and at a speed of 10 °C/min. MFI (melt flow index) values are indicative parameters for thermoplastics in the case of processability. MFI values of the produced samples were determined via the Coesfeld Melt-Flixer device in accordance with a standard load of 2.16 kg. Xplore Instruments software was used to measure the force values during the extrusion process. The screw force values in the melt were determined using the software of the micro-mixer as a function of the mixing time.

3. Results and Discussion

The elemental content of the supplied pumice powder was obtained by EDS analysis and displayed in Fig. 2.
According to Fig. 2, it was observed that acidic pumice was rich in silica (SiO_2) with 63.9% composition. Other parts of AP contained metal oxides, mainly Al_2O_3, Fe_2O_3, SO_3, PbO, ZnO, K_2O, and MnO.

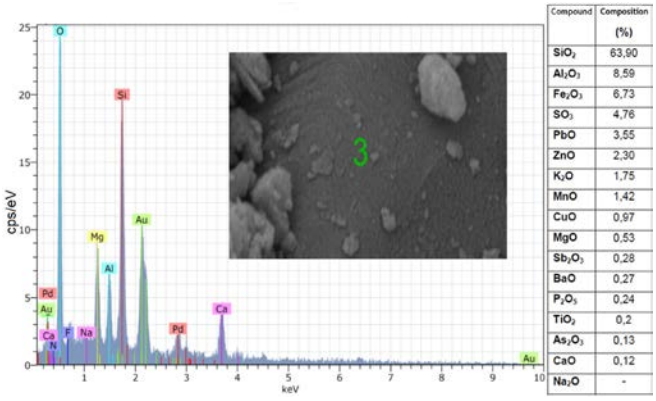

Compound	Composition (%)
SiO_2	63,90
Al_2O_3	8,59
Fe_2O_3	6,73
SO_3	4,76
PbO	3,55
ZnO	2,30
K_2O	1,75
MnO	1,42
CuO	0,97
MgO	0,53
Sb_2O_3	0,28
BaO	0,27
P_2O_5	0,24
TiO_2	0,2
As_2O_3	0,13
CaO	0,12
Na_2O	-

Figure 2. *EDS data of AP*

Force measurement provides experimental data for planning the production of the resulting composite materials before the large-scale production stages. As seen from the extrusion force of different mixing ratios of TPU and AP against time in Fig. 3, it was found to be AP additions cause an increase in the mixing force values due to the addition of powder, which improves the wear force because of the increased melt viscosity during the extrusion process. Similarly, a high amount of mineral filler loadings resulted in a remarkable increase in mixing force values in accordance with the studies in the literature dealt with the polymers involving minerals [43,44].

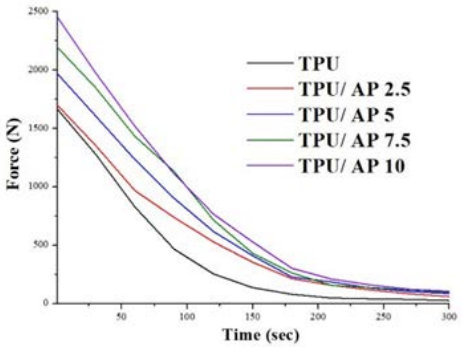

Figure 3. *Force-time graphs of TPU and composites*

The following experimental study is the tensile strength test, which is given as the graphs of tensile strength versus elongation with different mixing ratios of TPU and AP in Fig. 4. Although the tensile strength and percent elongation values of TPU are slightly reduced with the addition of acidic pumice, the composite containing 2.5% pumice presents similar values to the reference polymer. As the AP loading amount increases, the tensile strength and percent elongation values at break declined. Further additions of AP beyond the loading level of 2.5% caused pumice powder to deteriorate the composite structure by forming agglomeration. The highest tensile strength values were obtained for composite samples filled with the lowest amount of pumice powder based on the similar studies in the literature.[16,19,28].

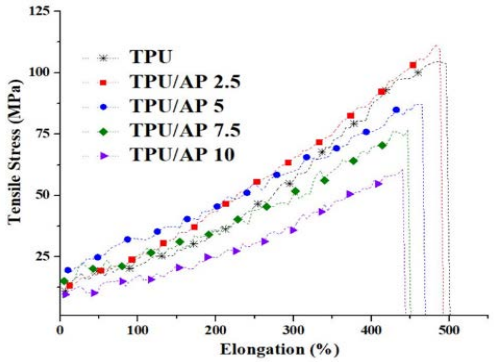

Figure 4. *Tensile test curves of TPU and composites*

The chain structure of TPU elastomer involves repeating soft and hard segments. The hard segment consists of diamine reacted with low molecular weight glycols or diisocyanate and strengthened by crosslinking. The soft segment consists of polyester or polyether units. TPU revealed a two-step degradation curve owing to isocyanate and polyol segments, respectively [45,46]. As the TGA and DTG curves of the composites are examined in Fig. 5, it was determined that especially low-ratio pumice reinforcement positively affected the thermal stability of TPU. Composites containing AP started to decompose at lower temperatures, and as the AP ratio increased, the decomposition temperature tended to decrease. According to the research works performed with pumice additive, several polymers such as polypropylene (PP) [16], polylactide (PLA) [28], and acrylonitrile-butadiene-styrene terpolymer (ABS) [41] exhibited lowering in thermal degradation after AP inclusions.

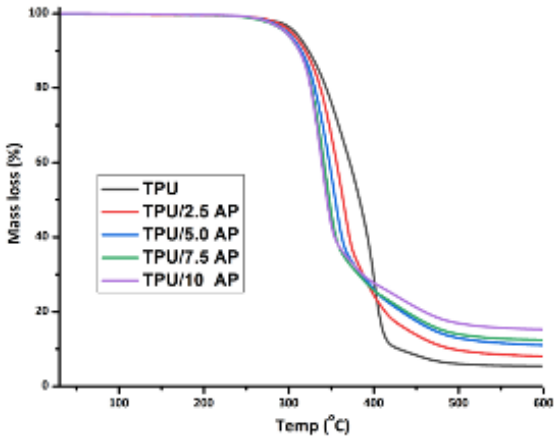

(a) TGA curves

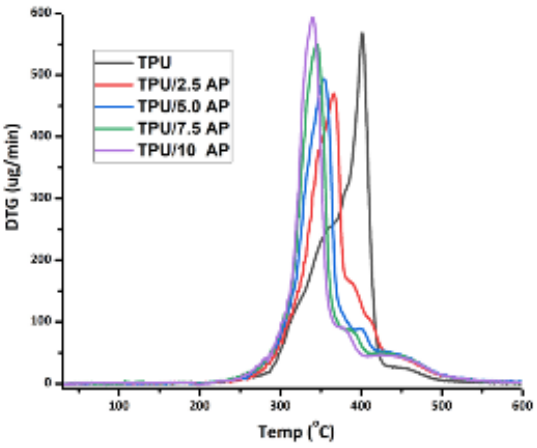

(b) DTG curves

Figure 5. *Thermo-gravimetric curves of composites*

Fig. 6 represents MFI graphs against mixing ratios of AP.

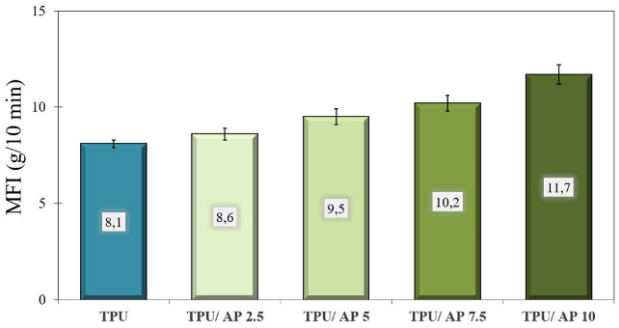

Figure 6. *MFI results of TPU and composites*

According to Fig. 6, MFI values gave variable results at different pumice ratios. The addition of AP caused an increase in the MFI value of TPU due to high specific gravity of the pumice. At low AP addition percentages, closer MFI values were obtained to unfilled TPU. This finding implies that the processing stages of TPU/AP composites can take place with no serious problems since technical difficulties in injection molding can be caused by the high level of melt-flow rates such as warpage or flow-lines as well as short-shot or delamination with high MFI values.

Table 1. The *Shore A hardness values of TPU and relevant composites*

Sample	Hardness (Shore A)
TPU	85.0±0.1
TPU/ AP 2.5	85.4±0.1
TPU/ AP 5	85.7±0.2
TPU/ AP 7.5	86.1±0.1
TPU/ AP 10	86.5±0.1

Shore hardness parameters of TPU and TPU/AP composites with varied filling amounts are listed in Table 1. Shore A hardness value of unfilled TPU showed an increasing trend with the increase in pumice loading ratio. Similar results were obtained from the literature, which found that incorporating pumice enhanced the shore hardness of polymeric composites [41,47]. Improvement in shore hardness values refers to the donation of scratch resistance of composite material related to the indentation volume of the polymer surface [48].

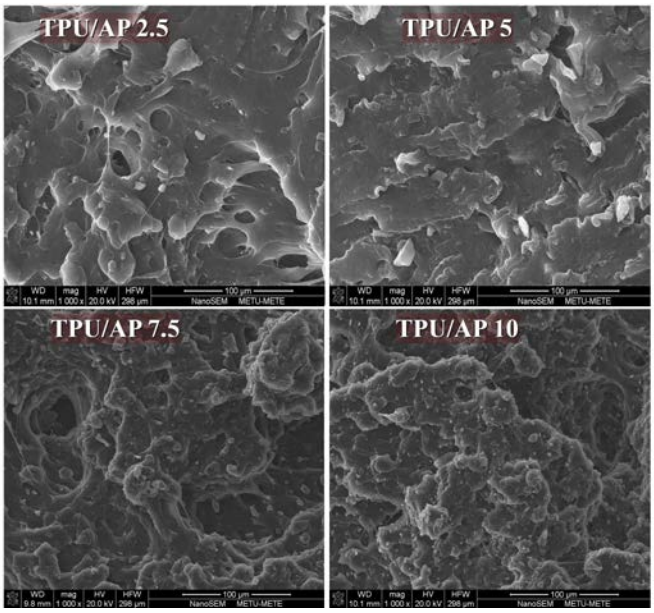

Figure 7. *SEM photographs of composites*

As the scanning electron microscope micro-photographs given in Fig. 7 are examined, it was determined that the pumice particles are homogeneously distributed within the TPU phase when their morphological structures were reinforced at 2.5% and 5.0%. The homogeneous distribution in the composite structure disappears at high AP loading rates. As visualized in Fig. 7, the agglomerated morphology of AP at high-loading amounts is the reason for obtaining a reduction in the mechanical performance of TPU/ AP 7.5 and TPU/ AP 10 composite samples. The decline in dispersion homogeneity was obtained for the morphology of mineral-filled polymeric composites according to the literature [15,20,23].

4. Conclusion

In addition to mechanical tests such as tensile and hardness, force measurement, thermal gravimetric analysis, melt flow rate, and electron microscope (SEM) characterization methods were applied to composite samples prepared by mixing acidic pumice powder with TPU using the melt blending technique at 2.5, 5.0, 7.5 and 10.0 wt% ratios. According to the results obtained, it was observed that the tensile strength and percentage elongation values of TPU increased with the addition of 2.5% AP, and these values decreased slightly with higher AP reinforcements. The shore hardness value increases with the pumice loading rate. TPU's melt-flow index increases directly proportional to the AP rate. According to TGA analysis, composites containing AP start to decompose at low temperatures compared to TPU. AP addition percentage negatively affects the thermal stability of composites. As a result of SEM characterization, pumice particles tend to exhibit homogeneous distribution in the TPU phase at low AP concentrations. Based on the findings, TPU-based composites containing the lowest

addition rate of pumice exhibited optimum results. Acidic pumice can potentially reduce costs while maintaining the performance of TPU-based composites in the case of low filling ratios. Results revealed that pumice can be used as an effective additive for TPU-based composite materials since mechanical and thermal performance increased.

Statement of conflicts of interest

There is no conflict of interest between the authors.

Author contributions

All authors contributed equally to the study.

References

[1]. Ersoy B., Sariisik A., Dikmen S., Sariisik G., "Characterization of acidic pumice and determination of its electrokinetic properties in water", Powder Technology, 197, (2010), 129–135.

[2]. Lura P., Bentz D.P., Lange D.A., Kovler K., Bentor A., "Pumice aggregates for internal water curing", International RILEM Symposium, 22–24, (2004), 137–151.

[3]. Yazıcıoğlu S., Arıcı E., Gönen T., "Pomza taşının kullanım alanları ve ekonomiye etkisi", F.Ü. DAUM Dergisi, 1, (2003), 118-123

[4]. Elmastas N., "A mine becoming increasingly important for economy of Turkey: Pumice". International Journal of Social Research, 5, (2012), 197-206

[5]. Bodude M.A., Akano T.T., Owa A. F., ''Mechanical and microstructural characterization of rubber particle reinforced thermoplastic for automobile bumper application'', MANAS Journal of Engineering, 7(2), (2019), 89-93.

[6]. Çoban O., Yilmaz T., "Volcanic particle materials in polymer composites: A review", Journal of Materials Science, 57(36), (2022), 16989-17020.

[7]. Whitham A.G., Sparks R.S.J., "Pumice", Bulletin of Volcanology, 48, (1986), 209-223.

[8]. Dayan O., Kilicer A., Bulut A., Ceylan E., Tayfun U., Uzun O., Zahmakiran M., Yurderi M., "Pumice-supported ruthenium nanoparticles as highly effective and recyclable catalyst in the hydrolysis of methylamine borane", International Journal of Hydrogen Energy, 52, (2024), 1-10.

[9]. Acet Ö., "Investigation of BSA adsorption performances of metal ıon attached mineral particles embedded cryogel discs", MANAS Journal of Engineering, 9, (2021), 65-71.

[10]. Hossain K.M., "Potential use of volcanic pumice as a construction material", Journal of Materials in Civil Engineering, 16(6), (2004), 573-577.

[11]. Kurt M., Gul M.S., Gul R., Aydin A.C., Kotan T., "The effect of pumice powder on the self compactability of pumice aggregate lightweight concrete", Construction and Building Materials, 103, (2016), 36-46.

[12]. Sari D., Pasamehmetoglu A.G., "The effects of gradation and admixture on the pumice lightweight aggregate concrete", Cement and Concrete Research, 35, (2005), 936–942.

[13]. Koyuncu M., "The influence of pumice dust on tensile, stiffness properties and flame retardant of epoxy/wood flour composites", Journal of Tropical Forest Science, 30, (2018), 89-94.

[14]. Shahapurkar K., Zelalem Y.M., Chenrayan V., Soudagar M.E., Fouad Y., Kalam M.A., Kiran M.C., "Investigation on the mechanical and fracture properties of lightweight pumice epoxy composites", Polymer Engineering & Science, 64(3), (2024), 1071-1082.

[15]. Fleischer C.A. , Zupan M., "Mechanical performance of pumice-reinforced epoxy composites", Journal of Composite Materials, 44, (2010), 2679-2696.

[16]. Kanbur Y., Tayfun U., "Mechanical, physical and morphological properties of acidic and basic pumice containing polypropylene composites", Sakarya University Journal of Science, 22, (2018), 333-339.

[17]. Almiron J., Roudet F., Duquesne S., "Influence of volcanic ash, rice husk ash, and solid residue of catalytic pyrolysis on the flame-retardant properties of polypropylene composites", Journal of Fire Science, 37(4–6), (2019), 434–451.

[18]. Sever K., Atagür M., Tunçalp M., Altay L., Seki Y., Sarıkanat M., "The effect of pumice powder on mechanical and thermal properties of polypropylene", Journal of Thermoplastic Composite Materials, 32, (2019), 1092-1106.

[19]. Wang C., Ajji A., 'Ethylene scavenging film based on low-density polyethylene incorporating pumice and potassium permanganate and its application to preserve avocados'', LWT, 172, (2022), 114200.

[20]. Han B., Sun Z., Chen Y., Tian F., Wang X., Lei Q., "Space charge distribution in low-density polyethylene (LDPE)/pumice composite", Proceedings of 9th International Conference on Properties and Applications of Dielectric Materials, China, (2009), 19-23.

[21]. Han B., Sun Z., Chen Y., Tian F., Wang X., Lei Q., ‘’Space charge distribution in Low-density Polyethylene (LDPE)/Pumice composite’’, IEEE 9th International Conference on the Properties and Applications of Dielectric Materials, (2009), 969-972.

[22]. Kurtulmus E., Karaboyacı M., Yigitarslan S., ‘’Production and characterization of a composite insulation material from waste polyethylene teraphtalates’’, AIP Conference Proceedings, 1569, (2013), 487-491.

[23]. Sari N.H., Setyawan P.D., Thiagamani S.M.K., Suteja Tamimi R., Rangappa S.M., Siengchin S., ‘’Evaluation of mechanical, thermal and morphological properties of corn husk modified pumice powder reinforced polyester composites’’, Polymer Composites, 43(3), (2022), 1763-1771.

[24]. Jayakrishnan P., Ramesan M.T., "Synthesis, characterization and properties of poly (vinyl alcohol)/chemically modified and unmodified pumice composites", Journal of Chemical and Pharmaceutical Sciences, 1, (2016) 97-104.

[25]. Ramesan M.T., Jose C., Jayakrishnan P., Anilkumar T., "Multifunctional ternary composites of poly (vinyl alcohol)/cashew tree gum/pumice particles", Polymer Composites, 39, (2018), 38-45.

[26]. Sarı A., Hekimoğlu G., Tyagi V.V., Sharma R.K., ‘’Evaluation of pumice for development of low-cost and energy-efficient composite phase change materials and lab-scale thermoregulation performances of its cementitious plasters’’, Energy, 207, (2020), 118242.

[27]. Sarı A., ‘’Composites of polyethylene glycol (PEG600) with gypsum and natural clay as new kinds of building PCMs for low temperature-thermal energy storage’’, Energy and Buildings, 69, (2014), 184-192.

[28]. Dike A.S., ‘’Türk Pomza mineralinin modifikasyonu ve poli (laktik asit) bazli biyo-kompozit malzemelerinde eklenti olarak kullanimi’’, Afyon Kocatepe Üniversitesi Fen ve Mühendislik Bilimleri Dergisi, 20(1), (2020), 111-117.

[29]. Koc S., ‘’Pumice and perlite co-substituted hydroxyapatite: Fabrication and characterization’’, MANAS Journal of Engineering, 8(2), (2020), 132-137.

[30]. Sahin A., Karsli N.G., Sinmazcelik T., "Comparison of the mechanical, thermomechanical, thermal, and morphological properties of pumice and calcium carbonate-filled poly (phenylene sulfide) composites", Polymer Composites, 37, (2016), 3160-3166.

[31]. Bora M.Ö., Çoban O., Kutluk T., Fidan S., Sinmazçelik T., "The influence of heat treatment process on mechanical properties of surface treated volcanic ash particles/polyphenylene sulfide composites", Polymer Composites, 39, (2018), 1604–1611.

[32]. Sahin A., Yildiran Y., Avcu E., Fidan S., Sinmazcelik T., "Mechanical and thermal properties of pumice powder filled PPS composites", Acta Physica Polonica A, 2, (2014), 518-520.

[33]. Avcu E., Coban O., Bora M.O., Fidan S., Sinmazcelik T., Ersoy O., "Possible use of volcanic ash as a filler in Polyphenylene Sulfide composites: thermal, mechanical, and erosive wear properties", Polymer Composites, 35, (2014), 1826–1833.

[34]. Akkaya R., "Uranium and thorium adsorption from aqueous solution using a novel polyhydroxyethylmethacrylate-pumice composite", Journal of Environmental Radioactivity, 120, (2013), 58-63.

[35]. Yılmaz K., Akgoz A., Cabuk M., Karaagac H., Karabulut O., Yavuz M., "Electrical transport, optical and thermal properties of polyaniline–pumice composites", Material Chemistry and Physics, 130, (2011), 956-961.

[36]. Gok A., Gode F., Turkaslan B.E., "Synthesis and characterization of polyaniline/pumice composite", Material Science and Engineering B, 133, (2006), 20-25.

[37]. Rahmaniar S.T., Prasetya H.A., Marlina P., Purbaya M., Chalid M., Hasan A., ‘’The effect of pumice and clay composition in natural rubber-ethylene propylene diene monomer blends towards its curing characteristics and physic-mechanical properties’’, Material Science and Engineering, 980, (2020), 012003.

[38]. Ramesan M.T., George A., Jayakrishnan P., Kalaprasad G., "Role of pumice particles in the thermal, electrical and mechanical properties of poly(vinyl alcohol)/poly(vinyl pyrrolidone) composites", Journal of Thermal Analysis and Calorimetry, 126, (2016), 511-519.

[39]. El-Nemr K.F., Radi H., Helal R.H., ‘’Partial replacement of silica by naturally occurring pumice powder for enhancing mechanical and thermal properties of nitrile rubber cured by electron beam irradiation’’, Pigment & Resin Technology, 53(4), (2022), 442-449.

[40]. Alvarado S., Morales K., Srubar W., Billington S., "Effects of natural porous additives on the tensile mechanical performance and moisture absorption behavior of PHBV-based composites for construction", Stanford Undergrad Research Journal, 10, (2011), 30-35.

[41]. Tayfun Ü., Tirkeş S., Doğan M., Tirkeş S., Zahmakıran M., ‘’Comparative performance study of acidic pumice and basic pumice inclusions for acrylonitrile–butadiene–styrene-based composite filaments’’, 3D Printing and Additive Manufacturing, 11(1), (2024), 276-286.

[42]. Soyaslan I.I., "Thermal and sound insulation properties of pumice/polyurethane composite material", Emerging Materials Research, 9(3), (2020), 859-867.

[43]. Akar A.Ö., Yıldız Ü.H., Tayfun Ü., "Halloysite nanotube loaded polyamide nanocomposites: Structural, morphological, mechanical, thermal and processing behaviors.", AIP Conference Proceedings. 2607(1), (2023), 070005.

[44]. Aksoy E., Tirkeş S., Tayfun Ü., Tirkeş S., ‘’Expanded perlite mineral as a natural additive used in polylactide-based biodegradable composites’’, Turkish Journal of Science and Technology, 19(1), (2023), 113-122.

[45]. Herrera M., Matuschek G., Kettrup A., ‘’Thermal degradation of thermoplastic polyurethane elastomers (TPU) based on MDI’’, Polymer Degradation and Stability, 78(2), (2002), 323-331.

[46]. Wei Z., Chen X., Jiao C., ‘’Thermal degradation and flame retardancy of fumaric acid in thermoplastic polyurethane elastomer’’, Polymers for Advanced Technologies, 30(2), (2019), 475-482.

[47]. Yurderi M., Tayfun Ü., Bulut A., ‘’Development of polyurethane elastomer-based bio-composites reinforced with basaltic pumice’’, Journal of the Institute of Science and Technology, 14(4), (2024), 1622-1631.

[48]. Chu J., Xiang C., Sue H.J., Hollis, R.D., ‘’Scratch resistance of mineral-filled polypropylene materials’’, Polymer Engineering & Science, 40(4), (2000), 944-955.

MANAS Journal of Engineering
ISSN 1694-7398 | e-ISSN 1694-7398

Volume 13, Issue 1, (2025) Pages 30-39
https://doi.org/10.51354/mjen.1575022

An investigation into the asymptotic stability analysis of delayed *q*-fractional neutral systems

Yener ALTUN

Yuzuncu Yil University, Van, Türkiye, yeneraltun@yyu.edu.tr, ORCID: 0000-0003-1073-5513

ABSTRACT

This research analyzes the asymptotic stability of delayed *q*-fractional neutral systems. By developing suitable Lyapunov-Krasovskii functionals (LKFs), certain sufficient conditions for asymptotic stability are derived using linear matrix inequalities (LMIs). The approach used in this paper relies on directly calculating the quantum derivatives of the LKFs. Lastly, we provide two numerical examples to demonstrate how our theoretical findings can be applied.

ARTICLE INFO

Research article

Received: 28.10.2024
Accepted: 12.03.2025

Keywords:
asymptotic stability, q-fractional neutral systems, LKF, LMI.

1. Introduction

Time delays in information flow within different components of dynamic systems often lead to instability and are commonly observed in various engineering applications, including chemical processes, long-distance transmission lines, and microwave oscillators. Due to their ability to model natural phenomena more effectively than ordinary differential equations, fractional calculus have garnered significant attention from scholars worldwide. Therefore, mathematicians in particular currently appear to have a strong interest in fractional calculus. It is well known that neutral systems, which are of a more general class than those of the delayed type, have been an active area of research in recent years. The stability of neutral systems has proven to be a more complex question, since the system under consideration involves the derivation of the delayed state. In particular, over the past few decades, numerous books and articles have been explored concerning retarded-type or neutral-type differential and fractional differential systems. In this sense, the stability problem, which is one of the important problems in theoretical and practical applications, is considered an index in the study of fractional systems, and numerous articles have addressed different types of stability in such systems without delay and delay. Fractional systems, both with and without time-varying delays, frequently appear in various scientific disciplines, including fields such as engineering, physics, biophysics, polymer rheology, blood flow dynamics, control theory, biology, and signal processing (see [1–37] and references therein).

Based on insights from the relevant literature, fractional calculus often provide a more accurate description of natural phenomena compared to ordinary differential equations. Consequently, this topic has been widely explored by numerous renowned scientists (see [36]). For those interested, several studies in this rapidly growing field are listed below.

The q-fractional calculus, which was brought to the attention of researchers by some q-fractional derivatives and q-fractional integrals, was first discussed by Agarwal [1] and Al-salam [3] in 1969. In [8], Chartbupapan et al. explored the asymptotic stability of nonlinear fractional Riemann-Liouville (RL) differential equations with a fixed delay and included examples to demonstrate the validity of the conditions they established. In [29], presented a simple mathematical approach to explain when and why fractional Brownian motion is appropriate for economic modeling. In [27], various physical implications examined that are pertinent to dynamical processes in complex systems. In [25], three bioengineering research areas bio electrodes, biomechanics, and bioimaging are described, which have been utilized to develop new mathematical models based on fractional calculus. In [11], Jarad et al. examined the conditions for stability, uniform stability, and asymptotic stability within the framework of non-autonomous Caputo fractional derivatives using the Lyapunov direct method. In [24], Lu et al. derived various sufficient conditions for the asymptotic stability and Mittag-Leffler stability of fractional nonlinear neutral singular systems using the Lyapunov direct method. Zhang et al. [37], on the other hand, studied the

global asymptotic stability of delayed fractional RL neural networks. Additionally, several books on these topics can be referenced. Examples include works on q-fractional calculus [5, 10, 12], fractional calculus [13, 28], and singular systems [33, 36]. Drawing inspiration from the studies mentioned above and their references, we have focused on nonlinear time delay q-fractional neutral systems.

It is observed that the stability method in the majority of studies concerning system stability in control theory is primarily based on LMIs and Lyapunov stability theory, as seen in references [4, 6, 9, 15–23, 30]. The Lyapunov direct method plays a central role in investigating stability in differential equations. The LKF explicitly incorporates terms that account for time delays in the system (including distributed or discrete delays). This allows it to effectively model the dynamic behavior of systems where the current state depends not only on the current time but also on past states.In contrast, classical Lyapunov functions typically focus on delay-free systems or only handle delays in an approximate or conservative manner. Advantage of LKF, by including integral terms related to the delay, LKFs provide a more flexible structure for capturing the dynamics of time-delay systems. This often leads to less conservative stability conditions, allowing more accurate determination of the system's stability region. In this research, the proof technique relies on fundamental inequalities, LMIs, and the Lyapunov functional approach.

In comparison to the existing literature, the main contributions of this paper can be succinctly outlined as follows:

(i) This study relies on the LMI and the direct calculation of quantum derivatives of LKFs. Therefore, there is no need to compute the fractional-order derivative of the Lyapunov functional. The derived stability criteria are formulated as LMIs, making them both convenient and effective for testing the asymptotically stability of the considered systems.

(ii) In this study, motivated by the above-mentioned findings, the asymptotically stability of time-delayed nonlinear q-fractional neutral systems is investigated by developing appropriate LKFs;

(iii) In this study, several delay dependent sufficient conditions for asymptotic stability are derived.

(iv) In this study believe that the theoretical results obtained are both intriguing and contemporary, providing a significant contribution to the existing literature. When the studies on stability analysis of q-fractional neutral systems are examined, the equation system considered in this research is new and generalizes similar studies in the related literature.

In this study, we describe delayed q-fractional neutral systems. In addition, we introduce fundamental definitions and properties of quantum calculus, along with q-fractional integrals and derivatives. Next, using the Lyapunov method, we derive sufficient conditions to demonstrate the asymptotic stability of the considered system, leveraging foundational information and inequalities.
Consider the following delayed nonlinear q-fractional system:

$$\begin{aligned}\nabla_q^{\alpha} x(t) = Ax(t) + Bx(t-\tau) + C\nabla_q^{\alpha} x(t-\tau) + Df(x(t)) \\ + Ef(x(t-\tau)) + Ff(\nabla_q^{\alpha} x(t-\tau)), \quad t \geq 0,\end{aligned} \tag{1}$$

with the initial value condition as follows:

$$I_q^{1-\alpha} x(t) = \varphi(t), \quad t \in [-\tau, 0], \quad 0 < \alpha < 1,$$

where the state vector $x(t) \in \mathbb{R}^n, \tau < 0$ is a constant time delay, $A, B, B, D, E, F \in \mathbb{R}^{n\times n}$ are constant system matrices, $f(x(t)), f(x(t-\tau))$ and $f\left(\nabla_q^{\alpha} x(t-\tau)\right) \in \mathbb{R}^n$represent the nonlinear terms of system (1), which satisfy that

$$\begin{aligned}\left\| f(x(t)) \right\| &\leq \eta_1 \left\| x(t) \right\| \\ \left\| f(x(t-\tau)) \right\| &\leq \eta_2 \left\| x(t-\tau) \right\| \\ \left\| f(\nabla_q^{\alpha} x(t-\tau)) \right\| &\leq \eta_3 \left\| \nabla_q^{\alpha} x(t-\tau) \right\|\end{aligned} \tag{2}$$

where η_1, η_2 and η_3 are positive real constants. Constraints described by (2) can be rewritten as follows

$$\begin{aligned}f^T(x(t)) f(x(t)) &\leq \eta_1^2 x^T(t) x(t) \\ f^T(x(t-\tau)) f(x(t-\tau)) &\leq \eta_2^2 x^T(t-\tau) x(t-\tau) \\ f^T(\nabla_q^{\alpha} x(t-\tau)) f(\nabla_q^{\alpha} x(t-\tau)) &\leq \eta_3^2 (\nabla_q^{\alpha} x(t-\tau))^T (\nabla_q^{\alpha} x(t-\tau)).\end{aligned} \tag{3}$$

Definition 1 ([28]) The RL fractional integral of order $p > 0$ of function g is described as

$$ {}_{t_0} D_t^{-p} \{g(t)\} = \frac{1}{\Gamma(p)} \int_{t_0}^{t} (t-s)^{p-1} g(s) ds, \quad t \geq t_0 .$$

Definition 2 ([28]) The RL fractional derivative of order p for a function g is described as

$$ {}_{t_0}^{RL}D_t^p\{g(t)\} = \frac{1}{\Gamma(n-p)}\frac{d^n}{dt^n}\int_{t_0}^{t}\frac{g(s)}{(t-s)^{p-n+1}}ds, $$

where $0 \le n-1 \le p < n, n \in Z^+$ and Γ denotes the Gamma function.

Definition 3 ([7]). For $q \in (0,1)$, $T_q = \{q^n : n \in Z\} \cup \{0\}$ is defined as time scale, where Z is the set of all integers.

Definition 4 ([11]). The trivial solution $x(t) = 0$ of system (1) is said to be

1. Stable, if for each $\varepsilon > 0$ and $t_0 \in T_q$, there exists $\delta = \delta(\varepsilon, t_0) > 0$ such that for any solution $x(t) = x(t, t_0, \varphi)$ with $\varphi(t) < \delta$, we always have $\|x(t)\| < \varepsilon$, for all $t \in T_q$, $t \ge t_0$;
2. Uniformly stable, if it is stable and δ depends only ε;
3. Asymptotically stable, if it is stable and for all $t_0 \in T_q$, there exists $\delta = \delta(t_0) > 0$ such that if $\varphi(t) < \delta$ implies that $\lim_{t\to\infty} x(t, t_0, \varphi) = 0$.

Lemma 1 ([37]). Assume that $S \in \mathbb{R}^{n\times n}, S = S^T > 0$, is a constant matrix and $x(t) \in \mathbb{R}^n$ be a vector of q-fractional differentiable function. Therefore, $\forall t \in T_q$, $t > 0$,

$$ \nabla_q^\alpha (x^{\mathrm{T}}(t)Sx(t)) \le 2x^{\mathrm{T}}(t)S\nabla_q^\alpha x(t), \quad 0 < \alpha < 1, $$

is satisfied.

Lemma 2 ([19]). The homogeneous difference operator $\Theta: \mathbb{R}([-\tau, 0], \mathbb{R}^n) \longrightarrow \mathbb{R}^n$ is defined to be $\Theta: \Theta(x_t) = x(t) - Cx(t-\tau)$. The operator Θ is stable if $\|C\| < 1$.

The notations listed below will be employed throughout this research: $\mathbb{R}$ denotes the set of all real numbers; n represent the dimension of the space; $\mathbb{R}^n$ represents the space of all n -tuples of real numbers: $\mathbb{R}^n = \{(x_1, x_2, \dots, x_n) | x_i \in \mathbb{R}^n, i = 1,2, \dots, n\}$; $\|.\|$ represents the Euclidean norm for vectors; A^T means the transpose of the matrix A; B is symmetric if $B = B^T$; C is positive definite (or negative definite) if $\langle Cx, x\rangle > 0$ (or $\langle Cx, x\rangle < 0$) for all $x \ne 0$; $\|D\|$ represents the spectral norm of matrix D; "*" means conjugate transpose.

2. Main results

We first present a result for the asymptotically stable of the trivial solution of system (1) with $D = E = F = 0$, as follows

$$ \nabla_q^\alpha x(t) = Ax(t) + Bx(t-\tau) + C\nabla_q^\alpha x(t-\tau), \ t > 0. \qquad (4) $$

Theorem 2.1 For given scalar $\tau > 0$, the trivial solution of system (4) is asymptotically stable, if $\|C\| < 1$ and there exist symmetric positive definite matrices P, Q, S and U such that the following LMI holds:

$$ \Pi = \begin{bmatrix} \Pi_{11} & \Pi_{12} & \Pi_{13} \\ * & \Pi_{22} & \Pi_{23} \\ * & * & \Pi_{33} \end{bmatrix} < 0. \qquad (5) $$

where,

$$ \Pi_{11} = PA + A^T P + Q + A^T(S + \tau U)A, $$
$$ \Pi_{12} = PB + A^T(S + \tau U)B, $$
$$ \Pi_{13} = PC + A^T(S + \tau U)C, $$
$$ \Pi_{22} = B^T(S + \tau U)B - Q, $$
$$ \Pi_{23} = B^T(S + \tau U)C, $$
$$ \Pi_{33} = C^T(S + \tau U)C - S. $$

Proof. Let us select the following Lyapunov-Krasovskii functional

$$ V(x(t)) = I_q^{1-\alpha}(x^{\mathrm{T}}(t)Px(t)) + \int_{t-\tau}^{t} x^{\mathrm{T}}(s)Qx(s)\nabla_q s $$
$$ + \int_{t-\tau}^{t} \nabla_q^\alpha x^T(s)S\nabla_q^\alpha x(s)\nabla_q s $$
$$ + \int_{t-\tau}^{t}\int_{\theta}^{t} \nabla_q^\alpha x^T(s)U\nabla_q^\alpha x(s)\nabla_q s\nabla_q \theta. $$

Clearly, $V(t) > 0$. Let $\Psi(t) = \int_{t-\tau}^{t}\int_{\theta}^{t} \nabla_q^\alpha x^T(s)U\nabla_q^\alpha x(s)\nabla_q s\nabla_q \theta.$

Based on the preceding results, we obtain

$$ \nabla_q \Psi(t) = \nabla_q^\alpha \left(\int_{t-\tau}^{t}\int_{0}^{t} \nabla_q^\alpha x^T(s)U\nabla_q^\alpha x(s)\nabla_q s\nabla_q \theta \right. $$
$$ \left. - \int_{t-\tau}^{t}\int_{0}^{\theta} \nabla_q^\alpha x^T(s)U\nabla_q^\alpha x(s)\nabla_q s\nabla_q \theta \right) $$

$$
\begin{aligned}
&= \nabla_q^{\alpha}\left(\tau \int_0^t \nabla_q^{\alpha} x^T(s) U \nabla_q^{\alpha} x(s) \nabla_q s \right. \\
&\quad \left. - \int_{t-\tau}^{t} \int_0^{\theta} \nabla_q^{\alpha} x^T(s) U \nabla_q^{\alpha} x(s) \nabla_q s \nabla_q \theta \right) \\
&= \tau \nabla_q^{\alpha} x^T(t) U \nabla_q^{\alpha} x(t) \\
&\quad - \int_{t-\tau}^{t} \nabla_q^{\alpha} x^T(s) U \nabla_q^{\alpha} x(s) \nabla_q s. \qquad (6)
\end{aligned}
$$

From $\nabla_q^{\alpha} I_q^{\beta} f(t) = \nabla_q^{\alpha-\beta} f(t),\ \alpha > \beta \geq 0$ and (6), we can derive the q-derivate of $V(t)$ along the trajectories of the system (4), we can write the as follows:

$$
\begin{aligned}
\nabla_q V(x(t)) &= \nabla_q^{\alpha}(x^T(t) P x(t)) + x^T(t) Q x(t) \\
&\quad - x^T(t-\tau) Q x(t-\tau) + \nabla_q^{\alpha} x^T(t) S \nabla_q^{\alpha} x(t) \\
&\quad - \nabla_q^{\alpha} x^T(t-\tau) S \nabla_q^{\alpha} x(t-\tau) \\
&\quad + \tau \nabla_q^{\alpha} x^T(t) U \nabla_q^{\alpha} x(t) \\
&\quad - \int_{t-\tau}^{t} \nabla_q^{\alpha} x^T(s) U \nabla_q^{\alpha} x(s) \nabla_q s. \qquad (7)
\end{aligned}
$$

Since U is positive definite matrix, then

$$
\int_{t-\tau}^{t} \nabla_q^{\alpha} x^T(s) U \nabla_q^{\alpha} x(s) \nabla_q s = \int_0^{\tau} \nabla_q^{\alpha} x^T(t-s) U \nabla_q^{\alpha} x(t-s) \nabla_q s \geq 0. \qquad (8)
$$

From (7)-(8), then

$$
\begin{aligned}
\nabla_q V(x(t)) &\leq \nabla_q^{\alpha}(x^T(t) P x(t)) + x^T(t) Q x(t) \\
&\quad - x^T(t-\tau) Q x(t-\tau) + \nabla_q^{\alpha} x^T(t) S \nabla_q^{\alpha} x(t) \\
&\quad - \nabla_q^{\alpha} x^T(t-\tau) S \nabla_q^{\alpha} x(t-\tau) \\
&\quad + \tau \nabla_q^{\alpha} x^T(t) U \nabla_q^{\alpha} x(t) \qquad (9)
\end{aligned}
$$

From Lemma 1, we obtain

$$
\begin{aligned}
&\nabla_q^{\alpha}(x^T(t) P x(t)) \leq 2 x^T(t) P \nabla_q^{\alpha} x(t) \\
&= 2 x^T(t) P \left(A x(t) + B x(t-\tau) + C \nabla_q^{\alpha} x(t-\tau) \right) \\
&= x^T(t)(PA + A^T P) x(t) + 2 x^T(t) P B x(t-\tau) \\
&\quad + 2 x^T(t) P C \nabla_q^{\alpha} x(t-\tau) \qquad (10)
\end{aligned}
$$

and

$$
\nabla_q^{\alpha} x^T(t)(S + \tau U) \nabla_q^{\alpha} x(t) = \left(A x(t) + B x(t-\tau) + C \nabla_q^{\alpha} x(t-\tau) \right)
$$

$$
\begin{aligned}
&(S + \tau U)\left(A x(t) + B x(t-\tau) + C \nabla_q^{\alpha} x(t-\tau) \right) \\
&= x^T(t) A^T (S + \tau U) A x(t) \\
&\quad + x^T(t) A^T (S + \tau U) B x(t-\tau) \\
&\quad + x^T(t) A^T (S + \tau U) C \nabla_q^{\alpha} x(t-\tau) \\
&\quad + x^T(t-\tau) B^T (S + \tau U) A x(t) \\
&\quad + x^T(t-\tau) B^T (S + \tau U) B x(t-\tau) \\
&\quad + x^T(t-\tau) B^T (S + \tau U) C \nabla_q^{\alpha} x(t-\tau) \\
&\quad + (\nabla_q^{\alpha} x(t-\tau))^T C^T (S + \tau U) A x(t) \\
&\quad + (\nabla_q^{\alpha} x(t-\tau))^T C^T (S + \tau U) B x(t-\tau) \\
&\quad + (\nabla_q^{\alpha} x(t-\tau))^T C^T (S + \tau U) C \nabla_q^{\alpha} x(t-\tau) \qquad (11)
\end{aligned}
$$

Substituting (10) and (11) into (9), we get

$$
\nabla_q V(x(t)) \leq \Xi^T \Pi \Xi, \qquad (12)
$$

where

$$
\Xi = \left(x^T(t) \quad x^T(t-\tau) \quad (\nabla_q^{\alpha} x(t-\tau))^T \right)^T
$$

and the matrix Π, is defined with (5).

From (5) and (12), $\nabla_q V(t) < 0$. Since the the conditions outlined in Theorem 2.1 are met, the trivial solution of the linear q-fractional system (1) is asymptotically stable.

The following theorem presents the asymptotically stability of the trivial solution of the system (1), which is another main result of this study.

Theorem 2.2 For given scalars $\tau, \eta_1, \eta_2, \eta_3 > 0$ and $\varepsilon_1, \varepsilon_2, \varepsilon_3 \geq 0$, the trivial solution of system (1) is asymptotically stable, if $\|C\| < 1$ and there exist symmetric positive definite matrices P, Q, S, U and W such that the following LMI holds:

$$
\Delta = \begin{bmatrix}
\Delta_{11} & \Delta_{12} & \Delta_{13} & \Delta_{14} & \Delta_{15} & \Delta_{16} \\
* & \Delta_{22} & \Delta_{23} & \Delta_{24} & \Delta_{25} & \Delta_{26} \\
* & * & \Delta_{33} & \Delta_{34} & \Delta_{35} & \Delta_{36} \\
* & * & * & \Delta_{44} & \Delta_{45} & \Delta_{46} \\
* & * & * & * & \Delta_{55} & \Delta_{56} \\
* & * & * & * & * & \Delta_{66}
\end{bmatrix} < 0, \qquad (13)
$$

where,

$$
\Delta_{11} = PA + A^T P + Q + A^T (S + \tau U) A + \varepsilon_1 \eta_1^2 I,
$$

$$
\Delta_{12} = PB + A^T (S + \tau U) B,
$$

$$\Delta_{13} = PC + A^T(S+\tau U)C,$$
$$\Delta_{14} = PD + A^T(S+\tau U)D,$$
$$\Delta_{15} = PE + A^T(S+\tau U)E,$$
$$\Delta_{16} = PF + A^T(S+\tau U)F,$$
$$\Delta_{22} = B^T(S+\tau U)B + \varepsilon_2\eta_2^2 I - Q,$$
$$\Delta_{23} = B^T(S+\tau U)C,$$
$$\Delta_{24} = B^T(S+\tau U)D,$$
$$\Delta_{25} = B^T(S+\tau U)E,$$
$$\Delta_{26} = B^T(S+\tau U)F,$$
$$\Delta_{33} = C^T(S+\tau U)C + \varepsilon_3\eta_3^2 I - S,$$
$$\Delta_{34} = C^T(S+\tau U)D,$$
$$\Delta_{35} = C^T(S+\tau U)E,$$
$$\Delta_{36} = C^T(S+\tau U)F,$$
$$\Delta_{44} = W + D^T(S+\tau U)D - \varepsilon_1 I,$$
$$\Delta_{45} = D^T(S+\tau U)E,$$
$$\Delta_{46} = D^T(S+\tau U)F,$$
$$\Delta_{55} = E^T(S+\tau U)E - \varepsilon_2 I - W,$$
$$\Delta_{56} = E^T(S+\tau U)F,$$
$$\Delta_{66} = F^T(S+\tau U)F - \varepsilon_3 I.$$

Proof. Let us select the following Lyapunov-Krasovskii functional

$$V(x(t)) = I_q^{1-\alpha}(x^{\mathrm{T}}(t)Px(t)) + \int_{t-\tau}^{t} x^{\mathrm{T}}(s)Qx(s)\nabla_q s + \int_{t-\tau}^{t} \nabla_q^\alpha x^T(s)S\nabla_q^\alpha x(s)\nabla_q s + \int_{t-\tau}^{t}\int_{\theta}^{t} \nabla_q^\alpha x^T(s)U\nabla_q^\alpha x(s)\nabla_q s\nabla_q\theta + \int_{t-\tau}^{t} f^{\mathrm{T}}(x(s))Wf(x(s))\nabla_q s.$$

Clearly, $V(t) > 0$. Let $\Psi(t) = \int_{t-\tau}^{t}\int_{\theta}^{t} \nabla_q^\alpha x^T(s)U\nabla_q^\alpha x(s)\nabla_q s\nabla_q\theta.$

Based on the preceding results, we obtain

$$\begin{aligned}\nabla_q\Psi(t) &= \nabla_q^\alpha\left(\int_{t-\tau}^{t}\int_{0}^{t} \nabla_q^\alpha x^T(s)U\nabla_q^\alpha x(s)\nabla_q s\nabla_q\theta - \int_{t-\tau}^{t}\int_{0}^{\theta} \nabla_q^\alpha x^T(s)U\nabla_q^\alpha x(s)\nabla_q s\nabla_q\theta\right)\\ &= \nabla_q^\alpha\left(\tau\int_{0}^{t} \nabla_q^\alpha x^T(s)U\nabla_q^\alpha x(s)\nabla_q s - \int_{t-\tau}^{t}\int_{0}^{\theta} \nabla_q^\alpha x^T(s)U\nabla_q^\alpha x(s)\nabla_q s\nabla_q\theta\right)\\ &= \tau\nabla_q^\alpha x^T(t)U\nabla_q^\alpha x(t) - \int_{t-\tau}^{t} \nabla_q^\alpha x^T(s)U\nabla_q^\alpha x(s)\nabla_q s. \end{aligned} \tag{14}$$

From $\nabla_q^\alpha I_q^\beta f(t) = \nabla_q^{\alpha-\beta} f(t)$, $\alpha > \beta \geq 0$ and (14), we can derive the q-derivate of $V(t)$ along the trajectories of the system (1), we can write the as follows:

$$\begin{aligned}\nabla_q V(x(t)) &= \nabla_q^\alpha(x^T(t)Px(t)) + x^T(t)Qx(t)\\ &\quad - x^T(t-\tau)Qx(t-\tau) + \nabla_q^\alpha x^T(t)S\nabla_q^\alpha x(t)\\ &\quad - \nabla_q^\alpha x^T(t-\tau)S\nabla_q^\alpha x(t-\tau)\\ &\quad + \tau\nabla_q^\alpha x^T(t)U\nabla_q^\alpha x(t)\\ &\quad - \int_{t-\tau}^{t} \nabla_q^\alpha x^T(s)U\nabla_q^\alpha x(s)\nabla_q s\\ &\quad + f^T(x(t))Wf(x(t))\\ &\quad - f^T(x(t-\tau))Wf(x(t-\tau)) \end{aligned} \tag{15}$$

Since U is positive definite matrix, then

$$\int_{t-\tau}^{t} \nabla_q^\alpha x^T(s)U\nabla_q^\alpha x(s)\nabla_q s = \int_{0}^{\tau} \nabla_q^\alpha x^T(t-s)U\nabla_q^\alpha x(t-s)\nabla_q s \geq 0. \tag{16}$$

From (15)-(16), then

$$\begin{aligned}\nabla_q V(x(t)) &\leq \nabla_q^\alpha(x^T(t)Px(t)) + x^T(t)Qx(t)\\ &\quad - x^T(t-\tau)Qx(t-\tau) + \nabla_q^\alpha x^T(t)S\nabla_q^\alpha x(t)\\ &\quad - \nabla_q^\alpha x^T(t-\tau)S\nabla_q^\alpha x(t-\tau)\\ &\quad + \tau\nabla_q^\alpha x^T(t)U\nabla_q^\alpha x(t)\\ &\quad + f^T(x(t))Wf(x(t))\\ &\quad - f^T(x(t-\tau))Wf(x(t-\tau)) \end{aligned} \tag{17}$$

From Lemma 1, we get

$$\begin{aligned}\nabla_q^\alpha(x^T(t)Px(t)) &\leq 2x^T(t)P\nabla_q^\alpha x(t)\\ &= 2x^T(t)P\big(Ax(t) + Bx(t-\tau)\end{aligned}$$

$$
\begin{aligned}
&+C\nabla_q^{\alpha}x(t-\tau)+Df(x(t))\\
&+Ef(x(t-\tau))+Ff(\nabla_q^{\alpha}x(t-\tau))\big)\\
&=x^T(t)(PA+A^TP)x(t)\\
&+2x^T(t)PBx(t-\tau)\\
&+2x^T(t)PC\nabla_q^{\alpha}x(t-\tau)\\
&+2x^T(t)PDf(x(t))\\
&+2x^T(t)PEf(x(t-\tau))\\
&+2x^T(t)PFf(\nabla_q^{\alpha}x(t-\tau)) \qquad (18)
\end{aligned}
$$

and

$$
\begin{aligned}
\nabla_q^{\alpha}x^T(t)(S+\tau U)\nabla_q^{\alpha}x(t)&=(Ax(t)+Bx(t-\tau)\\
&+C\nabla_q^{\alpha}x(t-\tau)+Df(x(t))+Ef(x(t-\tau))\\
&+Ff(\nabla_q^{\alpha}x(t-\tau)))(S+\tau U)\big(Ax(t)+Bx(t-\tau)\\
&+C\nabla_q^{\alpha}x(t-\tau)+Df(x(t))+Ef(x(t-\tau))\\
&+Ff(\nabla_q^{\alpha}x(t-\tau)))\\
&=x^T(t)A^T(S+\tau U)Ax(t)+x^T(t)A^T(S+\tau U)\\
&Bx(t-\tau)+x^T(t)A^T(S+\tau U)C\nabla_q^{\alpha}x(t-\tau)\\
&+x^T(t)A^T(S+\tau U)Df(x(t))+x^T(t)A^T(S+\tau U)E\\
&f(x(t-\tau))+x^T(t)A^T(S+\tau U)Ff(\nabla_q^{\alpha}x(t-\tau)))\\
&+x^T(t-\tau)B^T(S+\tau U)Ax(t)+x^T(t-\tau)B^T\\
&(S+\tau U)Bx(t-\tau)+x^T(t-\tau)B^T(S+\tau U)C\\
&\nabla_q^{\alpha}x(t-\tau)+x^T(t-\tau)B^T(S+\tau U)Df(x(t))\\
&+x^T(t-\tau)B^T(S+\tau U)Ef(x(t-\tau))+x^T(t-\tau)B^T\\
&(S+\tau U)Ff(\nabla_q^{\alpha}x(t-\tau))+(\nabla_q^{\alpha}x(t-\tau))^TC^T\\
&(S+\tau U)Ax(t)+(\nabla_q^{\alpha}x(t-\tau))^TC^T(S+\tau U)\\
&Bx(t-\tau)+(\nabla_q^{\alpha}x(t-\tau))^TC^T(S+\tau U)C\nabla_q^{\alpha}x(t-\tau)\\
&+(\nabla_q^{\alpha}x(t-\tau))^TC^T(S+\tau U)Df(x(t))\\
&+(\nabla_q^{\alpha}x(t-\tau))^TC^T(S+\tau U)Ef(x(t-\tau))+(\nabla_q^{\alpha}x(t-\tau))^T\\
&C^T(S+\tau U)Ff(\nabla_q^{\alpha}x(t-\tau))+f^T(x(t))D^T(S+\tau U)\\
&Ax(t)+f^T(x(t))D^T(S+\tau U)Bx(t-\tau)\\
&+f^T(x(t))D^T(S+\tau U)C\nabla_q^{\alpha}x(t-\tau)+f^T(x(t))\\
&D^T(S+\tau U)Df(x(t))+f^T(x(t))D^T(S+\tau U)E\\
&f(x(t-\tau))+f^T(x(t))D^T(S+\tau U)Ff(\nabla_q^{\alpha}x(t-\tau))\\
&+f^T(x(t-\tau))E^T(S+\tau U)Ax(t)+f^T(x(t-\tau))\\
&E^T(S+\tau U)Bx(t-\tau)+f^T(x(t-\tau))E^T(S+\tau U)\\
&C\nabla_q^{\alpha}x(t-\tau)+f^T(x(t-\tau))E^T(S+\tau U)Df(x(t))\\
&+f^T(x(t-\tau))E^T(S+\tau U)Ef(x(t-\tau))\\
&+f^T(x(t-\tau))E^T(S+\tau U)Ff(\nabla_q^{\alpha}x(t-\tau))\\
&+f^T(\nabla_q^{\alpha}x(t-\tau))F^T(S+\tau U)Ax(t)+f^T(\nabla_q^{\alpha}x(t-\tau))\\
&F^T(S+\tau U)Bx(t-\tau)+f^T(\nabla_q^{\alpha}x(t-\tau))F^T(S+\tau U)\\
&C\nabla_q^{\alpha}x(t-\tau)+f^T(\nabla_q^{\alpha}x(t-\tau))F^T(S+\tau U)Df(x(t))\\
&+f^T(\nabla_q^{\alpha}x(t-\tau))F^T(S+\tau U)Ef(x(t-\tau))\\
&+f^T(\nabla_q^{\alpha}x(t-\tau))F^T(S+\tau U)Ff(\nabla_q^{\alpha}x(t-\tau))
\end{aligned} \qquad (19)
$$

Note that for any $\varepsilon_1,\varepsilon_2,\varepsilon_3\geq 0,$ it follows from (2) and (3) that

$$\varepsilon_1[\eta_1^2x^T(t)x(t)-f^T(x(t))f(x(t))]\geq 0,$$

$$\varepsilon_2[\eta_2^2x^T(t-\tau)x(t-\tau)-f^T(x(t-\tau))f(x(t-\tau))]\geq 0,$$

and

$$\varepsilon_3[\eta_3^2(\nabla_q^{\alpha}x(t-\tau))^T(\nabla_q^{\alpha}x(t-\tau))-f^T(\nabla_q^{\alpha}x(t-\tau))f(\nabla_q^{\alpha}x(t-\tau))]\geq 0.$$

Substituting (18) and (19) into (17), we have

$$\nabla_q V(x(t))\leq \varphi^{\mathrm{T}}\Delta\varphi, \qquad (20)$$

where the matrix Δ is defined with (13) and

$$\varphi=\begin{pmatrix}x(t) & x(t-\tau) & \nabla_q^{\alpha}x(t-\tau) & f(x(t)) & f(x(t-\tau)) & f(\nabla_q^{\alpha}x(t-\tau))\end{pmatrix}.$$

From (13) and (20), $\nabla_q V(t)<0.$ Since the conditions outlined in Theorem 2.2 are satisfied, the trivial solution of nonlinear q-fractional delay system (1) is asymptotically stable.

3. Numerical applications

Two numerical examples are presented below to illustrate the effectiveness of the obtained theoretical results.

Example 3.1 Let us define the below linear q-fractional neutral delay system as:

$$
\begin{aligned}
\nabla_q^{\alpha}x(t)&=\begin{pmatrix}-3.8 & -1.5\\ -1.8 & -2.4\end{pmatrix}x(t)+\begin{pmatrix}0.3 & -0.01\\ 0 & 0.2\end{pmatrix}x(t-\tau)\\
&+\begin{pmatrix}0.4 & 0\\ 0 & 0.3\end{pmatrix}\nabla_q^{\alpha}x(t-\tau),\quad t>0.
\end{aligned} \qquad (21)
$$

where $0<\alpha<1,\ 0<q<1,\ x(t)=\begin{pmatrix}x_1(t) & x_2(t)\end{pmatrix}^{\mathrm{T}},\ \tau=1.5.$

Now, we choose

$$P=\begin{pmatrix}28 & 1\\ 1 & 20\end{pmatrix},\ Q=\begin{pmatrix}8 & 1\\ 1 & 4\end{pmatrix},\ S=\begin{pmatrix}4 & 1\\ 1 & 3\end{pmatrix},\ U=\begin{pmatrix}1.2 & 0\\ 0 & 2\end{pmatrix}.$$

Under the above assumptions, by making a straightforward calculation with the help of MATLAB software, we can show that:

$$\Pi=\begin{bmatrix}-91.5280 & -12.4000 & 1.2480 & -2.7616 & 1.6640 & -4.0800\\ -12.4000 & -40.1900 & -3.0300 & 0.9210 & -4.0400 & 1.2300\\ 1.2480 & -3.0300 & -7.4780 & -0.9574 & 0.6960 & 0.0900\\ -2.7616 & 0.9210 & -0.9574 & -3.7634 & 0.0568 & 0.3570\\ 1.6640 & -4.0400 & 0.6960 & 0.0568 & -3.0720 & -0.8800\\ -4.0800 & 1.2300 & 0.0900 & 0.3570 & -0.8800 & -2.4600\end{bmatrix}.$$

In this case, $\Pi<0$, since all eigenvalues of matrix Π are -94.5910, -38.3651, -7.6909, -3.5436, -3.3680, and -0.9328, respectively. Thus, all the conditions of Theorem 2.1 are fulfilled. From Theorem 2.1, the trivial solution of the system (21) is asymptotically stable.

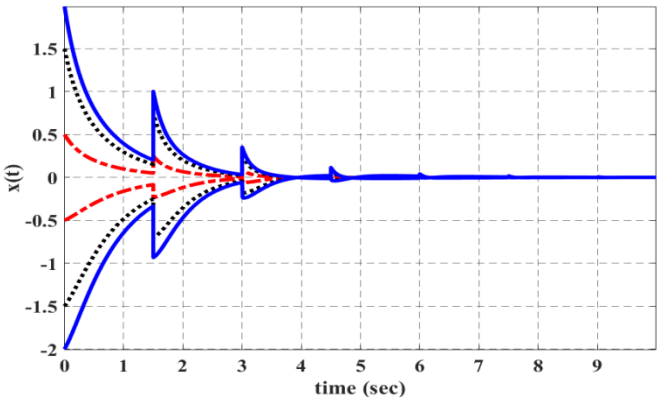

Figure 1. *The simulation of the Example 3.1 for* $\tau=1.5$.

Example 3.2 Let us define the below delayed nonlinear q-fractional system as:

$$\begin{aligned}\nabla_q^{\alpha}x(t)&=\begin{pmatrix}-4.8 & -1.2\\ -1.8 & -3.2\end{pmatrix}x(t)+\begin{pmatrix}0.3 & -0.02\\ 0 & 0.2\end{pmatrix}x(t-\tau)\\&+\begin{pmatrix}0.5 & 0\\ 0 & 0.2\end{pmatrix}\nabla_q^{\alpha}x(t-\tau)+\begin{pmatrix}1 & -0.1\\ 0 & -2\end{pmatrix}f(x(t))\\&+\begin{pmatrix}0.3 & -0.04\\ 0 & 0.2\end{pmatrix}f(x(t-\tau))+\begin{pmatrix}0.3 & 0\\ -0.1 & 0.2\end{pmatrix}f(\nabla_q^{\alpha}x(t-\tau)).\end{aligned}\tag{22}$$

where $0<\alpha<1,\ 0<q<1,\ x(t)=(x_1(t)\quad x_2(t))^T, \tau=1.5$.

Now, we choose $\varepsilon_1=42, \varepsilon_2=16, \varepsilon_3=20, \eta_1=0.02, \eta_2=0.03, \eta_3=0.04,$

$$P=\begin{pmatrix}24 & 2\\ 2 & 20\end{pmatrix}, Q=\begin{pmatrix}10 & 1\\ 1 & 4\end{pmatrix}, S=\begin{pmatrix}4 & 1\\ 1 & 3\end{pmatrix},$$
$$U=\begin{pmatrix}1.2 & 0\\ 0 & 0.8\end{pmatrix}, W=\begin{pmatrix}4 & 0\\ 0 & 1\end{pmatrix}.$$

Under the above assumptions, by making a straightforward calculation with the help of MATLAB software, we can show that:

$$\Delta = \begin{bmatrix} -63.0632 & -4.6800 & -1.6920 & -1.9592 & -2.8200 & -2.0720 & -5.6400 & 21.2840 & -1.6920 & -1.8464 & -0.6560 & -2.0720 \\ -4.6800 & -69.7432 & -2.4480 & 1.2352 & -4.0800 & 1.0720 & -8.1600 & -9.9040 & -2.4480 & 1.3984 & -2.9840 & 1.0720 \\ -1.6920 & -2.4480 & -9.4636 & -0.9748 & 0.8700 & 0.0600 & 1.7400 & -0.7740 & 0.5220 & -0.0096 & 0.4920 & 0.0600 \\ -1.9592 & 1.2352 & -0.9748 & -3.8233 & 0.0420 & 0.1640 & 0.0840 & -1.6484 & 0.0252 & 0.1606 & -0.0568 & 0.1640 \\ -2.8200 & -4.0800 & 0.8700 & 0.0420 & -2.5180 & -0.9000 & 2.9000 & -1.2900 & 0.8700 & -0.0160 & 0.8200 & 0.1000 \\ -2.0720 & 1.0720 & 0.0600 & 0.1640 & -0.9000 & -2.8000 & 0.2000 & -1.7000 & 0.0600 & 0.1600 & -0.0240 & 0.1680 \\ -5.6400 & -8.1600 & 1.7400 & 0.0840 & 2.9000 & 0.2000 & -32.2000 & -2.5800 & 1.7400 & -0.0320 & 1.6400 & 0.2000 \\ 21.2840 & -9.9040 & -0.7740 & -1.6484 & -1.2900 & -1.7000 & -2.5800 & -23.7420 & -0.7740 & -1.5968 & 0.0760 & -1.7000 \\ -1.6920 & -2.4480 & 0.5220 & 0.0252 & 0.8700 & 0.0600 & 1.7400 & -0.7740 & -19.4780 & -0.0096 & 0.5220 & 0.0252 \\ -1.8464 & 1.3984 & -0.0096 & 0.1606 & -0.0160 & 0.1600 & -0.0320 & -1.5968 & -0.0096 & -16.8387 & -0.0096 & 0.1606 \\ -0.6560 & -2.9840 & 0.4920 & -0.0568 & 0.8200 & -0.0240 & 1.6400 & 0.0760 & 0.4920 & -0.0896 & -19.4960 & -0.0240 \\ -2.0720 & 1.0720 & 0.0600 & 0.1640 & 0.1000 & 0.1680 & 0.2000 & -1.7000 & 0.0600 & 0.1600 & -0.0240 & -19.8320 \end{bmatrix}.$$

In this case, $\Delta < 0,$ since all eigenvalues of matrix Δ are -75.0337, -72.1298, -31.7295, -20.7979, -20.0050, -17.5758, -18.4755, -12.1922, -9.1788, -3.5531, -1.5474 and -0.7794, respectively. Thus, all conditions of Theorem 2.2 are fulfilled. From Theorem 2.2, the trivial solution of the system (22) is asymptotically stable.

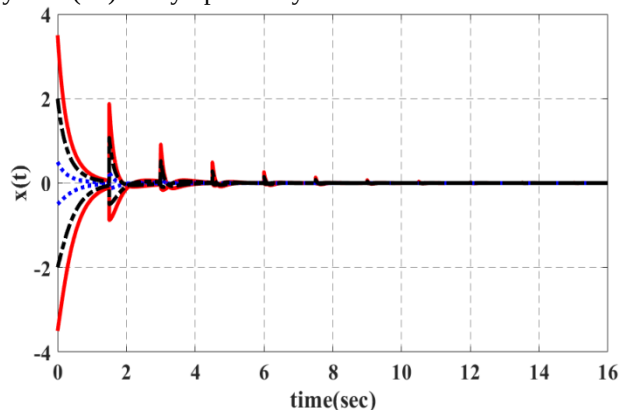

Figure 2. *The simulation of the Example* 3.2 *for* $\tau = 1.5$.

An examination of the theoretical solutions for the above examples (Examples 3.1 and 3.2) indicates that the trivial solution of the systems becomes stable after a certain time interval under different initial conditions. This stability is supported by the corresponding simulation results (Figures 1 and 2).

4. Conclusions

In this paper, we derive sufficient conditions for the asymptotic stability of certain kinds of *q*-fractional neutral type systems using LMIs and based on the direct computation of quantum derivatives of LKFs. Two examples are provided to highlight the validity of the proposed methods. In this study believe that the theoretical results obtained are both intriguing and contemporary, providing a significant contribution to the existing literature. Our future research will focus on the stability and synchronization of q-fractional systems with time-varying delays and q-fractional coupled complex networks.

References

[1]. Agarwal, R.P., "Certain fractional *q*-integrals and *q*-derivatives," Proc Cambridge Philos Soc., 66, (1969), pp. 365-370.

[2]. Agarwal, R.P., Benchohra, M., Hamani, S., "A survey on existence results for boundary value problems of nonlinear fractional differential equations and inclusions," Acta Appl. Math., 109 (3), (2010), pp. 973-1033.

[3]. Al-Salam, WA., "Some fractional *q*-integrals and *q*-derivatives," Proc Edin Math Soc., 15, (1969), pp. 135-140.

[4]. Altun, Y. and Tunç, C., "On exponential stability of solutions of nonlinear neutral differential systems with discrete and distributed variable lags," Nonlinear Studies 26(2), (2019), pp. 455-466.

[5]. Annaby, M.H. and Mansour, Z.S., "Q-fractional Calculus and Equations," New York: Springer-Heidelberg; 2012.

[6]. Balasubramaniam, P., Krishnasamy, R. and Rakkiyappan, R., "Delay-dependent stability of neutral systems with time-varying delays using delay-decomposition approach," Applied Mathematical Modelling 36, (2012), pp. 2253–2261.

[7]. Bohner, M. and Peterson, A., "Dynamic Equations on Time Scales: An Introduction with Applications," Boston: Birkhäuser, 2001.

[8]. Chartbupapan, C., Bagdasar, O. and Mukdasai, K., "A Novel Delay-Dependent Asymptotic Stability Conditions for Differential and Riemann-Liouville Fractional Differential Neutral Systems with Constant Delays and Nonlinear Perturbation," Mathematics, 8, (2020), pp. 1-10.

[9]. Duarte-Mermoud, M.A., Aguila-Camacho, N., Gallegos, J.A. and Castro-Linares, R., "Using general quadratic Lyapunov functions to prove Lyapunov uniform stability for fractional order systems," Commun. Nonlinear Sci. Numer. Simul., **22**, (2015), pp. 650–659.

[10]. Diethelm, K., "The analysis of fractional differential equations: An application-oriented exposition using differential operators of Caputo type," Berlin: Springer, 2010.

[11]. Jarad, F., Abdeljawad, T. and Baleanu D., "Stability of *q*-fractional non-autonomous systems," Nonlinear Anal RealWorld Appl., 14, (2013b), pp. 780-784.

[12]. Kac, V. and Cheung, P., "Quantum calculus," New York: Springer-Verlag, 2002.

[13]. Kilbas, A. A., Srivastava, H. M. and Trujillo, J. J., "Theory and Application of Fractional Differential Equations," Elsevier, New York: USA, 2006.

[14]. Koca, I. and Demirci, E., "On local asymptotic stability of q-fractional nonlinear dynamical systems," Applications and Applied Mathematics: An International Journal (AAM), 11, (2016), pp. 174-183.

[15]. Li, H. Zhou, S. and Li, H., "Asymptotic stability analysis of fractional-order neutral systems with time delay," Adv. Difference Equ., 2015, (2015), pp. 325–335.

[16]. Liu, K. and Jiang, W., "Stability of fractional neutral systems," Adv. Differ. Equ., 2014(78), (2014), pp. 1-9

[17]. Liu P.L., "A delay decomposition approach to stability analysis of neutral systems with time-varying delay," App Math Model., 37, (2013), pp. 5013-5026.

[18]. Liu, S., Jiang, W., Li, X. and Zhou, X.F., "Lyapunov stability analysis of fractional nonlinear systems," Appl. Math. Lett., 51, (2016), pp. 13–19.

[19]. Liu, S., Wu, X. Zhang, Y.J. and Yang, R., "Asymptotical stability of Riemann–Liouville fractional neutral systems," Appl. Math. Lett., 69, (2017), pp. 168–173.

[20]. Liu, S., Wu, X., Zhou, X.F. and Jiang, W., "Asymptotical stability of Riemann–Liouville fractional nonlinear systems," Nonlinear Dynam., 86(1), (2016), pp. 65–71.

[21]. Liu, S., Zhou, X.F., Li, X. and Jiang, W., "Stability of fractional nonlinear singular systems its applications in synchronization of complex dynamical networks," Nonlinear Dynam., 84(4), (2016), pp. 2377–2385.

[22]. Liu, S., Zhou, X.F., Li, X. and Jiang, W., "Asymptotical stability of Riemann–Liouville fractional singular systems with multiple time-varying delays," Appl. Math. Lett., 65, (2017), pp. 32–39.

[23]. Lu, J.G. and Chen, G., "Robust stability and stabilization of fractional-order interval systems: An LMI approach," IEEE Trans. Automat. Control, 54 (6), (2009), pp. 1294–1299.

[24]. Lu, Y.F., Wu, R.C. and Qin, Z.Q., "Asymptotic stability of nonlinear fractional neutral singular systems," J. Appl. Math. Comput., 45, (2014), pp. 351–364.

[25]. Magin, R., "Fractional calculus models of complex dynamics in biological tissues," Comput. Math. Appl., 59, (2010), pp. 1586-1593.

[26]. Mahdi, N.K. and Khudair, A.R., "Stability of nonlinear q-fractional dynamical systems on time scale," Partial Differ. Equ. Appl. Math., 7, (2023), 100496.

[27]. Metzler, R. and Klafter, J., "The random walk's guide to anomalous diffusion: a fractional Dynamics approach," Phys. Rep., 339, (2000), pp. 1-77.

[28]. Podlubny, I., Fractional Differential Equations, Academic Press., New York: USA, 1999.

[29]. Rostek, S. and Schobel, R., "A note on the use of fractional Brownian motion for financial modeling," Econ Model., 30, (2013), pp. 30-35.

[30]. Sabatier, J., Moze, M. and Farges, C., "LMI stability conditions for fractional order systems," Comput. Math. Appl., 59 (5), (2010), pp. 1594-1609.

[31]. Singh, A., Shukla, A., Vijayakumar, V. and Udhayakumar, R., "Asymptotic stability of fractional order (1, 2] stochastic delay differential equations in Banach spaces," Chaos, Solitons & Fractals, 150, (2021), pp. 1-9.

[32]. Sivasankar, S. and Udhayakumar, R., "Hilfer fractional neutral stochastic Volterra integro-differential inclusions via almost sectorial operators," Mathematics, 10(12), (2022), pp. 1-19.

[33]. Xu, S. and Lam, J., "Robust control and filtering of singular systems," Lecture Notes in Control and Information Sciences, 29 332, Springer-Verlag, Berlin, 2006.

[34]. Varun Bose, C. B. S. and Udhayakumar, R., "Existence of mild solutions for Hilfer fractional neutral integro differential inclusions via almost sectorial operators," Fractal and Fractional, 6(9), (2022), pp. 1-16.

[35]. Yang, W., Alsaedi, A., Hayat, T. and Fardoun, H.M., "Asymptotical stability analysis of Riemann-Liouville q-fractional neutral systems with mixed delays," Math. Meth. Appl. Sci., 42, (2019), pp. 4876–4888.

[36]. Yang, C., Zhang, Q. and Zhou, L., "Stability analysis and design for nonlinear singular systems," Lecture Notes in Control 31 and Information Sciences, 435, Springer, Heidelberg, 2013.

[37]. Zhang, H., Ye, R., Cao, J., Ahmed, A., Li, X. and Ying, W., "Lyapunov functional approach to stability analysis of Riemann–Liouville fractional neural networks with time-varying delays," Asian J. Control, 20(5), (2018), pp. 1938–1951.

MANAS Journal of Engineering
ISSN 1694-7398 | e-ISSN 1694-7398

Volume 13, Issue 1, (2025) Pages 40-51
https://doi.org/10.51354/mjen.1584061

An atmospheric impact assessment of water-based hydrogen production methods: Sustainability evaluation

Aysegul Yagmur Goren

Izmir Institute of Technology, Department of Environmental Engineering, Izmir, Türkiye, yagmurgoren@iyte.edu.tr, ORCID: 0000-0003-1114-6059

ABSTRACT

Population growth and urbanization have significantly affected the energy demand and environmental contaminant levels worldwide. Currently, global warming with greenhouse gas emissions, air pollution, acid rain, environmental degradation, and depletion of energy resources are all consequences of utilizing fossil fuel-powered energy infrastructure. Hence, renewable energy-powered alternative energy resources must be considered to minimize atmospheric emissions and environmental contaminants. Hydrogen (H_2) has become a viable fuel to satisfy energy needs, and in recent years, there has been a lot of interest in green H_2 production, particularly using electrolysis processes that produce no emissions. In this regard, this paper utilized the atmospheric emission assessment software to evaluate atmospheric contaminants from the alkaline electrolysis (AE), proton exchange membrane-based electrolysis (PEM), and solid oxide electrolysis (SOE) processes. Among these processes, the highest CO_2 emission comes from the PEM electrolysis process, accounting for 4.68 kg-CO_2/kg-H_2, while the AE process provides the minimum total CO_2 emissions of 3.28 kg-CO_2/kg-H_2. A similar trend was observed in the particulate matter (PM) emissions, and the $PM_{2.5}$ emissions were 1.36, 1.30, and 1.24 kg-$PM_{2.5}$/kg-H_2 for PEM, SOE, and AE processes, respectively. Moreover, the environmental impact parameters of the processes were assessed, and the lowest global warming potential (GWP) of 3.32 kgCO_2-eq./kg-H_2 was obtained for the AE process. Accordingly, these results demonstrated that energy production techniques may be completely environmentally sustainable by substituting fully sustainable resources for the energy sources employed in current H_2 production methods.

ARTICLE INFO

Research article

Received: 13/11/2024
Accepted: 26/02/2025

Keywords:
Atmospheric contaminants, electrolysis, hydrogen production, sustainability, environmental assessment

1. Introduction

The global warming tragedy and its consequences have gained worldwide interest. Therefore, since fossil fuels are one of the main reasons for global warming, a greener energy source should replace traditional fossil fuels to attain carbon neutrality. In this regard, hydrogen (H_2) becomes a possible alternative since it burns without producing carbon dioxide (CO_2) and has extremely high efficiency. Moreover, H_2 production for energy storage via water electrolysis, biomass electrolysis, or other renewable energy source use has shown to be beneficial in several ways, including reducing toxic gas byproducts like CO_x, sulphur oxide (SO_x), and nitrogen oxide (NO_x), which are not good for the environment. In addition, H_2 has a heating value three times larger than any other fossil fuel, making it the ideal option for long-term and extensive use in the transition to green energy [1].

Nevertheless, electrolysis operations account for less than 4% of H_2 production, with H_2 serving as the primary by-product of chlorine synthesis. Therefore, most H_2 requirements depend on the fossil pathway via natural gas steam reforming [2]. Due to high electricity costs and conflicting rules, the production costs of electrolysis procedures are greater than those of conventional fossil sources, which is precisely what is causing this current situation [3].

In the coming decades, there has to be a significant rise in the percentage of H_2 produced from renewable power sources to lower CO_2 emissions and achieve energy independence from fossil fuels. Water electrolysis is, therefore, a crucial technique for utilizing renewable energy to divide water into H_2 and oxygen. Combining water electrolysis with renewable energy sources is especially beneficial because extra electrical energy may be chemically stored as H_2 to close the gap between energy output and demand. Fundamentally, three methods are available for water electrolysis: solid oxide

electrolysis (SOE), proton exchange membrane electrolysis (PEM), and alkaline water electrolysis (AE) [4]. Among these processes, high-temperature SOE technology is still in development, while low-temperature technologies, such as AE and PEM, provide high levels of technological readiness [5]. To date, several experimental studies have been performed on various electrolysis processes to improve their H_2 production performances and reduce environmental impacts [6,7]. Moreover, several theoretical environmental impact assessment studies have been conducted on electrolysis processes. For instance, Jolaoso et al. [8] performed a life cycle analysis of an SOE process for H_2, considering different wastewater and energy resources. They reported that the CO_2 emissions from the SOE process are 6.89 kg-CO_2eq./kg-H_2, and their results also proved that solar photovoltaic (PV) is a good energy source for SOE operations. In a separate study, the environmental impacts of the AE, PEM, and SOE processes are compared, and the life-cycle greenhouse gas (GHG) emissions of all electrolyzer technologies using low-carbon energy (biomass, solar, nuclear or wind) range from 0.3 to 2.4 kg-CO_2eq./kg-H_2 [9]. Kim et al. [10] investigated the greenhouse gas (GHG) emissions, particularly carbon dioxide emissions, from AE and PEM electrolysis processes, considering various renewable energy sources like solar, wind, and hydropower. Their results revealed that the carbon dioxide emissions for AE and PEM electrolysis processes were 8434 and 3695 kg-CO_2/kg-H_2, respectively, providing that an AE system emits about 2.3 times more greenhouse gasses than a PEM system. One potential reason for this significant difference may lie in excluding emissions associated with the membrane production stage in the assessment. Membrane production involves energy-intensive manufacturing processes and the utilization of specialized materials, both of which contribute to additional carbon emissions. By not accounting for these emissions, the environmental impact of the PEM system might appear underestimated in comparison to the AE system. Including these factors in the analysis could reveal a more comprehensive picture of the total greenhouse gas emissions, potentially reducing the observed gap between the two systems. Moreover, their study focused exclusively on carbon dioxide emissions, without considering other GHG emissions or environmental impacts that may also contribute to the overall footprint of the electrolysis processes. Zhang et al. [11] performed the life cycle assessment of onshore-offshore wind-powered H_2 production through water electrolysis, and it is clear from the study of the environmental impact proportion that the process of building infrastructure has a major influence on the total environmental effect. Wei et al. [12] also investigated the environmental impacts of four electrolyzer technologies SOE, PEM, anion-exchange membrane (AEM), and AE. The authors reported that significant CO_2 reductions are feasible with SOE and AEM electrolyzers, both of which are still in the development stage, whereas PEM and AE, being mature technologies, provide few possibilities for improvement.

Previous studies have primarily focused on process optimization and the evaluation of environmental impact parameters without providing a detailed analysis of the atmospheric pollutants influencing these parameters, both in type and magnitude. Moreover, they have predominantly focused on the operational phase of processes, overlooking the broader lifecycle impacts. This narrow scope has proven insufficient for generating realistic and comprehensive results. Since most of the literature studies only focused on the direct environmental impact parameters of these electrolysis processes. There is a critical need to evaluate the individual atmospheric emissions from electrolysis processes to understand the main contaminant types. Consequently, the novelty of our research lies in addressing this gap by incorporating emissions from all lifecycle stages, including material production, transportation, and operational phases. By identifying and quantifying the emissions that influence environmental parameters in detail, our study provides a more holistic and accurate environmental assessment. This comprehensive approach offers meaningful insights and practical relevance, making it better suited for real-world applications compared to prior research. Another novelty of this work also lies in its ability to address critical limitations of traditional approaches by offering significant advancements in cost-efficiency, reliability, and performance. By utilizing sustainable and readily available materials, the proposed system substantially reduces overall costs, making it a more economically viable solution. Furthermore, the design ensures enhanced reliability by integrating robust operational features that maintain efficiency under varying conditions. The optimization of key performance parameters further contributes to its superior functionality, ensuring consistent and high-quality outcomes. These advancements collectively position this work as a practical and scalable solution for real-world applications, bridging the gap between theoretical potential and operational feasibility.

In this context, the key purpose of this study is to evaluate the atmospheric emissions of different electrolysis-based H_2 production processes (alkaline, solid oxide, and proton exchange membrane-based electrolysis processes) using greenhouse gases, regulated emissions, and energy use in transportation (GREET) model, considering the feedstock utilization and extraction, energy production, transportation, and H_2 production stages. Overall, the critical goals of this paper are: (i) to review and discuss the benefits, limitations, and future perspectives of specified electrolysis processes for H_2 production, (ii) to assess and compare the environmental impacts and atmospheric emissions of the processes presenting their atmospheric contaminants for whole process chain, including feedstock utilization, transportation, and H_2 production stages, and (iii) to compare electrolysis processes to provide the best option in sustainability manner, considering their sustainability levels. Consequently, this study assesses the atmospheric emissions and environmental effects of electrolysis technologies for effective and

sustainable H_2 production. Overall, this study proved easy to identify which steps in the electrolysis processes have the greatest environmental impacts and what kind of measures should be taken at which steps to prevent the potential emissions by measuring the atmospheric emission of the processes from feedstock processing to H_2 production.

2. System description and analysis

In this section, a description of the alkaline, solid oxide, and proton exchange membrane-based water electrolysis systems with boundaries for H_2 production are reported, and their environmental impacts are assessed, considering atmospheric emissions from these processes (Figure 1). A GREET study usually includes the following procedures: defining the objectives and scope, reviewing the inventory, assessing the environmental effect, and interpreting the results [13]. Furthermore, the total emissions from every stage are standardized to the preferred functional unit, which is established by the kg of H_2 produced for different H_2 production pathways. For the suggested system, the emissions of CO_2, CO, greenhouse gas emissions (GHG-100), particulate matter ($PM_{2.5}$ and PM_{10}), NO_x, volatile organic compounds (VOCs), etc., were calculated and addressed separately.

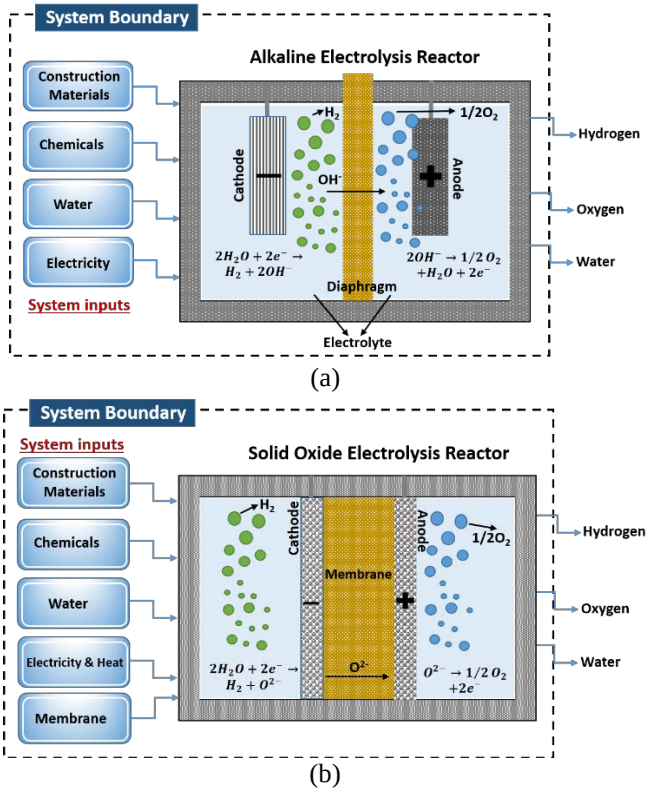

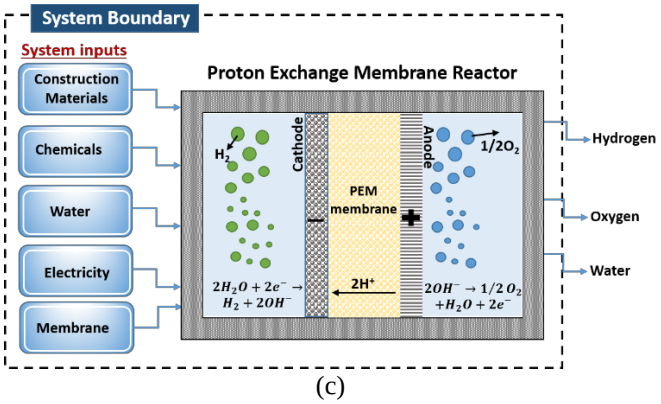

Figure 1. *System boundaries and processes of investigated water electrolysis systems: (a) alkaline electrolysis, (b) solid oxide electrolysis, and (c) proton exchange membrane electrolysis.*

The GREET software, developed by Argonne National Laboratory, is a comprehensive and freely accessible life-cycle analysis tool widely used for assessing the energy consumption and atmospheric emissions of various technologies, including electrolysis processes such as alkaline, solid oxide, and proton exchange membrane systems. GREET models the entire life cycle of hydrogen production, from resource extraction to the end-use phase, enabling the quantification of GHG emissions, regulated air pollutants, and energy consumption. For electrolysis systems, the software requires inputs such as the type of system (alkaline, solid oxide, or PEM), energy source, and regional electricity grid mix (e.g., renewable, fossil-based, or nuclear), operating conditions like temperature and pressure, and material requirements for components like electrodes and electrolytes. Outputs generated by GREET include GHG emissions (e.g., CO_2, CH_4, N_2O), criteria air pollutants (e.g., NO_x, SO_x, $PM_{2.5}$, and PM_{10}), and energy consumption across the life cycle stages. Input values in Table 1 were entered into the model based on data from experimental studies on the processes examined, and emissions were calculated accordingly.

Table 1. *Typical specification of studied electrolyzers for 1 kg H_2 production*.

Specification	AE	PEM	SOE
Cell temperature	60 °C	50 °C	900 °C
Current density	0.4 A/cm^2	2 A/cm^2	1 A/cm^2
Voltage	2.4 V	2.2. V	1 V
Cell area	4 m^2	4 m^2	4 m^2
System life time	20 year	20 year	20 year
Hydrogen purity	99.9 %	99.9 %	99.9 %
Stack life time	90000 h	20000 h	30000 h

The software employs detailed formulations and mathematical models to evaluate emissions and energy use. These include energy balance equations to calculate electricity and heat requirements, material flow analysis to estimate emissions from raw material production and system operation, and electrochemical models to incorporate cell efficiency,

hydrogen yield, and system degradation. For alkaline electrolysis, GREET accounts for emissions related to producing KOH electrolytes, steel electrodes, and operational energy use. For PEM electrolysis, it models the impacts of platinum group metals in the catalyst and the ion-conducting membrane. Similarly, solid oxide electrolysis inputs include high-temperature energy demands and ceramic material production. GREET assesses emissions by simulating the entire life cycle of each electrolysis system, identifying emission hotspots, and quantifying direct emissions, such as those from electricity generation, and indirect emissions from upstream activities like material production and transportation. It also allows scenario analysis, enabling emissions comparisons under different energy grid configurations (e.g., renewable vs. coal-based electricity) or optimization strategies, such as using waste heat or renewable electricity. In this study, a renewable-based energy grid is considered for all electrolysis processes. Overall, by integrating material and energy flows with life-cycle inventory data, GREET provides a robust framework for quantifying and comparing the environmental impacts of alkaline, solid oxide, and PEM electrolysis systems, offering actionable insights to advance sustainable hydrogen production. Consequently, all atmospheric emission analyses were conducted using the GREET software database, with inputs derived from the dataset of the project. This dataset was specifically developed to reflect the unique characteristics and parameters of the system under investigation, ensuring that the analyses accurately represent the study's context. By integrating this customized dataset into the GREET software, the evaluation of life-cycle emissions and energy use was carried out with precision and alignment to the objectives of the study. As a result, this section does not include additional analyses beyond those facilitated by the GREET database and the tailored dataset of the project.

2.1 Alkaline electrolysis

In particular, the AE is a scalable, adaptable, and widely utilized method for producing pure H_2 [14]. Fundamentally, an alkaline electrolyzer splits water into H_2 and HO^- at the cathode. The latter moves through the diaphragm and electrolyte before discharging at the anode and releasing the O_2. Low temperatures (60-80 °C) are used for AE, and the electrolyte used in the process is an aqueous solution of potassium hydroxide (KOH), sodium hydroxide (NaOH), or sodium chloride (NaCl), with a concentration of around 25–30% and applied voltage of 1.8 to 2.2 V. In contrast to traditional AEs, advanced AEs perform at a comparatively low voltage of 1.6 V and a current density of 2 A/cm^2. Moreover, AE produces H_2 at a purity of 99.9%, meeting fuel cell requirements for high-quality H_2 production [15]. Overall, although AE is an outdated technology, it remains one of the most straightforward and appropriate ways of producing H_2. However, AE has challenges related to energy consumption, durability, safety, and installation and maintenance costs [16]. Nevertheless, AE is a well-established method; industrial electrolyzers are available, and it is an environmentally friendly method of producing H_2 if the power is produced using CO_2-free methods like nuclear and renewable resources. For instance, together with innovative electrode technologies, the chlor-alkali electrolyzer's developed zero-gap technology offers improved performance [17].

2.2. Solid oxide electrolysis

Steam electrolysis utilizing an SOE is one method of water electrolysis currently being developed. Its high working temperatures of 600-1000 °C significantly reduce electrical energy usage [18]. Compared to other electrolysis processes, SOE technology with intermediate temperature has an electrical energy usage of around 3 kWh/Nm^3 of H_2. A SOE comprises a positive O_2 electrode, a negative fuel electrode, and an electron-insulating electrolyte with high ionic conductivity at high temperatures [19]. Namely, a subsequent rise in operating temperature results in a significant increase in thermal energy demand and a decrease in electrical energy demand in the SOE process, and the operating temperature does not affect the total energy requirement. High-temperature SOE is, therefore, beneficial as it offers more chances to use industrial waste heat to produce H_2. In SOE operation, high-temperature steam is supplied to the cathode side, where the catalyst site converts it to H_2 and O_2 gases. The phase potential then moves the O_2 ions across the electrolyte to the anode side, undergoing oxidation to produce O_2 molecules [20]. Nevertheless, in the SOE process, detailed phenomena often involve a complex interplay of material qualities, operating factors, reaction kinetics, and thermodynamics. Since SOE is still an emerging technology, modeling may be very important for both the design and management of SOEs. Overall, SOE and stacks operate at substantially higher temperatures, which accelerates reaction kinetics and may lead to improved electrical efficiency. Thermodynamically stated, waste heat from industrial operations or high-temperature heat from solar thermal power can supply a portion of the energy required for the endothermic water-splitting reaction, lowering the need for electric energy. Moreover, CO_2 and water molecules can be divided via high-temperature electrolysis, or a combination, to create synthesis gas or other energy carriers like methanol or methane through catalytic conversion.

2.3. Proton exchange membrane electrolysis

General Electric created the first water electrolyzer based on a solid polymer electrolyte concept in developing water electrolysis technology for effective H_2 production [21]. This novel technique was originally called a PEM or polymer electrolyte membrane. The PEM electrolyzer and the alkaline electrolyzer have a similar construction. The key difference is forming a zero-pole separation by employing a thin film-electrode assembly called a membrane electrode, and the Nafion-type membrane separator becomes very acidic after soaking in water. The anode and cathode catalysts are hot-pressed or electroless-plated onto both sides of the separator.

In the PEM electrolyzer, at 10000 to 20,000 A/m^2, the DC density is approximately 5 times higher than that of the AE process [22]. Moreover, the PEM electrolyzer can function at varying pressures because of its operating temperature range of 50 to 80 °C, pressure of less than 5 MPa, and lower volume than the AE. Fundamentally, in the PEM electrolyzer, the deionized water just needs to reach the anode side of the electrolyzer, in contrast to the alkaline electrolyzer. Following energization, the membrane electrode's anode side produces H_2 and O_2 ions, while the cathode side receives the H_2 ions in their hydrated form, which produces H_2 gas. Then, the O_2 and H_2 are separated by the membrane. The Nafion membrane separation and lack of solution voltage drop give this approach a high energy efficiency for producing H_2. In addition, compared to the AE process, PEM offers several benefits, including excellent safety, ease of handling and maintenance, low gas crossover, high proton conductivity, low power consumption, high purity of H_2, large size and mass, high-pressure operation, and control over electrical power variations.

3. Results and discussion

In this section, the atmospheric emissions and other environmental impact parameters from the three different water-based H_2 production methods (alkaline, solid oxide, and proton exchange-based electrolysis) are evaluated and discussed comprehensively. Furthermore, the normalized ranking method presents their sustainability potential based on impact parameters.

The evaluation of atmospheric emissions and environmental impact parameters for the three water-based hydrogen production methods (alkaline electrolysis, solid oxide electrolysis, and proton exchange membrane electrolysis) was conducted using distinct methodologies. Atmospheric emissions were calculated and compared using the GREET software, which provides a comprehensive life-cycle analysis framework. Environmental impact assessment, on the other hand, was performed by utilizing the coefficients of impact categories listed in Table 1. These coefficients facilitated a detailed quantification of environmental problems across various categories, enabling a comparative analysis of the three methods.

3.1. Atmospheric emissions

3.1.1. Carbon dioxide emission

The enormous increase in the concentration of anthropogenic CO_2 in the atmosphere from the mid-1800s is widely attributed to the increased usage of fossil fuels since the beginning of the Industrial Revolution [23]. Therefore, considering SDGs, there is a significant need to explore green energy resource alternatives and make our current energy systems more sustainable to overcome huge amounts of CO_2 emissions. In this context, the H_2 is one of the more favorable options for present-day and future energy carriers. Namely, commercialized gasification, steam reforming, and pyrolysis techniques are currently used to produce H_2 from fossil fuel resources, accounting for most H_2 production worldwide [4]. Nevertheless, a big disadvantage of fossil fuel-based H_2 production technologies is the large quantities of CO_2 emissions since they utilize fossil fuels in both heat source and manufacturing steps. Recently, to overcome these problems most of these systems combined with the different CO_2-capture processes. Moreover, the water-based electrolysis processes have significant advantages owing to their low CO_2 emissions. Overall, it is important to consider the total chain of activities from resource utilization to H_2 production to evaluate if using different resources and/or processes instead of the currently available options will decrease or increase GHG emissions. In this regard, the CO_2 and GHG emissions from different electrolysis processes are evaluated in this study (Figure 2).

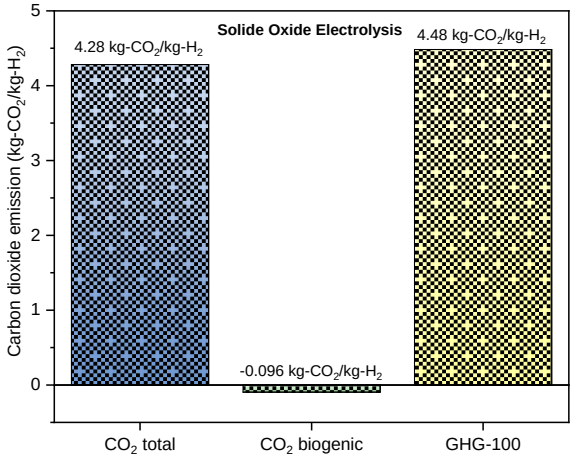

(a)

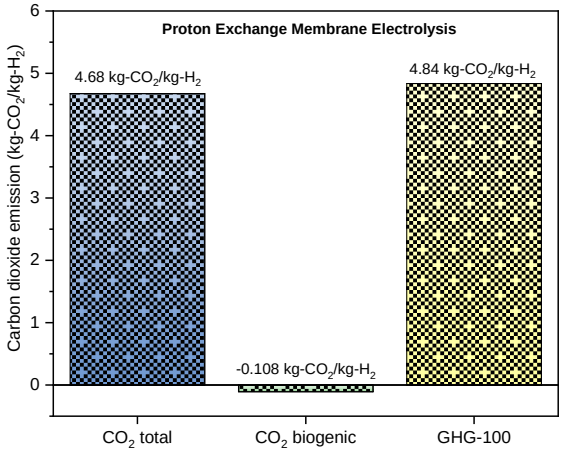

(b)

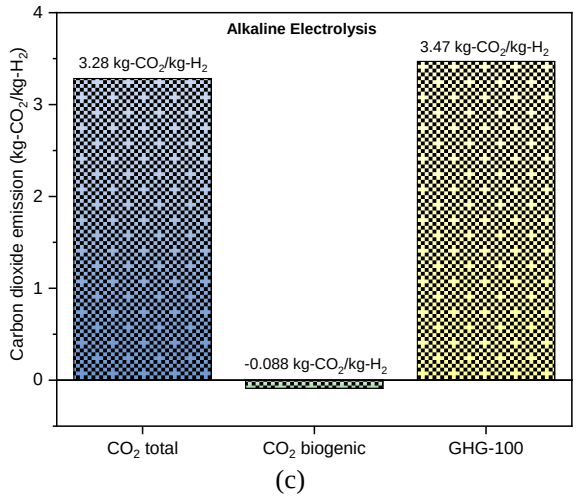

Figure 2. *The CO_2 emissions from (a) solid oxide, (b) proton exchange membrane, and (c) alkaline electrolysis processes.*

The emissions from the transportation, feedstock use, and H_2 production phases contribute to the overall CO_2 emission values of the processes. For the SOE process, the CO_2 emission was 4.28 kg-CO_2/kg-H_2 with a GHG emission value of 4.48 kg-CO_2/kg-H_2 (Figure 2a). Namely, the CO_2 emissions associated with SOEs depend on several factors, primarily the source of electricity and heat. If renewable energy sources, such as wind or solar, are used to power the process, direct CO_2 emissions can be near zero. However, if fossil fuels provide electricity, emissions can rise significantly, with estimates suggesting that around 0.5 to 1 kg of CO_2 could be released per kg of H_2 produced. Additionally, high-temperature heat is often required, and if generated from natural gas or coal, this could add another 1 to 2 kg of CO_2 per kg of H_2, depending on the fuel efficiency. Another source of CO_2 emissions arises from the production and disposal of SOE components, such as ceramic electrolytes and metal interconnects, which may contribute between 5 and 10% of the overall carbon footprint, depending on material choice and manufacturing processes. Our findings agree with the literature studies, considering these possible sources of CO_2 emissions from electrolytes and materials production processes for the electrolysis processes. Therefore, these results revealed that achieving low-emission SOE operation requires integrating renewable electricity, efficient heat recovery, and sustainable materials, with each factor playing a crucial role in reducing overall emissions. For example, the CO_2 emission from the wind-powered electrolysis process was reported as 0.95 kg-CO_2/kg-H_2; however, the author neglected to account for the emissions from the transportation and extraction of materials [24].

Moreover, the CO_2 and GHG emissions from the PEM electrolysis process are evaluated, and the CO_2 and GHG emissions are 4.68 kg-CO_2/kg-H_2 and 4.84 kg-CO_2/kg-H_2, respectively. The results reveal that the membrane production procedure contributes the highest CO_2 emissions in the PEM process, considering the material extraction and chemical utilization steps. Therefore, selecting green and sustainable materials with low environmental emissions for membrane production can effectively decrease the CO_2 emission of the overall system. Similarly, Zhang et al. [25] evaluated the environmental impacts of the PEM process for solar energy-powered H_2 production, considering various lifetimes. The lowest CO_2 emission was found to be 4.63 kg-CO_2/kg-H_2 for a lifetime of 60 years, while it was 9.67 kg-CO2/kg-H_2 for a lifetime of 30 years. Overall, their results provided that the lifetime of the system is another important parameter to understand and minimize its environmental impacts. As estimated, the lowest total CO_2 emission of 3.28 kg-CO_2/kg-H_2 is obtained for the AE process, while its GHG emission was 3.47 kg-CO_2.eq./kg-H_2 (Figure 2c). For the AE process, the operational phase consumes primarily electricity and water which are the main two inputs of the life cycle of H_2 production, therefore, the electricity production step is the main contributor to the CO_2 emissions in the AE process. Overall, compared to the three electrolysis processes, the highest CO_2 emissions were obtained for the PEM process due to its complex membrane production procedure.

Furthermore, the biogenic CO_2 emissions of the electrolysis technologies are evaluated and presented in Figure 2. Fundamentally, the term "biogenic CO_2 emissions" mostly refers to CO_2 that comes from biological sources including plants, animals, and microbes, and is a component of the natural carbon cycle. Biogenic CO_2 is a component of very short-term carbon cycles, in contrast to fossil CO_2, which is produced by burning fossil fuels. Additionally, biogenic CO_2 emissions may be negative; in this case, the process sequesters more CO_2 than it releases. For example, because plants grow and store carbon in biomass and soils, some agricultural methods and reforestation may absorb CO_2 emissions from the atmosphere. As a result, the idea of biogenic CO_2 emission is crucial for carbon accounting and environmental impact analyses, particularly in fields like bioenergy, forestry, and agriculture. Namely, the formation of negative biogenic CO_2 emissions is possible when the input electricity is derived from renewable sources and the feedstock contains biomass or biogenic CO_2 sources in PEM, AE, and SOE processes. In this context, coupling the electrolysis with carbon capture technologies can lead to net-negative emissions. By integrating biogenic CO_2 into these processes, and utilizing renewable electricity, the system can contribute to a reduction in atmospheric CO_2 levels, resulting in net-negative biogenic CO_2 emissions. This approach aligns with carbon-negative strategies aimed at combating climate change by removing more CO_2 than is emitted, thereby establishing these processes as viable contributors to a sustainable carbon economy. Our results revealed that there was no significant change in the biogenic CO_2 emissions from the different electrolysis processes. The negative biogenic CO_2 emissions of -0.096, -0.108, and -0.088 kg-CO_2/kg-H_2 were observed for the SOE, PEM, and AE processes. The similarity in results among the PEM, AE, and SOE processes can be attributed to their shared

goal of splitting water into H_2 and O_2, despite differences in electrolyte type, operational temperature, and design. Each method effectively achieves high efficiencies under optimized conditions, especially when powered by renewable energy sources. While SOE operates at higher temperatures, leading to slightly different thermodynamic efficiencies, all three methods benefit from advanced catalyst developments and enhanced system integration, reducing variations in overall H_2 production efficiency. Moreover, when these systems utilize biogenic CO_2 capture, they demonstrate comparable carbon-negative potentials, as they all facilitate CO_2 conversion and sequestration with similar effectiveness, resulting in closely associated outcomes across these electrolysis technologies.

3.1.2. Nitrogen oxide, carbon monoxide, and methane emissions

Nitrogen oxide (NO_x), also referred to as laughing gas, is another major greenhouse gas that has an impact 298 times higher than CO_2 [26]. Many chemical facilities produce nitrogen oxides as by-products, including nitric acid and adipic acid factories, and catalytic converters are needed to handle N_2O [27]. In this context, the NO_x emissions are also critical atmospheric emissions from the electrolyzers for H_2 production. The NO_x emissions from SOE, PEM, and AE processes are reported in Figure 3. These results showed that the NO_x emissions are highest in the PEM electrolysis system, with an emission concentration of 3.66 kg-NO_x/kg-H_2. The SOE system has a similar but slightly lower NO_x emission level at 3.16 kg-NO_x/kg-H_2, and the AE system has the lowest NO_x emissions, at 2.68 kg-NO_x/kg-H_2. Basically, these differences are influenced by the interaction of nitrogen and oxygen at various operational conditions and by the energy sources and materials used in these electrolysis systems. The high NO_x emissions in the PEM system could be related to its operating environment, where nitrogen can interact with oxygen species, forming NO_x compounds. Although SOE operates at high temperatures, which could theoretically encourage NO_x formation, the system's design typically minimizes direct nitrogen exposure, keeping NO_x levels slightly lower. On the other hand, AE has the lowest NO_x emissions, largely due to the alkaline environment (KOH solution) and the low likelihood of nitrogen oxidation at its operating temperature. Nickel and stainless steel materials used in alkaline systems also contribute minimally to NO_x formation. Moreover, PEM electrolysis operates with a membrane that allows for efficient H_2 separation but often relies on grid electricity, which, if sourced from fossil fuels, can lead to higher indirect NO_x emissions. A similar trend also can be observed for the other electrolysis processes without the utilization of renewable energy resources.

In terms of CO emissions, PEM electrolysis emits the highest concentration at 10.29 kg-CO/kg-H_2, followed by SOE at 9.99 kg-CO/kg-H_2, and AE at 9.69 kg-CO/kg-H_2. The higher CO emissions in PEM and SOE systems can be linked to the operating temperatures and the types of catalysts and materials used. PEM electrolysis relies on a polymer electrolyte membrane, typically made from materials like Nafion, and requires precious metal catalysts such as platinum. These catalysts can enhance reaction rates, but at moderate operating temperatures (50-80 °C), incomplete oxidation can occur, leading to CO as a by-product. Furthermore, SOE systems are often designed to integrate waste heat or renewable energy sources, like solar or geothermal, which can further reduce indirect CO emissions by lowering the need for external fossil-based electricity.

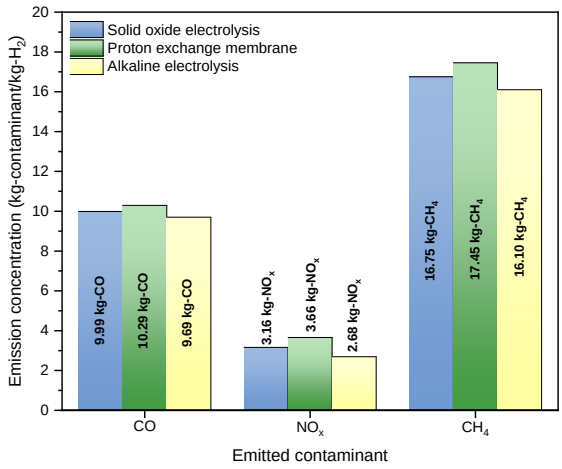

Figure 3. *The CO, NO_x, and CH_4 emissions from SOE, PEM, and AE processes.*

A similar trend was obtained for the CH_4 emissions. Namely, according to some reports, the CH_4 emissions from utilizing fossil fuels to produce H_2 would be comparable to those from using traditional natural gas sources to produce power [28]. Furthermore, the extraction and transportation of feedstocks can also result in CH_4 emissions from H_2 production activities; hence, incorporating these operations into the system boundaries results in a significantly greater contribution of CH_4 emissions to the impact of global warming [29]. Controlling CH_4 emissions from the extraction of feedstock and its transportation to the production of H_2 is therefore essential. Based on our results, the CH_4 emissions are most significant in PEM electrolysis with 17.45 kg-CH_4/ kg-H_2, followed by SOE at 16.75 kg-CH_4/ kg-H_2, and as expected, AE system with emission of 16.10 kg-CH_4/ kg-H_2. Overall, the materials and energy sources used in each electrolysis system significantly impact their emission profiles. In summary, the choice of electrolysis system should consider not only the direct emissions from the reaction process but also the environmental footprint of materials and the source of electricity used. Systems like AE, when powered by renewables or integrated with waste energy, offer lower overall emissions. In contrast, PEM and SOE systems may require cleaner electricity sources and careful management of catalyst and membrane materials to reduce indirect emissions.

3.1.3. Volatile organic carbon and sulfur oxide emissions

The SO_x emissions from the various H_2 production processes vary greatly; the environmental profiles of the gasification, electrolysis, and dark fermentation-microbial electrolysis cell (DF-MEC) processes are different. One notable source of SO_x emissions is gasification, especially when coal or other sulfur-containing feedstocks are used. During gasification, the sulfur in the feedstock is liberated as hydrogen sulfide (H_2S), which burns to produce SO_2, which causes acid rain and respiratory disorders. However, because electrolysis separates water into H_2 and O_2 without the need for any intermediates that contain sulfur, it produces very little SO_x emissions, particularly when it is fueled by renewable energy sources. In the same way, DF-MEC usually emits little SO_x. However, there may be very little SO_x emissions if the feedstocks include sulfur compounds. The SO_x emissions from the considered electrolysis processes are reported in Figure 4. When examining SO_x emissions, PEM Electrolysis has the highest emission rate at 4.65 kg SO_x/kg-H_2, whereas the SOE process emits 4.37 kg SO_x/kg-H_2, and the AE shows the lowest SO_x emissions at 4.11 kg SO_x/kg-H_2.

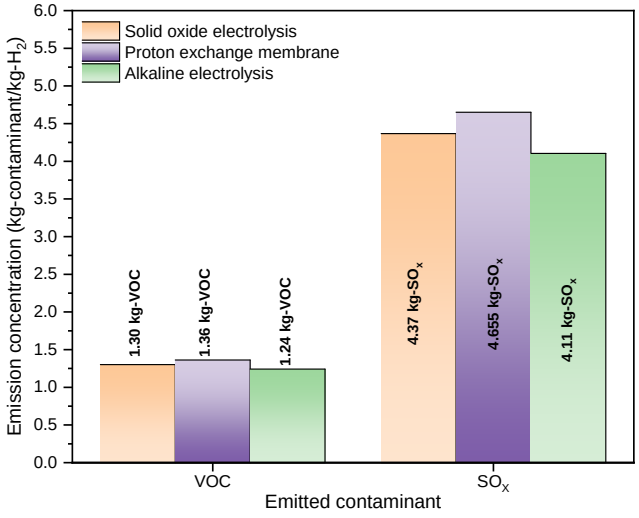

Figure 4. *The VOC and SO_x emissions from SOE, PEM, and AE processes.*

In addition, electrolysis processes present unique potential sources of VOC emissions, although generally low compared to fossil fuel-based processes. For instance, AE exhibits the lowest VOC emissions of 1.30 kg-VOC/kg-H_2, followed by SOE with 1.36 kg-VOC/kg-H_2, and PEM electrolysis with 1.42 kg kg-VOC/kg-H_2. The underlying reasons for these differences are primarily attributed to the distinct operating temperatures, electrolyte structures, and energy consumption patterns inherent to each electrolysis method. For instance, the SOE process typically operates at high temperatures, which enhances energy efficiency, but the elevated temperatures can partially promote the formation of VOC emissions. On the other hand, in PEM electrolyzers, VOC emissions may result from the degradation of polymeric materials within the membrane under prolonged exposure to high temperatures and operational stresses. The AE, which uses potassium hydroxide as the electrolyte, can also lead to VOC release if organic impurities present in the electrolyte or other system components degrade during operation. Overall, minimizing VOC emissions in these systems involves choosing durable materials, implementing effective sealing strategies, and controlling operating conditions to prevent thermal and chemical degradation.

3.1.4. Particulate matter emissions

Another significant problem is air pollution driven by particle matter (PMs), rather than SO_x and NO_x. Specifically, PMs can have a harmful influence on the environment, such as deteriorating air visibility, and on human health, such as cardiovascular disease and respiratory issues [30]. Additionally, the PMs are divided into two groups: $PM_{2.5}$, which is defined as particulate matter with a diameter of less than 2.5 µm, and PM_{10}, which is defined as particulate matter with a diameter of less than 10 µm. Because of its higher potential to cause health problems, $PM_{2.5}$ has been studied more than the other PMs [31]. Although they constitute a small percentage of all PM, $PM_{2.5}$ pollutants also have high surface-to-volume ratios, which enable them to concentrate sulfur compounds, nitrogen oxides, acids, heavy metals, bacteria, and more on their surfaces. Thus, it is essential to assess the PM emissions from the different H_2 production processes to comprehend their effects on the environment, create capturing methods, and/or implement stringent restrictions to reduce potential emissions. In this context, Figure 5 reports the $PM_{2.5}$ and PM_{10} emissions from the SOE, PEM, and AE H_2 production processes.

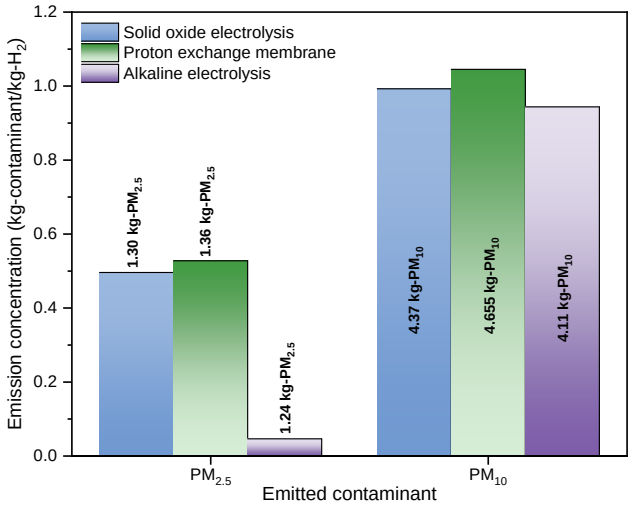

Figure 5. *The particulate matter emissions from SOE, PEM, and AE processes.*

Our results revealed that the highest PM emissions were observed for the PEM electolysis process with a $PM_{2.5}$ concentration of 1.36 kg-$PM_{2.5}$/kg-H_2 and a PM_{10} concentration of 4.65 kg-PM_{10}/kg-H_2. This result can be

explaine with that in PEM electrolysis process for H_2 production, sources of $PM_{2.5}$ and PM_{10} emissions primarily arise from indirect stages related to the manufacturing, transportation, and disposal of materials and energy inputs. These particles can be formed during the production of high-purity metals like platinum, iridium, and titanium, used in catalysts and cell components, which often involve mining and refining processes that emit fine particulates. In addition, if sourced from fossil fuel-based energy, the electricity used to power the electrolyzer contributes to particulate emissions through combustion processes, particularly coal or natural gas plants. Manufacturing of the PEM membranes and the operation of machinery involved in the assembly and maintenance of PEM systems also release PMs. Thus, while the electrolysis process does not emit $PM_{2.5}$ or PM_{10} directly, upstream and downstream processes associated with materials and energy production may contribute to PM emissions in the H_2 production lifecycle. Similar PM emissions values were observed for the SOE process with a $PM_{2.5}$ concentration of 1.30 kg-$PM_{2.5}$/kg-H_2 and a PM_{10} concentration of 4.37 kg-PM_{10}/kg-H_2. On the other hand, the lowest PM emissions were obtained for the AE process. For the AE process, the $PM_{2.5}$ and PM_{10} emissions were 1.24 kg-$PM_{2.5}$/kg-H_2 and 4.11 kg-PM_{10}/kg-H_2. The manufacturing of electrodes and other cell components involves mining and metallurgical processes that generate PM due to the handling, crushing, and smelting of metals. Additionally, the production of the alkaline electrolyte solution requires chemicals like potassium hydroxide (KOH) and its synthesis and transportation can lead to PM emissions.

3.2. Environmental impact assessment

In this section, critical environmental impact parameters like acidification potential (AP), aquatic eutrophication (AEP), global warming potential (GWP), and terrestrial eutrophication (TE) potentials of the electrolysis processes are evaluated using the coefficients of impact categories (Table 2), which are reported by Fallahpour et al. [32].

Table 2. *Characterization values of emissions for various environmental impact categories.*

Substance (in kg)	Global warming potential (in kg-CO_2eq./kg)	Acidification potential (in kg-SO_2eq./kg)	Terrestrial eutrophication potential (in kg-NO_xeq./kg)	Aquatic eutrophication potential (in kg-PO_4eq./kg)
CO_2	1	-	-	-
CH_4	21	-	-	-
SO_2	-	1	-	-
NO_x	-	0.28	1	0.13

Figure 6a reports the GWP and AP values of the processes based on their emissions of CO_2, CH_4, SO_2, and NO_x. Since it converts GHG emissions into CO_2 equivalent, the GWP is a widely recognized indicator for comprehending the environmental consequences of the systems and can be used to determine its overall emissions, making it one of the most significant LCA parameters of importance in this study [33].

The amount of toxic acid accumulated in soil, groundwater, surface water, and organisms, as well as variations in acidity and SO_2 emissions, are all represented by the AP. Fuel or biomass burning for energy production and transportation are the primary sources of emissions that become acidic [34]. For instance, the GWP and AP values of 4.71 kgCO_2-eq./kg-H_2 and 3.05 kg-SO_2eq./kg-H_2 are observed for the PEM electrolysis process most probably related to the production and disposal of materials like Nafion in PEMs contributing to GWP and acidification due to perfluorinated compounds. Moreover, the TE and AEP values are other important impact parameters considered in this paper, and these parameters for different electrolysis processes are illustrated in Figure 6b. Terrestrial (10.66 kg-NO_xeq./kg-H_2) and aquatic eutrophication (1.38 kg-PO_4eq./kg-H_2) potentials in PEM electrolysis are also influenced by the emissions from raw material extraction and membrane manufacturing.

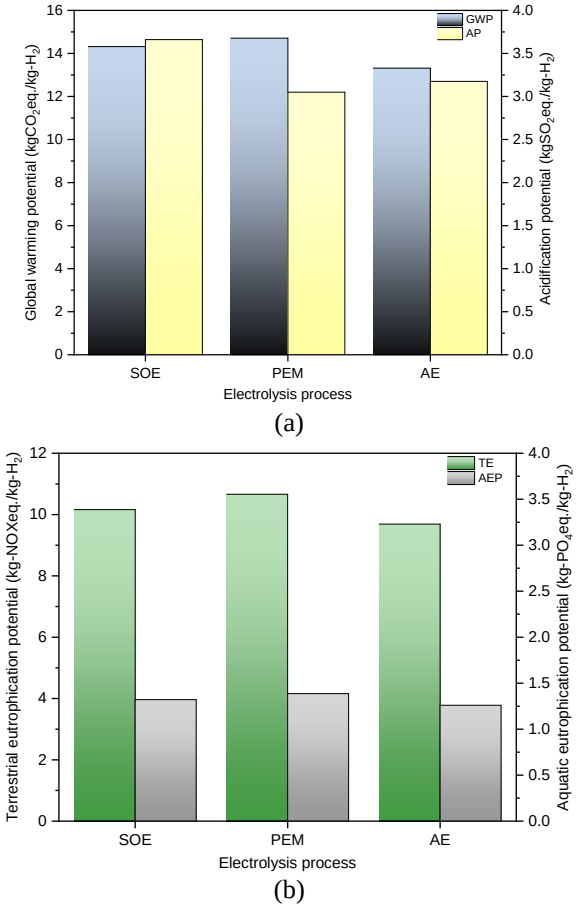

Figure 6. *Different electrolysis-based hydrogen production processes: (a) GWP and AP values and (b) TE and AEP values.*

For SOE processes, although the GWP value (4.31 kgCO_2-eq./kg-H_2) was similar to PEM, the AP value (3.66 kg-SO_2eq./kg-H_2) was found to be higher than PEM most probably related to its operating temperature. Namely, the high operating temperatures lead to material degradation, increasing the demand for replacement parts and,

consequently, environmental burdens from material production. Furthermore, ceramic materials in the SOE process can release pollutants during their production, contributing to acidification and eutrophication (TE: 10.16 kg-NO_xeq./kg-H_2 and AEP: 1.32 kg-PO_4eq./kg-H_2). On the other hand, the lowest environmental impacts are observed for the conventional AE process. For instance, the lowest GWP of 3.32 kgCO_2-eq./kg-H_2 is observed for the AE process, while its AP value was 3.17 kg-SO_2eq./kg-H_2. Moreover, the TE and AEP values were 9.69 kg-NO_xeq./kg-H_2 and 1.26 kg-PO_4eq./kg-H_2 for the AE process, respectively. These results revealed that the AE process, while typically less energy-intensive than PEM, still contributes to GWP due to the electricity source. The potassium hydroxide electrolyte used in AE can lead to acidification and eutrophication if released into the environment. Material processing and disposal stages, particularly involving electrodes, also contribute to environmental impacts. Consequently, across all these processes, the impact on acidification and eutrophication potentials is strongly correlated with raw material extraction, chemical use, and disposal practices, underscoring the importance of sustainable energy and material sourcing in mitigating these environmental effects.

Overall, this study extensively evaluates the atmospheric emissions and environmental impacts of three widely used water-based H_2 production methods: AE, SOE, and PEM. Among these, AE emerged as the most environmentally favorable option, exhibiting the lowest CO_2 emissions (3.28 kg-CO_2/kg-H_2), global warming potential (3.32 kg-CO_2-eq./kg-H_2), and particulate matter emissions (1.24 kg-$PM_{2.5}$/kg-H_2). Its straightforward design and scalability make AE a robust choice for integration with renewable energy sources, potentially achieving a fully sustainable H_2 production cycle. However, AE is not without its limitations, such as the dependency on chemical-intensive electrolytes like KOH, which may contribute to localized environmental concerns if improperly managed. Conversely, the PEM process demonstrated the highest CO_2 (4.68 kg-CO_2/kg-H_2), methane (17.45 kg-CH_4/kg-H_2), and particulate emissions (1.36 kg-$PM_{2.5}$/kg-H_2), primarily due to the complex and energy-intensive membrane production process involving precious metals. While PEM offers advantages in terms of operational flexibility, high H_2 purity, and compact system design, its environmental footprint and cost remain critical drawbacks. On the other hand, the SOE process, characterized by its high operating temperatures, exhibited intermediate environmental performance. Although SOE benefits from reduced electrical energy demands and the potential to harness industrial waste heat, its reliance on ceramic materials and high thermal energy inputs presents challenges, particularly in terms of material degradation and acidification potential (3.66 kg-SO_2eq./kg-H_2).

One of the major contributions of this study lies in its comprehensive lifecycle approach, incorporating emissions from feedstock utilization, transportation, and operational phases. It highlights critical emission hotspots, such as membrane production in PEM and thermal energy requirements in SOE, and underscores the importance of renewable energy integration to mitigate environmental impacts. However, the study also reveals systemic challenges shared across all processes, including significant methane emissions (ranging from 16.1 to 17.45 kg-CH_4/kg-H_2) and indirect emissions tied to electricity generation. These findings stress the necessity of optimizing material selection, improving operational efficiencies, and transitioning to cleaner energy grids to enhance the sustainability of H_2 production.

Consequently, a key advantage of this study is its holistic approach to assessing the environmental impacts of H_2 production methods, integrating lifecycle emissions from feedstock utilization to operational phases using the GREET model. This comprehensive methodology allows for a detailed comparison of the processes. Additionally, its inclusion of a broad spectrum of atmospheric emissions, such as CO_2, CH_4, and PM, enhances its relevance and applicability for sustainability assessments. However, the study also has limitations such as while it evaluates environmental parameters comprehensively, it does not delve deeply into the economic viability or scalability challenges of the processes, particularly for emerging technologies like SOE. Moreover, the dependency on renewable energy sources for achieving optimal performance, while crucial, introduces variability that may not be practical in regions with limited access to clean energy. Nevertheless, this study provides a robust framework for identifying both the advantages and limitations of water-based H_2 production methods, offering valuable insights for policymakers and industry stakeholders aiming to achieve long-term environmental and energy sustainability.

Moreover, based on the current findings, future research should address both the technological and methodological gaps identified in this study to advance the sustainability of H_2 production. While the GREET software provides a robust framework for lifecycle analysis, certain limitations must be acknowledged. For instance, the model's reliance on standardized datasets may overlook regional variations in energy grids, feedstock availability, and material production methods, leading to discrepancies in real-world applicability. Future studies should aim to integrate region-specific data and incorporate more detailed assessments of upstream emissions. Additionally, the analysis would benefit from including more comprehensive economic evaluations. These could encompass the capital and operational costs of electrolysis technologies, including material sourcing, system maintenance, and infrastructure development, as well as long-term financial projections under various energy market scenarios. Moreover, the high dependence on renewable energy sources for achieving optimal emissions reductions highlights the need to evaluate the feasibility and cost of

renewable energy integration across different regions. Future work should also explore the potential of coupling these electrolysis systems with carbon capture and utilization (CCU) technologies to mitigate methane and CO_2 emissions further and achieve net-negative emissions. Hybrid systems, combining the strengths of AE, PEM, and SOE, represent another promising area for exploration, potentially balancing the low emissions of AE with the efficiency and operational flexibility of PEM. Finally, expanding the scope of the environmental impact assessment to include social and economic dimensions, such as supply chain resilience, and public acceptance, will provide a more holistic understanding of the role of H_2 production in sustainable energy transitions. By addressing these aspects, future research can build on the solid foundation laid by this study to facilitate the practical implementation of environmentally and economically sustainable H_2 technologies.

4. Conclusions

This study offers a detailed environmental evaluation of AE, SOE, and PEM electrolysis processes for H_2 production, highlighting significant variations in their sustainability profiles. AE emerged as the most environmentally favorable method, with CO_2 emissions of 3.28 kg-CO_2/kg-H_2, methane emissions of 16.1 kg-CH_4/kg-H_2, and the lowest $PM_{2.5}$ emissions of 1.24 kg-$PM_{2.5}$/kg-H_2. These results confirm the potential of the AE process as a low-impact, renewable-compatible H_2 production process. On the other hand, PEM exhibited the highest CO_2 emissions at 4.68 kg-CO_2/kg-H_2 and the most significant methane emissions (17.45 kg-CH_4/kg-H_2), largely due to its reliance on energy-intensive membrane production and the use of precious metals. SOE, while showing some promise with reduced electrical energy demands, recorded CO_2 emissions of 4.28 kg-CO_2/kg-H_2 and the highest acidification potential at 3.66 kg-SO_2eq./kg-H_2, attributed to its high operational temperatures and material requirements. Notably, all systems demonstrated similar biogenic CO_2 emissions, ranging from -0.088 to -0.108 kg-CO_2/kg-H_2, indicating their potential for carbon-negative operations when integrated with renewable energy and carbon capture technologies.

Overall, these findings highlight the urgent need for innovation in material design, particularly for PEM and SOE, and the broader adoption of renewable energy grids to reduce lifecycle emissions. Future research should prioritize economic feasibility studies, hybrid system designs that combine the strengths of different electrolysis methods, and strategies to mitigate indirect emissions, such as methane and acidification precursors. By addressing these challenges, H_2 production can evolve into a cornerstone technology for achieving global energy sustainability and decarbonization goals.

References

[1] J. Turner, G. Sverdrup, M.K. Mann, P. Maness, B. Kroposki, M. Ghirardi, R.J. Evans, D. Blake, Renewable hydrogen production, Int. J. Energy Res. 32 (2008) 379–407.

[2] F. Suleman, I. Dincer, M. Agelin-Chaab, Environmental impact assessment and comparison of some hydrogen production options, Int. J. Hydrogen Energy. 40 (2015) 6976–6987.

[3] I. Dincer, C. Acar, Review and evaluation of hydrogen production methods for better sustainability, Int. J. Hydrogen Energy. 40 (2015) 11094–11111.

[4] A.Y. Goren, I. Dincer, A. Khalvati, A Comprehensive Review on Environmental and Economic Impacts of Hydrogen Production from Traditional and Cleaner Resources, J. Environ. Chem. Eng. (2023) 111187.

[5] M. David, C. Ocampo-Martínez, R. Sánchez-Peña, Advances in alkaline water electrolyzers: A review, J. Energy Storage. 23 (2019) 392–403.

[6] Y. Zhu, Y. Zhang, S. Bin, Z. Chen, F. Zhang, S. Gong, Y. Xia, X. Duan, Effects of key design and operating parameters on the performance of the PEM water electrolysis for hydrogen production, Renew. Energy. (2024) 121290.

[7] L. Järvinen, P. Puranen, V. Ruuskanen, A. Kosonen, P. Kauranen, J. Ahola, C. Chatzichristodoulou, Experimental study of alkaline water electrolyzer performance and frequency behavior under high frequency dynamic operation, Int. J. Hydrogen Energy. 67 (2024) 50–61.

[8] L.A. Jolaoso, C. Duan, P. Kazempoor, Life cycle analysis of a hydrogen production system based on solid oxide electrolysis cells integrated with different energy and wastewater sources, Int. J. Hydrogen Energy. 52 (2024) 485–501.

[9] R.K. Iyer, J.H. Prosser, J.C. Kelly, B.D. James, A. Elgowainy, Life-cycle analysis of hydrogen production from water electrolyzers, Int. J. Hydrogen Energy. 81 (2024) 1467–1478.

[10] Y. Kim, I. Min, J. Lee, H. Yang, An Analysis of Greenhouse Gas Emissions in Electrolysis for Certifying Clean Hydrogen., Energies (19961073). 17 (2024).

[11] J. Zhang, Z. Wang, Y. He, M. Li, X. Wang, B. Wang, Y. Zhu, K. Cen, Comparison of onshore/offshore wind power hydrogen production through water electrolysis by life cycle assessment, Sustain. Energy Technol. Assessments. 60 (2023) 103515.

[12] X. Wei, S. Sharma, A. Waeber, D. Wen, S.N. Sampathkumar, M. Margni, F. Maréchal, Comparative life cycle analysis of electrolyzer technologies for hydrogen production: Manufacturing and operations,

Joule. (2024).

[13] O. Siddiqui, I. Dincer, A well to pump life cycle environmental impact assessment of some hydrogen production routes, Int. J. Hydrogen Energy. 44 (2019) 5773–5786.

[14] C. Zhang, J.B. Greenblatt, M. Wei, J. Eichman, S. Saxena, M. Muratori, O.J. Guerra, Flexible grid-based electrolysis hydrogen production for fuel cell vehicles reduces costs and greenhouse gas emissions, Appl. Energy. 278 (2020) 115651.

[15] C.A. Grimes, O.K. Varghese, S. Ranjan, Light, water, hydrogen: the solar generation of hydrogen by water photoelectrolysis, Springer, 2008.

[16] A. Manabe, M. Kashiwase, T. Hashimoto, T. Hayashida, A. Kato, K. Hirao, I. Shimomura, I. Nagashima, Basic study of alkaline water electrolysis, Electrochim. Acta. 100 (2013) 249–256.

[17] P. Lerch, F. Scheller, D.G. Reichelt, K. Menzel, T. Bruckner, Electricity cost and CO2 savings potential for chlor-alkali electrolysis plants: Benefits of electricity price dependent demand response, Appl. Energy. 355 (2024) 122263.

[18] A. Jun, J. Kim, J. Shin, G. Kim, Achieving high efficiency and eliminating degradation in solid oxide electrochemical cells using high oxygen-capacity perovskite, Angew. Chemie Int. Ed. 55 (2016) 12512–12515.

[19] J. Laurencin, J. Mougin, High-Temperature Steam Electrolysis, Hydrog. Prod. Electrolysis. (2015) 191–272.

[20] A. Brisse, J. Schefold, M. Zahid, High temperature water electrolysis in solid oxide cells, Int. J. Hydrogen Energy. 33 (2008) 5375–5382.

[21] L.J. Nuttall, A.P. Fickett, W.A. Titterington, Hydrogen generation by solid polymer electrolyte water electrolysis, Hydrog. Energy Part A. (1975) 441–455.

[22] B. Yang, Z. Zhang, S. Su, J. Li, J. Wang, R. Zhang, H. Shu, Y. Ren, L. Jiang, Y. Sang, Optimal scheduling of wind-photovoltaic-hydrogen system with alkaline and proton exchange membrane electrolyzer, J. Power Sources. 614 (2024) 235010.

[23] S.E. Haque, Historical perspectives on climate change and its influence on nature, in: Vis. Tech. Clim. Chang. with Mach. Learn. Artif. Intell., Elsevier, 2023: pp. 15–38.

[24] R. Bhandari, C.A. Trudewind, P. Zapp, Life cycle assessment of hydrogen production via electrolysis–a review, J. Clean. Prod. 85 (2014) 151–163.

[25] J. Zhang, B. Ling, Y. He, Y. Zhu, Z. Wang, Life cycle assessment of three types of hydrogen production methods using solar energy, Int. J. Hydrogen Energy. 47 (2022) 14158–14168.

[26] H.-Y. Chen, J.-C. Jeng, Integration of hydrogen production and greenhouse gas treatment by utilizing nitrogen oxide as sweep gas in a solid oxide electrolysis cell, J. Taiwan Inst. Chem. Eng. 130 (2022) 103937.

[27] K.O. Denisova, A.A. Ilyin, R.N. Rumyantsev, A.P. Ilyin, A. V Volkova, Nitrous oxide: Production, application, and protection of the environment, Russ. J. Gen. Chem. 89 (2019) 1338–1346.

[28] C. Bauer, K. Treyer, C. Antonini, J. Bergerson, M. Gazzani, E. Gencer, J. Gibbins, M. Mazzotti, S.T. McCoy, R. McKenna, On the climate impacts of blue hydrogen production, Sustain. Energy Fuels. 6 (2022) 66–75.

[29] Y.A. Alhamdani, M.H. Hassim, R.T.L. Ng, M. Hurme, The estimation of fugitive gas emissions from hydrogen production by natural gas steam reforming, Int. J. Hydrogen Energy. 42 (2017) 9342–9351.

[30] W.G. Tucker, An overview of PM2. 5 sources and control strategies, Fuel Process. Technol. 65 (2000) 379–392.

[31] C.I. Davidson, R.F. Phalen, P.A. Solomon, Airborne particulate matter and human health: a review, Aerosol Sci. Technol. 39 (2005) 737–749.

[32] F. Fallahpour, A. Aminghafouri, A. Ghalegolab Behbahani, M. Bannayan, The environmental impact assessment of wheat and barley production by using life cycle assessment (LCA) methodology, Environ. Dev. Sustain. 14 (2012) 979–992.

[33] Y. Zhou, D. Swidler, S. Searle, C. Baldino, Life-cycle greenhouse gas emissions of biomethane and hydrogen pathways in the European Union, (2021).

[34] A.D. La Rosa, Life cycle assessment of biopolymers, in: Biopolym. Biotech Admixtures Eco-Efficient Constr. Mater., Elsevier, 2016: pp. 57–78.

MANAS Journal of Engineering
ISSN 1694-7398 | e-ISSN 1694-7398

Volume 13, Issue 1, (2025) Pages 52-63
https://doi.org/10.51354/mjen.1656854

Efficient degradation of phenol by electrooxidation process at boron-doped diamond anode system

Nawid Ahmad Akhtar[1*], Mehmet Kobya[1,2]

[1] Department of Environmental Engineering, Kyrgyz-Turkish Manas University, 720038 Bishkek, Kyrgyzstan, nawidahmad.akhtar@manas.edu.kg, ORCID: 0009-0006-5390-7505

[2] Department of Environmental Engineering, Gebze Technical University, 41400 Gebze, Türkiye, kobya@gtu.edu.tr, ORCID: 0000-0001-5052-7220

ABSTRACT

The rapid increase in global population and industrialization has led to increased environmental pollution, primarily due to insufficient treatment technologies and the depletion of freshwater resources. This research investigates the impact of the electrooxidation (EO) process using Boron Doped Diamond (BDD) anode on phenol degradation, energy consumption, total operating costs, and anode efficiency. The study was carried out on different current densities (j = 50-200 A/m^2), initial pH (3.6-9.6), initial phenol concentration (C_i = 100-800 mg/L), and supporting electrolyte concentration (SEc = 2-6 g NaCl/L). The phenol removal efficiency under optimum conditions (anode = BDD, j = 200 A/m^2, initial pH = 7.6, C_{phenol} = 100 mg/L, and SE_c = 4 g NaCl/L) was determined to be 100% after 50 min of EO reaction time. However, the energy consumption and total operating cost under these conditions were 12.7 kWh/m^3 (420 kWh/kg phenol) and 0.99 $/m^3 (7.88 $/kg phenol), respectively. Moreover, BDD anode efficiencies were calculated as 6.39, 3.47, and 1.74 g phenol/Ahm^2 at current densities of 50, 100, and 200 A/m^2, respectively. Consequently, the EO process is a more cost-effective treatment approach for efficient phenol removal from an aqueous solution.

ARTICLE INFO

Research article

Received: 13/03/2025
Accepted: 16/05/2025

Keywords:
Phenol
Degradation,
Electrooxidation,
BDD anode Operating costs

*Corresponding author

1. Introduction

With the increasing population and developing technology, industrial capacity is increasing. This increases the consumption of natural resources and water. Water consumed in industrial areas returns to nature as polluted water [1]. Phenol compounds are generally found in significant amounts in wastewater from the paper industry [2] and olive oil production facilities [3], oil refineries [4], [5], coke ovens [6], textile production facilities [7], iron and steel mills [8], and gas production facilities [9]. Therefore, it has become mandatory to treat wastewater in a way that prevents the pollution of natural water resources [10]. Phenols, especially in the structure of industrial wastewater, are persistent aromatic organic compounds in which one or more hydroxyl groups are attached to the aromatic ring [11]. International regulatory agencies have established stringent limits on phenol discharge into the environment; for instance, the United States Environmental Protection Agency (USEPA) has mandated that phenol content in surface water must not exceed 1 ppb [12]. Phenol, which considerably impacts water quality, is unpleasant even at minimal concentrations. A phenol content of 2.5 mg/L results in an unpleasant taste and odor [13]. High concentrations terminate all vital environmental activities [14]. Due to its harmful effects, it is among the primary pollutants.

Therefore, the efficient treatment of phenol-contaminated water is of great importance for human and environmental health [15]. One of the most significant issues in wastewater management is the development of efficient treatment methods that can efficiently eliminate contaminants and mitigate their toxicity to organisms [16,17]. In the existing literature, different treatment processes have been used to remove phenol wastewater, such as distillation [18], adsorption [19,20], chemical oxidation [21], enzymatic treatment [22], membrane technology [23,24], electrooxidation [25], electro-Fenton [26], and photocatalytic process [27]. Although these processes are efficient in phenol removal, their use is not recommended for phenol removal [28]. For example, one of the major drawbacks of using extractive membrane bioreactors for phenol removal is that the combination of several systems requires a large area and many variables need to be adjusted frequently [29]. The use of reverse osmosis and nanofiltration technology for phenol removal is more suitable for treating water with low phenol

concentrations but not for high concentrations and is difficult to choose because it requires replacement of the fouled membrane or chemical cleaning [23]. On the other hand, membrane distillation is not recommended for phenol removal due to poor phenol separation due to limited membrane selectivity, and the high cost of setting up the system [30]. Therefore, there is a need for a process for phenol oxidation that does not have these disadvantages [28]. Recently, electrooxidation (EO), as one of the electrochemical methods, has been a highly efficient process for phenol removal [25]. When subjected to an electrical current, hazardous or non-biodegradable chemicals undergo oxidation, resulting in their transformation into biodegradable compounds or total oxidation into carbon dioxide (CO_2), water (H_2O), and readily degradable organic molecules [31,32]. The EO process offers several advantages in the degradation of organic substances. These include a notably high level of efficiency, as it effectively breaks down organic compounds [33]. Additionally, EO does not require the addition of chemical reagents, which simplifies the treatment process. The use of EO also leads to significantly reduced retention times, preventing the formation of sludge [10,34]. Furthermore, EO can be seamlessly integrated into existing treatment processes due to its straightforward structural design, the process is also easily controlled, making it manageable for operators [6]. Lastly, EO is environmentally friendly, as the primary reagent used possesses electron properties that contribute to its eco-friendliness [35-37].

This study seeks to assess the impact of BDD anode on phenol removal across different current densities, initial pH, phenol concentrations, and supporting electrolyte concentrations through the EO process. Furthermore, specific energy consumption (in kWh/m^3 and kWh/kg phenol removal), total operating costs ($/$m^3$ and $/kg phenol removed), and anode efficiency (in g phenol removal/Ahm^2) were evaluated.

2. Materials and methods

2.1. Materials and chemicals

The investigation employed high-quality chemicals, all of which were obtained from Merck (Germany). However, phenol was obtained from Kimya Borsası (Turkey). In the EO process, the anode used in this study is a BDD, which is composed of a layer of boron diamond film deposited on a 1.5 mm niobium plate (Nb/BDD) obtained from DiaCon GmbH, Germany. The cathode is made of stainless steel (SS) sourced from Turkey (316 AISI SS). The tap water used in the study was measured as initial pH (7.60), temperature (T, 13 °C), electrical conductivity (420 µs/cm), total hardness (310 mg HCO_3^-/L), total dissolved solids (TDS, 220 mg/L), magnesium (Mg^{2+}, 68 mg/L), calcium (Ca^{2+}, 102 mg/L), sodium (Na^+, 94 mg/L), potassium (K^+, 11 mg/L), chloride (Cl^-, 78 mg/L), and sulfate (SO_4^{2-}, 175 mg/L). However, the phenol synthetic stock solution was prepared by dissolving the required amount of phenol in tap water.

2.2. Experimental setup and procedure

All EO experiments were performed in a cylindrical batch glass reactor (V = 750 mL, diameter = 10 cm, and height = 12.5 cm). In the EO experiments, rectangular anode and cathode plate electrodes used were of the same size (length = 20 cm, width = 6 cm, and thickness 3 mm). The length of the contact area of the electrodes in the effluent in the EO reactor is = 10 cm, the distance between the electrodes is 1.5 cm, and the active surface area of the anode electrode is 0.012 m^2. The electrodes in the reactor were placed vertically, parallel to each other. The electrodes were fixed 1.5 cm above the bottom of the EO reactor. For each experimental study, 550 mL of wastewater was used. In the EO process, after the electrodes were connected to the respective (+) or (-) poles of the power supply (Gwinstek DC SPS-606, 0-6 A and 0-60 V), the required current and voltage settings were made. During the operational period, water was agitated using a magnetic stirrer set at a rotational speed of 250 rpm. Samples were taken from the EO reactor at different operating times, each sample was passed through a 0.45 mm membrane filter before analysis. Then, phenol and output pH analyses were performed. All experiments of the EO process were carried out at room temperature (25 ± 1 °C). A schematic representation of an EO reactor is given in (Figure. 1).

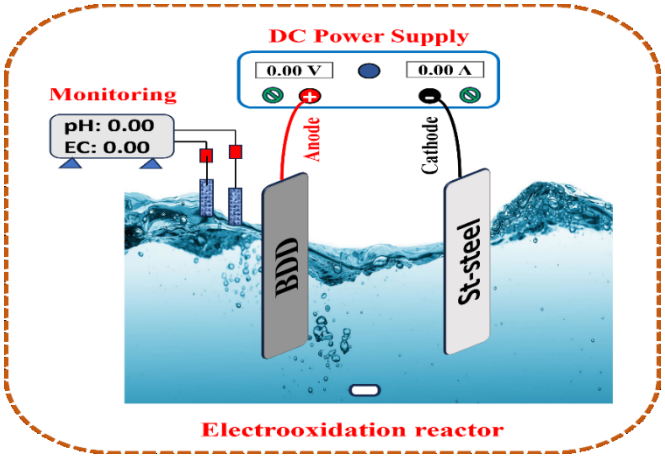

Figure 1. *Schematic representation of the electrooxidation process.*

2.3. Analytical methods

All experiments were assessed using the Standard Method guidelines for water and wastewater analysis [38]. A UV-vis spectrophotometer (Helios, Thermo Aquamate 2000E, UV-Vis spectrometer) was used to measure the absorbance of the colored phenol 4-aminoantipyrine complex at a wavelength of 500 nm. The absorbance value obtained was then compared with the calibration curve. The pH and conductivity were measured using the Thermo Scientific Eutech pH 150 (Singapore) and YSI model 30 (USA). The analyses were

performed in duplicates, and the data averages were reported if the test error was below 1%.

3. Results and discussion

3.1. Impact of current density

The current density is often considered the principal variable in the EO process because of its impact on the reaction rate. Current density is calculated by dividing a specified current (i) by the associated effective electrode surface area ($j = i/A_{electrode}$, A/m^2, or mA/cm^2) [31,37,39]. As shown in (Figure. 2a), under optimum conditions (anode = BDD, initial pH = 7.6, C_i = 100 mg/L, and SE_c = 6 g NaCl/L), the phenol output concentration was calculated as 8 mg/L (92.0%) after 60 min at 50 A/m^2, and 0.001 mg/L (100%) after 60 min at 100 A/m^2, and 0.001 mg/L (100%) after 50 min at 200 A/m^2, respectively. The study by Amado-Piña et al. (2017) calculated 98% on the removal of 100 mg/L phenol under optimum conditions such as anode = BDD, pH = 7.0, j = 600 A/m^2, and room temperature [40]. The results demonstrate a clear relationship between current density and removal efficiency, with an observed increase in removal efficiency as current density increases [10]. This suggests a positive correlation between current density and both mass transport and phenol concentration [41]. This correlation may be attributed to the enhanced generation of •OH radicals during the oxidation process, which potentially contributes to a higher level of efficiency in the removal process [42]. It is crucial to recognize that augmenting the current density does not always result in enhanced efficiency or oxidation rates. The effect of current density on removal efficiency, particularly for a certain anode material, is contingent upon the distinct properties of the effluent or aqueous medium requiring treatment [37]. Conversely, using larger current densities often leads to elevated operational expenses as a consequence of increased energy consumption [33]. The poor adsorption of hydroxyl radicals, which exhibit high reactivity towards organic molecules, may be attributed to the inert surface of the BDD anode [10]. The BDD anode may be characterized as a "non-active" anode due to its lack of catalytically active sites for the adsorption of reactants and/or products in an aqueous medium [33]. Therefore, non-active anodes, such as BDD, are considered favorable electrodes for fully oxidizing organic compounds to H_2O and CO_2 Eqs (1-3).

$$BDD + H_2O \rightarrow BDD(\bullet OH) + H^+ + e^- \quad (1)$$
$$BDD(\bullet OH) + R \rightarrow BDD + mCO_2 + nH_2O \quad (2)$$
$$BDD(\bullet OH) \rightarrow BDD + 0.5O_2 + H + e^- \quad (3)$$

Another important parameter in the EO process is the change of pH during the process stage [6], as can be seen in (Figure. 2b), from the optimum pH = 7.60, after 60 min at current densities of 50, 100, and 200 A/m^2 the final pH values decreased from 7.60 to 7.05 for 50 A/m^2, from 7.60 to 6.74 for 100 A/m^2, and from 7.60 to 6.24 for 200 A/m^2, respectively. As it can be seen from (Fig. 2a), the concentration of phenol remaining after 50 min at current densities of 100 and 200 A/m^2 was calculated to be 2 and 0.001 mg/L, it can be said that increasing the current density from 100 to 200 A/m^2 has a relatively weaker effect on phenol removal, which is explained by the fact that the removal of phenol is slower in acidic environments of pH. Another important parameter is the voltage (V) variation of the cell in the EO process because it is the most important parameter affecting the energy consumption in the EO process, as can be seen from (Figure. 2c), the applied V values after 1 hour at different current densities of 50, 100, and 200 A/m^2 using electrolyte with a constant 4 g/L NaCl support changed from 8.80 to 8.87 for 50 A/m^2, from 9.30 to 9.34 for 100 A/m^2, and from 10.50 to 10.25 for 200 A/m^2, respectively. Moreover, BDD anode efficiencies (as calculated by Eq. 9) were calculated as 6.39, 3.47, and 1.74 g phenol/Ahm^2 at current densities of 50, 100, and 200 A/m^2, respectively

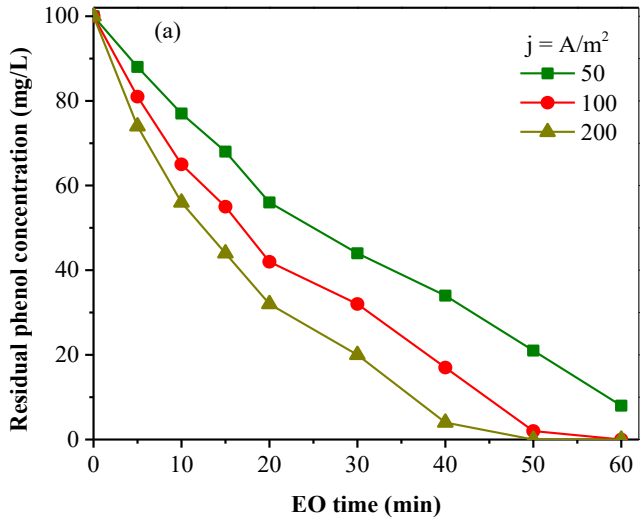

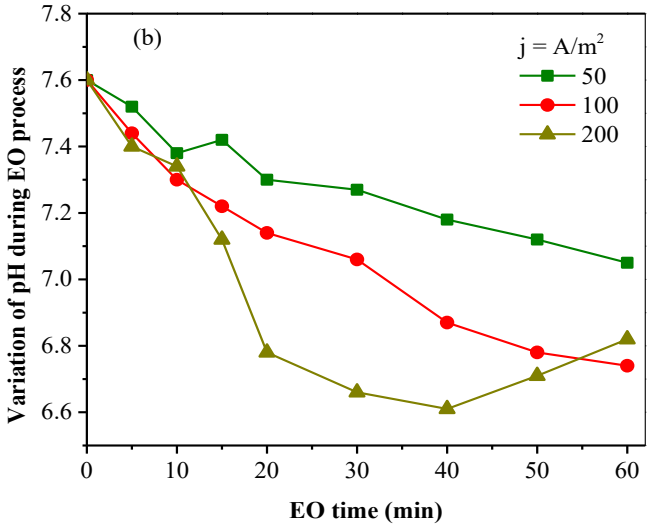

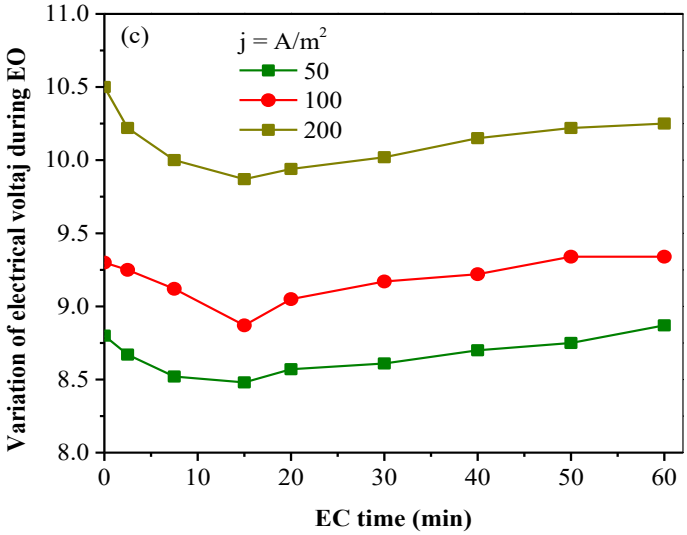

Figure 2. *Impact of different current densities on (a) phenol removal, (b) initial pH variation, and (c) electrical voltage variation*

Energy consumption and cost-effectiveness of the EO process are crucial criteria for the adoption of wastewater treatment technologies in industrial applications. The main cost components associated with the treatment of phenol-contaminated wastewater by the EO process are electricity consumption and the use of chemicals. The energy consumption (as kWh/m^3) for the EO process, the magnetic stirrer, and the total energy consumption for the process were calculated using Eqs. (4-6), respectively. However, the specific energy consumption (SEC) is the amount of energy used per unit mass of phenol removed from wastewater (in kWh/kg phenol). The SEC for phenol was determined using Eq. (7).

$$C_{energy}\ (kWh/m^3) = \frac{i \times t \times U}{v} \quad (4)$$

$$C_{magnetic\ stirrer\ energy}\ (kWh/m^3) = \frac{N \times t}{v \times \eta\ (\%)} \quad (5)$$

$$C_{total\ energy}\ (kWh/m^3) = C_{energy} + C_{magnetic\ stirrer\ energy} \quad (6)$$

$$SEC\ (kWh/kg\ phenol) = \frac{i \times t_{EO} \times U}{phenol_{rem}} \quad (7)$$

$$OC_{EO}\ (\$/m^3) = \alpha \times C_{energy} + \beta \times C_{chemicals} \quad (8)$$

where i is the applied current (amperes, A), U is the cell voltage (volts, V), t is the duration of the EO process (in hours), v is the volume of treated wastewater (in m^3), and $phenol_{rem}$ is the phenol removed from the solution.
The total operating cost for the EO process was determined by using Eq. (8).

where α indicates the unit cost of electrical energy, C_{energy} indicates the total energy consumption related to the operations, β indicates the unit prices of chemicals, and $C_{chemical}$ symbolizes the quantities of chemicals used (in kg). In March 2025, Kyrgyzstan's market recorded an electrical energy price of 0.062 $/kWh. The unit costs for the chemicals used in the research were as follows: NaOH had a unit price of 0.40 $/kg; HCl had a unit price of 0.45 $/kg; and NaCl had a unit price of 0.05 $/kg [43].

During the EO process, the anode efficiencies (η) represent the amount of phenol removed (g) from
the wastewater per hour, per ampere, and per square meter. The anode efficiencies (η) for phenol were determined using Eq. (9). The $S_{electrode}$ is the active anode area inside the EO reactor.

$$\eta\ (g\ phenol/Ahm^2) = \frac{(phenol_i - phenol_t) \times v}{i \times S_{electrode}} \quad (9)$$

The applied current, EO duration, and voltage between the anode and cathode directly determine the energy used in the EO process [37]. As can be seen from (Figure. 3), the specific energy consumption (SEC) and total operating costs (OC), under optimum conditions (anode = BDD, pH = 7.60, C_i = 100 mg/L, C_i = 100 mg/L, and SE_c = 4 gNaCl/L) for three different current densities were calculated as 3.73 kWh/m^3 (123. 2 kWh/kg phenol) and 0.43 $/m^3 (2.31 $/kg phenol) for 50 A/m^2, and 6.75 kWh/m^3 (233.2 kWh/kg phenol) and 0.62 $/m^3 (4.19 $/kg phenol) for 100 A/m^2, and 12.71 kWh/m^3 (420.0 kWh/kg phenol) and 0.99 $/m^3 (7.88 $/kg phenol) for 200 A/m^2, respectively. As can be seen from the results, the SEC and total OC of oxidation of the phenol increased with higher current densities. This resulted from the elevated electrical energy consumption resulting from the increased applied current density. Conversely, the efficiency of the anode decreased as the current density increased. Increasing the current density should enhance the removal of contaminants. However, it is expected that the current efficiency will decrease as a result of mass transport limits [37]. The results show that the 50 A/m^2 has the lowest SEC and total OC, while the 200 A/m^2 has the highest SEC and total OC.

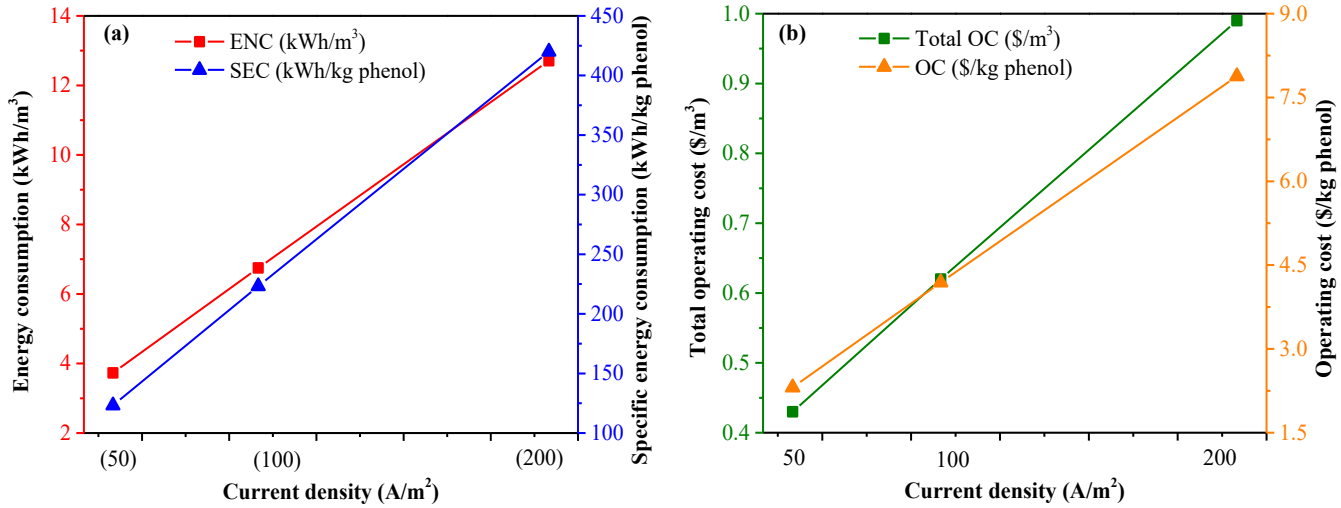

Figure 3. *Impact of different current densities on (a) specific energy consumption and (b) total operating costs.*

3.2. Impact of initial pH

The only controlled parameter in the EO process is pH, so the initial pH of the study is the most important parameter affecting the process efficiency [6]. As seen from (Figure. 4a), the phenol output concentration at different pH values between 3.6 and 9.6 under optimum conditions (anode = BDD, j = 200 A/m^2, C_i = 100 mg/L, and SE_c = 4 g NaCl/L) were calculated as 6 mg/L (Re = 94%) for pH 3.6 after 60 min, and 0.001 mg/L (Re = 100%) for pH 5.6 after 60 min, and 0.001 mg/L (Re = 100%) for pH 7.6 after 50 min, and 0.001 mg/L (Re = 100%) for pH 9.6 after 60 min, respectively. The results showed that the optimum pH for phenol removal by the EO process was 7.6. This indicates that degradation with the BDD anode was successful throughout a wide spectrum of pH values, implying that pH adjustment is unnecessary, provided that the pH is not above 9.6 [44]. As a result, the expenses related to treatment will decrease in actual implementations. The results demonstrate that the removal efficiency of all selected pollutants in phenol was optimal at an initial pH of 7.6 and markedly diminished under very acidic (pH 3.6) and alkaline (pH 9.6) conditions. The efficacy of phenol elimination decreased under acidic circumstances because of the instability of $OH^{\bullet}$ radicals. However, it markedly improved in alkaline solutions due to the generation of OCl^- ions, indicating that natural or basic pH values were more favorable [45]. In acidic conditions, the reverse reaction takes place, resulting in the combination of OCl^- and H^+ ions to form $HOCl^-$ (as shown in Eqs. 10 and 11). Consequently, OCl^- ions demonstrate a propensity for an alternative reaction rather than oxidizing the pollutants, mostly due to their intrinsic instability [46]. Moreover, acidic conditions substantially reduce the concentration of important oxidative radicals, such as $^{\bullet}OH$ radicals, produced at the anodes [45]. Furthermore, several chlorine species, including OCl^- and Cl_2, may be converted into ClO_3 Eq (12) or ClO_4 Eqs (13–16) under very alkaline conditions. These ions possess a restricted ability to oxidize and eliminate organic compounds. These characteristics together account for the decreased effectiveness of EO in alkaline conditions [47].

$$2Cl \rightarrow Cl_2 + 2e^- \quad (10)$$
$$Cl_2 + H_2O \rightarrow HOCl^- + Cl^- + H^+ \quad (11)$$
$$HOCl^- + H_2O \rightarrow 2ClO_3 + 4Cl^- + 12H^+ + 1.5O_2 + 6e^- \quad (12)$$
$$Cl^- + OH^- \rightarrow OCl^- + H^+ + e^- \quad (13)$$
$$OCl^- + OH^- \rightarrow ClO_2 + H + e^- \quad (14)$$
$$ClO_2 + OH^- \rightarrow ClO_3 + H + e^- \quad (15)$$
$$ClO_3 + OH^- \rightarrow ClO_4 + H + e^- \quad (16)$$

On the other hand, the outlet pH of the effluent after the EO process is important for the receiving environment, as can be seen from (Figure. 4b), the outlet pH after the EO process was 4.12, 5.37, 6.82, and 8.15 for the initial pH of 3.6, 5.6, 7.6, and 9.6, respectively. The results show that the initial pH of the study (7.6) is optimal because changing the initial pH of the solution requires the use of additional chemicals, which increases operating costs. Therefore, it is more advantageous to conduct the study at an initial pH of 7.6.

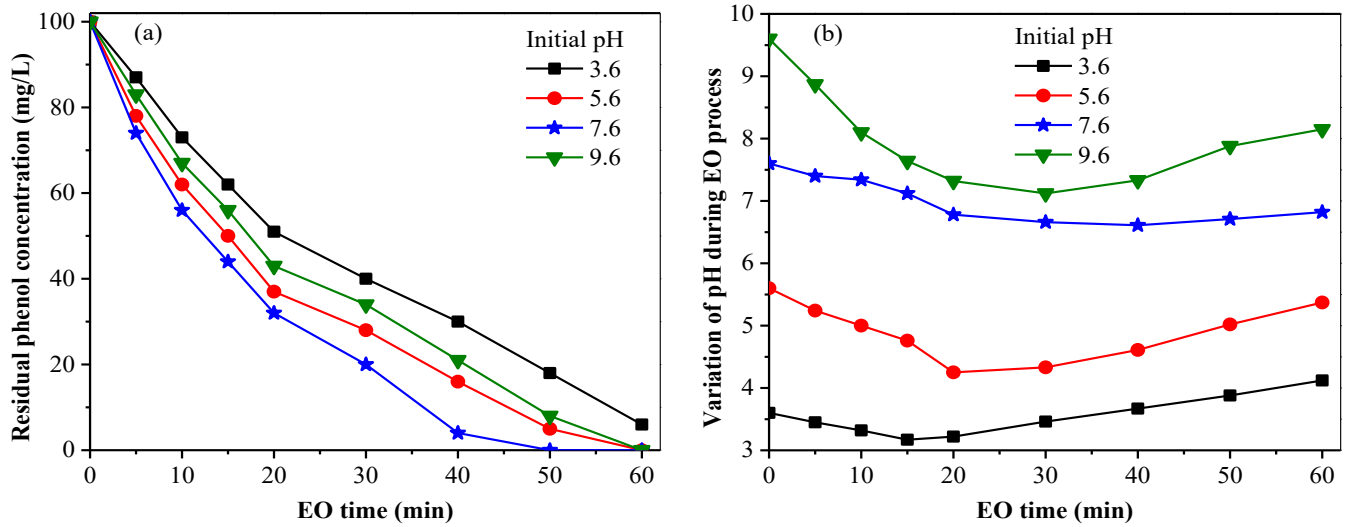

Figure 4. *Impact of initial pH on (a) phenol removal and (b) pH variation during the process.*

As can be seen from (Figure. 5), under optimum conditions (anode = BDD, j = 200 A/m^2, C_i = 100 mg/L, and SE_c = 4 gNaCl/L) the SEC and total OC were calculated as 16.6 kWh/m^3 (548.8 kWh/kg phenol) and 1.38 \$/m^3 (10.3 \$/kg phenol) for pH of 3.60, and 14.8 kWh/m^3 (489.6 kWh/kg phenol) and 1.22 \$/m^3 (9.18 \$/kg phenol) for pH of 5.60, and 12.7 kWh/m^3 (420.0 kWh/kg phenol) and 0.99 \$/m^3 (7.88 \$/kg phenol) for pH of 7.60, and 15.3 kWh/m^3 (496.8 kWh/kg phenol) and 1.18 \$/m^3 (9.32 \$/kg phenol) for pH of 9.60, respectively. As can be seen from the results, the lowest SEC and total OC were obtained at the optimum pH of the study. This is due to the cost of the chemicals used in the other pH, and also due to the slower removal of phenol, which requires longer time in the rectifier, which leads to high energy consumption, resulting in high operating cost of the study [6].

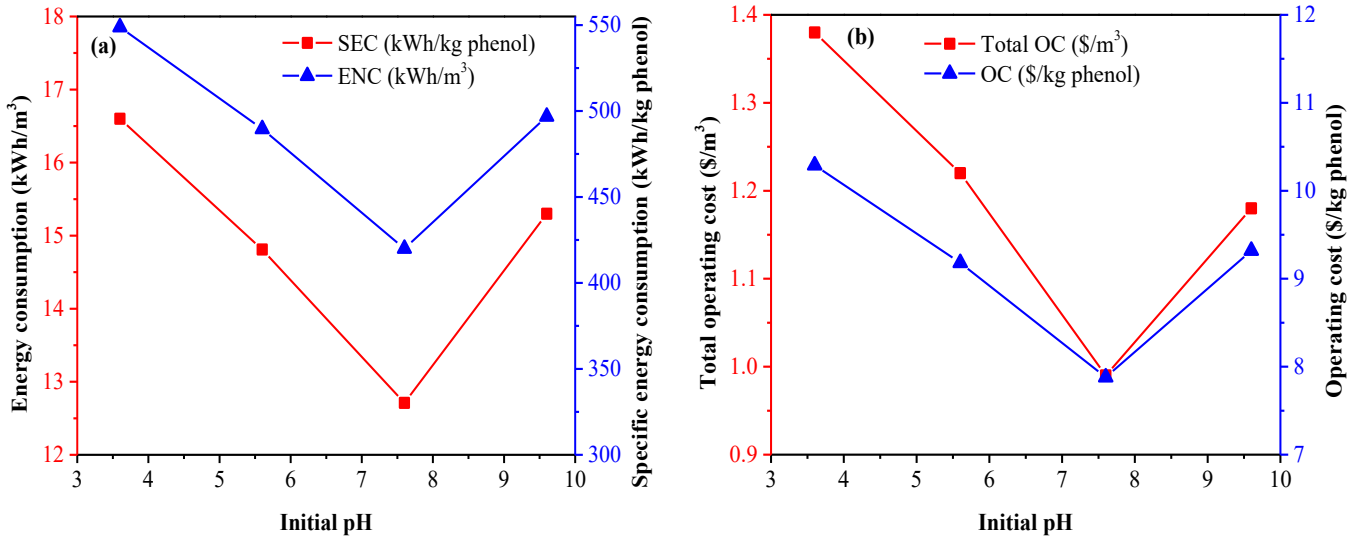

Figure 5. *Impact of initial pH on (a) specific energy consumption and (b) total operating costs.*

3.3. Impact of phenol concentration

The initial phenol concentration is the most important parameter because higher concentrations require longer times for degradation by the EO process [48]. In this study, experiments were performed with different phenol starting concentrations of 100, 200, 400, and 800 mg/L under optimum conditions (anode = BDD, j = 200 A/m^2, C_i = 100 mg/L, and SE_c = 4 g/L). As can be seen from (Figure. 6), the time required for 100% phenol removal was calculated as 50, 120, 160, and 240 min, respectively. As can be seen from the results, higher phenol concentrations require a longer time in the reactor for degradation.

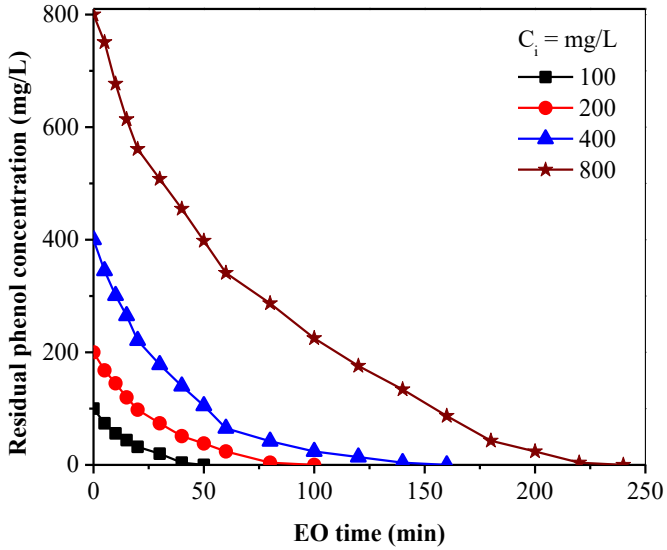

Figure 6. *Impact of reaction time on different phenol concentration removal.*

As can be seen from (Figure. 7), the SEC and total OC required under optimum conditions (anode = BDD, j = 200 A/m^2, SEc = 4 gNaCl/L) for removal of different phenol concentrations were calculated as 12.7 kWh/m^3 (420 kWh/kg phenol) and 0.99 \$/m^3 (7.88 \$/kg phenol) for 100 mg/L of phenol, and 25.41 kWh/m^3 (420 kWh/kg phenol) and 1.78 \$/m^3 (7.88 \$/kg phenol) for 200 mg/L of phenol, and 35.2 kWh/m^3 (291.2 kWh/kg phenol) and 2.38 \$/m^3 (5.46 \$/kg phenol) for 400 mg/L of phenol, and 52.9 kWh/m^3 (218.4 kWh/kg phenol) and 3.48 \$/m^3 (4.10 \$/kg phenol) for 800 mg/L of phenol, respectively. As can be seen from the results, the lowest SEC and total OC were obtained for the low phenol concentration of the study. This is due to the fact that other phenol concentrations require longer time to be reconciled, which leads to high energy consumption, resulting in high operating cost of the study [48].

3.4. Impact of supporting electrolyte concentration

The use of a supported electrolyte increases the conductivity of the solution and the cell voltage decreases, thus leading to lower energy consumption, and lower energy consumption minimizes the total operating cost of the process [49].
In the existing literature, different supported electrolytes were used for phenol oxidation in the EO process, of which NaCl was found to be the most efficient [50,51]. In this study, different concentrations of NaCl were used as supporting electrolytes. Another important reason is that using NaCl as a supported electrolyte, $HOCl^-$ (as seen in Eqs. 10 and 11), is formed rapidly with sodium chloride as a supporting electrolyte and will play an important role in phenol oxidation [50].

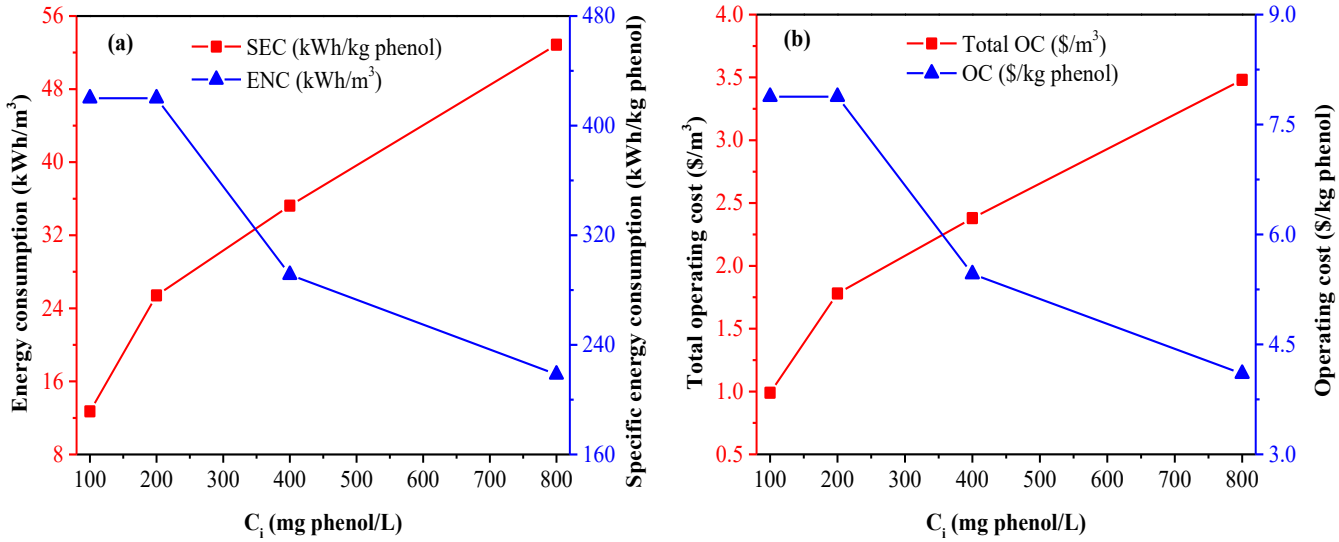

Figure 7. *Impact of initial phenol concentration on (a) specific energy consumption and (b) total operating costs.*

As can be seen from (Figure. 8), under optimum conditions (anode = BDD, j = 200 A/m^2, and initial pH= 7.60) for 2, 4 and 6 gNaCl/L supported electrolytes, the residual phenol concentration for 2 gNaCl/L was 0.001 mg/L after 60 min, however, for 4 and 6 gNaCl/L it was 0.001 mg/L after 50 min, indicating that the increase from 4 to 6 gNaCl/L supported electrolyte has no migratory effect on phenol removal. Similar results were obtained by Zambrano et al. (2019), where treatment with 6 g NaCl/L led to slightly higher removal than treatment with 8 g NaCl/L. As can be seen from the results, the higher concentration of the supported electrolyte, the higher removal of phenol, which may be due to the fact that at low NaCl concentrations, there is a smaller amount of Cl^- ions available to promote the formation of oxidants. However, the electrochemical process using higher electrolyte concentrations quickly reaches alkaline pH, favoring the

production of ClO^- species [51]. These species also promote the slowing down of phenol oxidation. In a study by Zambrano and Min (2019), two different supporting electrolytes (NaCl and Na_2SO_4) were used as Pt/Ti anode for the removal of 100 mg/L phenol at a current density of 96 A/m^2. In this study, it was found that the EO time required for 98.21 ± 3.10% phenol removal was 180 mins when 10 gNaCl/L was used as the supporting electrolyte, but complete phenol removal was achieved after 600 mins when 10 gNa_2SO_4/L was used as the supporting electrolyte. Complete and faster phenol removal was observed when NaCl was used as a supporting electrolyte compared to working with Na_2SO_4 as the electrolyte, probably due to the successful production of active chlorine [52].

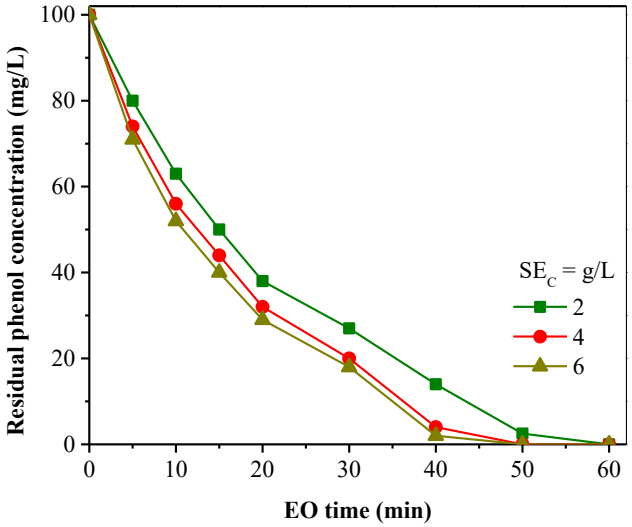

Figure 8. *Impact of supporting electrolyte concentrations on phenol removal efficiency.*

As can be seen from (Figure. 9), the SEC and total OC required under the optimum conditions of the study (anode = BDD, j = 200 A/m^2, pH = 7.60) for different supported electrolyte concentrations were calculated as 18.8 kWh/m^3 (600.0 kWh/kg phenol) and 1.23 $\$/m^3$ (11.25 \$/kg phenol) for 2 gNaCl/L, 12.7 kWh/m^3 (420.0 kWh/kg phenol) and 0.99 $\$/m^3$ (7.88 \$/kg phenol), and 11.6 kWh/m^3 (384.0 kWh/kg phenol) and 1.02 $\$/m^3$ (7.20 \$/kg phenol) for 6 gNaCl/L, respectively. As can be seen from the results, the lowest SEC and total OC were obtained for the high supported electrolyte concentration of the study.

This is because the cell voltage drop leads to low energy consumption, resulting in low operating costs for the study. However, the use of high amounts of supported electrolytes also results in high operating costs, as can be seen in (Figure. 9 b), where the use of 6 gNaCl/L supported electrolyte resulted in higher operating costs than the use of 4 gNaCl/L supported electrolyte. Although it causes the cell voltage to drop, the cost of conduction is higher. This can be explained by the use of excess chemicals.

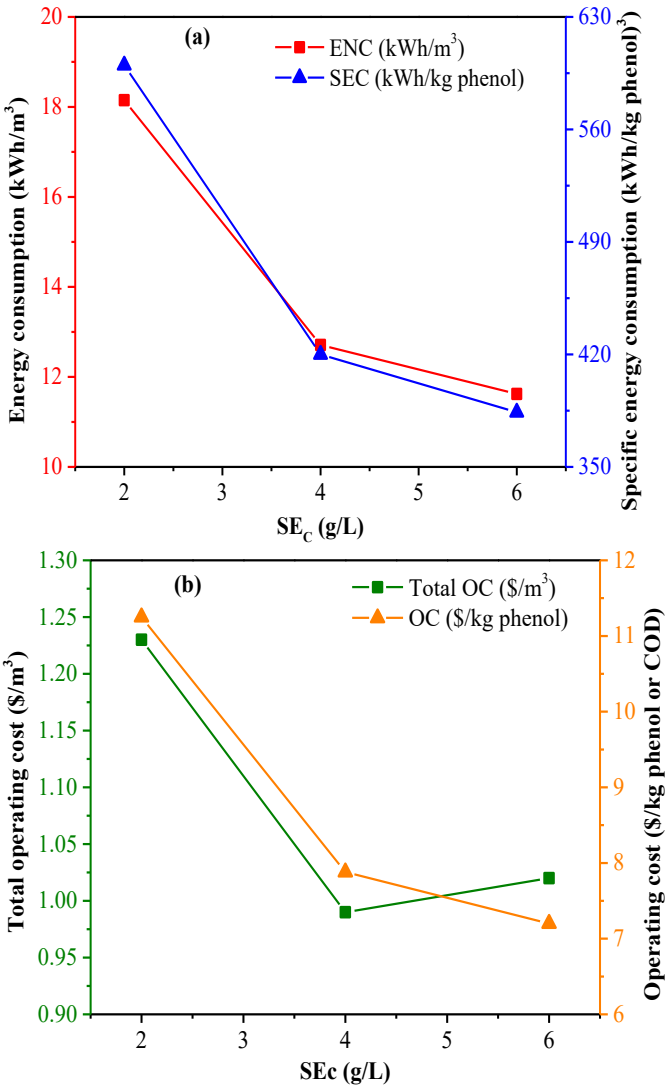

Figure 9. *Impact of supporting electrolyte concentration on (a) specific energy consumption and (b) total operating costs.*

3.5. Comparison of different conventional processes for phenol removal

Different studies on phenol oxidation, energy consumption, and total operating cost analysis have been carried out in the existing literature (as shown in Table. 1), for instance, Gümüş and Akbal (2016) calculated 81.1% for 250 mg/L phenol removal in the classical Fenton process with a starting pH of 10, H_2O_2 concentration of 500 mg/L, and Fe^{2+} dosage of 15 mg/L. However, the OC for this condition was 1.337 \$/kg-phenol. In the same study, Gümüş and Akbal (2016) calculated 93.3% for the electro-Fenton process for 250 mg/L phenol removal with an initial pH of 3, applied current of 0.9 A, and Fe^{2+} dosage of 15.2 mg/L. On the other hand, the OC for this condition was 1.003 \$/kg-phenol [53]. In another study, Amado-Piña et al., (2017) applied sequential ozone/EO process for 100 mg/L phenol removal, the optimum conditions were calculated as 100% phenol oxidation with initial pH

value 7, BDD/SS as anode and cathode, applied current density 600 A/m^2, EO process oxidation time 180 min, wastewater flow rate 0.05 mL/min, SEc concentration 0.1 M Na_2SO_4/L, and O_3 concentration 5 mg/L [54]. In our study, the EO process was applied for phenol oxidation of 100% under optimum conditions (initial concentration of 100 mg phenol/L, initial pH of 7.6, BDD/SS as anode and cathode, applied current density 200 A/m^2, and EO process oxidation time 50 min, SEc of 4 g NaCl/L). However, ENC and total OC for the study were calculated as 12.7 kWh/m^3 (420 kWh/kg phenol) and 0.99 \$/m^3 (7.88 \$/kg phenol), respectively.

Table 1. An overview of literature studies on phenol removal by different conventional processes.

Treatment process	Optimum values	R_e (%)	Energy consumption and total OC	References
Fenton	pH = 10, C_i = 250 mg/L, H_2O_2 concentration = 500 mg/L, Fe^{2+} dose = 15 mg/L	81.1	OC = 1.337 \$/kg-phenol	[53]
Electro-Fenton	pH = 3, anode/cathode = Fe/Fe, C_i = 250 mg/L, j = 0.9 A, t = 5 min, Fe^{2+} dose = 15.2 mg/L, SEc = 1 g Na_2SO_4/L	93.3	OC = 1.003 \$/kg-phenol	
Electro-Fenton	pH = 3, anode/cathode = nickel/carbon felt, C_i = 100 mg/L, j = 0.9 A, t = 90 min, Fe^{2+} dose = 20 mg/L	95.2	-	[55]
O_3-EO	pH = 7, anode/cathode = BDD/SS, C_i = 100 mg/L, j = 600 A/m^2, t = 180 min, Q = 0.05 mL/min, O_3 = 5 mg/L, SEc = 0.1 M Na_2SO_4/L	100	-	[54]
EO	pH = 3.4, anode/cathode = graphite /graphite, C_i = 500 mg/L, j = 150 A/m^2, t = 120 min	59.4	C_{energy} = 111 kWh/kg-phenol	[56]
EO	pH = 3.4, anode/cathode = Ti/RuO_2/SS, C_i = 323 mg/L, j = 1190 A/m^2, t = 180 min, SEc = 10 g NaCl/L	97.2	C_{energy} = 162 kWh/m^3	[57]
EO	pH = 5, anode/cathode = Pt/Ti, C_i = 90 mg/L, j = 91 A/m^2, t = 1440 min	99.9	C_{energy} = 14 kWh/m^3	[58]
EO	pH = 7.6, anode/cathode = BDD/SS, C_i = 100 mg/L, j = 200 A/m^2, t = 50 min, SEc = 4 g NaCl/L	100	C_{energy} = 12.7 kWh/m^3 (420 kWh/kg-phenol), OC = 0.99 \$/m^3 (7.88 \$/kg-phenol)	**Present work**

4. Conclusion

In this study, the removal of phenol from an aqueous solution using a BDD anode in the EO process was investigated. Different current densities, initial pH, phenol concentrations, and supported electrolyte concentrations were investigated. As the current density increased, the rate of phenol oxidation also increased. The most efficient results were obtained at a current density of 200 A/m^2 and the initial pH of the aqueous solution (7.60). In this study, although the supported electrolyte helped to reduce the cell voltage in the study, it was found that the removal efficiency did not have a high effect when using the supported electrolyte at a concentration higher than 4 g NaCl/L. Under these conditions, 100 mg/L phenol oxidation was 100% in 50 min. The SEC and total OC required for the removal of 100 mg/L phenol concentration under optimum conditions (anode = BDD, j = 200 A/m^2, pH = 7.60, SE_c = 4 gNaCl/L) were calculated as 12.7 kWh/m^3 (420 kWh/kg phenol) and 0.99 \$/m^3 (7.88 \$/kg phenol), respectively. The findings of the study show that the EO process using a BDD anode is a very efficient choice for phenol oxidation from an aqueous solution. The use of EO methods offers several advantages, such as user-friendly equipment, reduced treatment time, and economical costs of phenol oxidation.

References

[1] M. Motamedi, L. Yerushalmi, F. Haghighat, and Z. Chen, "Recent developments in photocatalysis of industrial effluents : A review and example of phenolic compounds degradation," *Chemosphere*, vol. 296, p. 133688, Jun. 2022, doi: 10.1016/j.chemosphere.2022.133688.

[2] M. Barik, C. P. Das, A. Kumar Verma, S. Sahoo, and N. K. Sahoo, "Metabolic profiling of phenol biodegradation by an indigenous Rhodococcus pyridinivorans strain PDB9T N-1 isolated from paper pulp wastewater," *Int Biodeterior Biodegradation*, vol. 158, p. 105168, Mar. 2021, doi: 10.1016/j.ibiod.2020.105168.

[3] A. Faggiano *et al.*, "Photo-Fenton like process as polishing step of biologically co-treated olive mill

wastewater for phenols removal," *Sep Purif Technol*, vol. 305, p. 122525, Jan. 2023, doi: 10.1016/j.seppur.2022.122525.

[4] S. T. Kadhum, G. Y. Alkindi, and T. M. Albayati, "Determination of chemical oxygen demand for phenolic compounds from oil refinery wastewater implementing different methods," *Desalination Water Treat*, vol. 231, pp. 44–53, Aug. 2021, doi: 10.5004/dwt.2021.27443.

[5] A. Almasi, M. Mahmoudi, M. Mohammadi, A. Dargahi, and H. Biglari, "Optimizing biological treatment of petroleum industry wastewater in a facultative stabilization pond for simultaneous removal of carbon and phenol," *Toxin Rev*, vol. 40, no. 2, pp. 189–197, Apr. 2021, doi: 10.1080/15569543.2019.1573433.

[6] C. Iskurt, R. Keyikoglu, M. Kobya, and A. Khataee, "Treatment of coking wastewater by aeration assisted electrochemical oxidation process at controlled and uncontrolled initial pH conditions," *Sep Purif Technol*, vol. 248, p. 117043, Oct. 2020, doi: 10.1016/j.seppur.2020.117043.

[7] L. Ayed, I. El Ksibi, A. Charef, and R. El Mzoughi, "Hybrid coagulation-flocculation and anaerobic-aerobic biological treatment for industrial textile wastewater: pilot case study," *The Journal of The Textile Institute*, vol. 112, no. 2, pp. 200–206, Feb. 2021, doi: 10.1080/00405000.2020.1731273.

[8] M. Malakootian and M. R. Heidari, "Removal of phenol from steel wastewater by combined electrocoagulation with photo-Fenton," *Water Science and Technology*, vol. 78, no. 6, pp. 1260–1267, Nov. 2018, doi: 10.2166/wst.2018.376.

[9] W. Ma *et al.*, "Enhanced degradation of phenolic compounds in coal gasification wastewater by a novel integration of micro-electrolysis with biological reactor (MEBR) under the micro-oxygen condition," *Bioresour Technol*, vol. 251, pp. 303–310, Mar. 2018, doi: 10.1016/j.biortech.2017.12.042.

[10] N. A. Akhtar, K. K. Kyzy, M. Kobya, and E. Gengec, "Operating cost and treatment analysis of cattle slaughterhouse wastewater by coagulation-flocculation and electrooxidation processes," *Clean Technol Environ Policy*, Dec. 2024, doi: 10.1007/s10098-024-03084-7.

[11] L. Zhao *et al.*, "Biochar as simultaneous shelter, adsorbent, pH buffer, and substrate of Pseudomonas citronellolis to promote biodegradation of high concentrations of phenol in wastewater," *Water Res*, vol. 172, p. 115494, Apr. 2020, doi: 10.1016/j.watres.2020.115494.

[12] USEPA, *U.S. Environmental Protection Agency (EPA). Water Quality Standards Handbook.* Washington, DC: EPA Office of Water, Office of Science and Technology, 2024.

[13] M. Y. Abduh, D. Nofitasari, A. Rahmawati, A. Y. Eryanti, and M. Rosmiati, "Effects of brewing conditions on total phenolic content, antioxidant activity and sensory properties of cascara," *Food Chemistry Advances*, vol. 2, p. 100183, Oct. 2023, doi: 10.1016/j.focha.2023.100183.

[14] M. Besharati Vineh, A. A. Saboury, A. A. Poostchi, A. M. Rashidi, and K. Parivar, "Stability and activity improvement of horseradish peroxidase by covalent immobilization on functionalized reduced graphene oxide and biodegradation of high phenol concentration," *Int J Biol Macromol*, vol. 106, pp. 1314–1322, Jan. 2018, doi: 10.1016/j.ijbiomac.2017.08.133.

[15] K. Grace Pavithra, P. Sundar Rajan, J. Arun, K. Brindhadevi, Q. Hoang Le, and A. Pugazhendhi, "A review on recent advancements in extraction, removal and recovery of phenols from phenolic wastewater: Challenges and future outlook," *Environ Res*, vol. 237, p. 117005, Nov. 2023, doi: 10.1016/j.envres.2023.117005.

[16] P. Bhatt *et al.*, "Nanobioremediation: A sustainable approach for the removal of toxic pollutants from the environment," *J Hazard Mater*, vol. 427, p. 128033, Apr. 2022, doi: 10.1016/j.jhazmat.2021.128033.

[17] N. Panigrahy, A. Priyadarshini, M. M. Sahoo, A. K. Verma, A. Daverey, and N. K. Sahoo, "A comprehensive review on eco-toxicity and biodegradation of phenolics: Recent progress and future outlook," *Environ Technol Innov*, vol. 27, p. 102423, Aug. 2022, doi: 10.1016/j.eti.2022.102423.

[18] R. Tundis, C. Conidi, M. R. Loizzo, V. Sicari, R. Romeo, and A. Cassano, "Concentration of Bioactive Phenolic Compounds in Olive Mill Wastewater by Direct Contact Membrane Distillation," *Molecules*, vol. 26, no. 6, p. 1808, Mar. 2021, doi: 10.3390/molecules26061808.

[19] M. Jain *et al.*, "Modelling and statistical interpretation of phenol adsorption behaviour of 3-Dimensional hybrid aerogel of waste-derived carbon nanotubes and graphene oxide," *Chemical Engineering Journal*, vol. 490, p. 151351, Jun. 2024, doi: 10.1016/j.cej.2024.151351.

[20] Y. Dehmani *et al.*, "Adsorption removal of phenol by oak wood charcoal activated carbon," *Biomass Convers Biorefin*, vol. 14, no. 6, pp. 8015–8027, Mar. 2024, doi: 10.1007/s13399-022-03036-5.

[21] J. Sun *et al.*, "Oxidative degradation of phenols and substituted phenols in the water and atmosphere: a review," *Adv Compos Hybrid Mater*, vol. 5, no. 2, pp. 627–640, Jun. 2022, doi: 10.1007/s42114-022-00435-0.

[22] L. Y. Jun *et al.*, "An overview of immobilized enzyme technologies for dye and phenolic removal from

wastewater," *J Environ Chem Eng*, vol. 7, no. 2, p. 102961, Apr. 2019, doi: 10.1016/j.jece.2019.102961.

[23] M. Ağtaş, T. Ormancı-Acar, B. Keskin, T. Türken, and İ. Koyuncu, "Nanofiltration membranes for salt and dye filtration: effect of membrane properties on performances," *Water Science and Technology*, vol. 83, no. 9, pp. 2146–2159, May 2021, doi: 10.2166/wst.2021.125.

[24] Y.-F. Mi, G. Xu, Y.-S. Guo, B. Wu, and Q.-F. An, "Development of antifouling nanofiltration membrane with zwitterionic functionalized monomer for efficient dye/salt selective separation," *J Memb Sci*, vol. 601, p. 117795, Mar. 2020, doi: 10.1016/j.memsci.2019.117795.

[25] T. Đuričić, H. Prosen, A. Kravos, S. Mićin, G. Kalčíková, and B. N. Malinović, "Electrooxidation of Phenol on Boron-doped Diamond and Mixed-metal Oxide Anodes: Process Evaluation, Transformation By-products, and Ecotoxicity," *J Electrochem Soc*, vol. 170, no. 2, p. 023503, Feb. 2023, doi: 10.1149/1945-7111/acb84b.

[26] X. Zhang *et al.*, "Degradation of phenol by metal-free electro-fenton using a carbonyl-modified activated carbon cathode: Promoting simultaneous H2O2 generation and activation," *Environ Res*, vol. 263, p. 120020, Dec. 2024, doi: 10.1016/j.envres.2024.120020.

[27] G. Yadav and Md. Ahmaruzzaman, "New generation advanced nanomaterials for photocatalytic abatement of phenolic compounds," *Chemosphere*, vol. 304, p. 135297, Oct. 2022, doi: 10.1016/j.chemosphere.2022.135297.

[28] K. A. Mohamad Said, A. F. Ismail, Z. Abdul Karim, M. S. Abdullah, and A. Hafeez, "A review of technologies for the phenolic compounds recovery and phenol removal from wastewater," *Process Safety and Environmental Protection*, vol. 151, pp. 257–289, Jul. 2021, doi: 10.1016/j.psep.2021.05.015.

[29] J. Tao *et al.*, "Multi-step separation of different chemical groups from the heavy fraction in biomass fast pyrolysis oil," *Fuel Processing Technology*, vol. 202, p. 106366, Jun. 2020, doi: 10.1016/j.fuproc.2020.106366.

[30] W. Raza, J. Lee, N. Raza, Y. Luo, K.-H. Kim, and J. Yang, "Removal of phenolic compounds from industrial waste water based on membrane-based technologies," *Journal of Industrial and Engineering Chemistry*, vol. 71, pp. 1–18, Mar. 2019, doi: 10.1016/j.jiec.2018.11.024.

[31] N. A. Akhtar and M. Kobya, "Treatment of cattle slaughterhouse wastewater by sequential coagulation-flocculation/electrooxidation process," *MANAS Journal of Engineering*, vol. 12, no. 1, pp. 116–128, Jun. 2024, doi: 10.51354/mjen.1407291.

[32] A. Turan, R. Keyikoglu, M. Kobya, and A. Khataee, "Degradation of thiocyanate by electrochemical oxidation process in coke oven wastewater: Role of operative parameters and mechanistic study," *Chemosphere*, vol. 255, p. 127014, Sep. 2020, doi: 10.1016/j.chemosphere.2020.127014.

[33] O. T. Can, E. Gengec, and M. Kobya, "TOC and COD removal from instant coffee and coffee products production wastewater by chemical coagulation assisted electrooxidation," *Journal of Water Process Engineering*, vol. 28, pp. 28–35, Apr. 2019, doi: 10.1016/j.jwpe.2019.01.002.

[34] Z. Movaffagh, A. Khataee, A. Jamal Sisi, Z. Jalali, M. Zarei, and M. Kobya, "Mixed metal oxide (Ru, Ir, Sn) electrodes in the anodic activation of peroxydisulfate for a sustainable degradation of rifampicin," *Journal of Industrial and Engineering Chemistry*, vol. 138, pp. 575–585, Oct. 2024, doi: 10.1016/j.jiec.2024.04.035.

[35] M. Moradi, Y. Vasseghian, A. Khataee, M. Kobya, H. Arabzade, and E.-N. Dragoi, "Service life and stability of electrodes applied in electrochemical advanced oxidation processes: A comprehensive review," *Journal of Industrial and Engineering Chemistry*, vol. 87, pp. 18–39, Jul. 2020, doi: 10.1016/j.jiec.2020.03.038.

[36] Z. Ukundimana, P. I. Omwene, E. Gengec, O. T. Can, and M. Kobya, "Electrooxidation as post treatment of ultrafiltration effluent in a landfill leachate MBR treatment plant: Effects of BDD, Pt and DSA anode types," *Electrochim Acta*, vol. 286, pp. 252–263, Oct. 2018, doi: 10.1016/j.electacta.2018.08.019.

[37] N. A. Akhtar, E. Gengec, and M. Kobya, "Treatment of Slaughterhouse Plant Wastewater by Sequential Chemical Coagulation-Continuous Flow Electrooxidation Process," *J Electrochem Soc*, vol. 171, no. 7, p. 073505, Jul. 2024, doi: 10.1149/1945-7111/ad6192.

[38] APHA, *Standard Methods for the Examination of Water and Wastewater*, 24th ed. Washington DC: American Public Health Association, American Water Works Association, Water Environment Federation., 2023.

[39] N. Akhtar and M. Kobya, "Efficient degradation of industrial slaughterhouse wastewater by electrooxidation process: impact of DSA anode materials on oxidation and operating costs," *Environ Technol*, Mar. 2025.

[40] D. Amado-Piña *et al.*, "Synergic effect of ozonation and electrochemical methods on oxidation and toxicity reduction: Phenol degradation," *Fuel*, vol. 198, pp. 82–90, Jun. 2017, doi: 10.1016/j.fuel.2016.10.117.

[41] Y. Gong *et al.*, "Novel graphite-based boron-doped diamond coated electrodes with refractory metal interlayer for high-efficient electrochemical oxidation degradation of phenol," *Sep Purif Technol*, vol. 355, p. 129550, Mar. 2025, doi: 10.1016/j.seppur.2024.129550.

[42] Y. Zhu, H. Wang, Q. Jiang, A. T. Kuvarega, and J. Li, "Hexagonal boron nitride-doped carbon membrane as anode for the enhanced adsorption and electrochemical oxidation of phenol," *J Environ Chem Eng*, vol. 12, no. 3, p. 113002, Jun. 2024, doi: 10.1016/j.jece.2024.113002.

[43] N. A. Akhtar, M. Kobya, and A. Khataee, "Removal of Cr(VI) by continuous flow electrocoagulation reactor at controlled and uncontrolled initial pH conditions," *Chemical Engineering Research and Design*, vol. 214, pp. 403–414, Feb. 2025, doi: 10.1016/j.cherd.2025.01.015.

[44] B. G. Savić *et al.*, "Electrochemical oxidation of a complex mixture of phenolic compounds in the base media using PbO2-GNRs anodes," *Appl Surf Sci*, vol. 529, p. 147120, Nov. 2020, doi: 10.1016/j.apsusc.2020.147120.

[45] E. M. S. Oliveira *et al.*, "Performance of (in)active anodic materials for the electrooxidation of phenolic wastewaters from cashew-nut processing industry," *Chemosphere*, vol. 201, pp. 740–748, Jun. 2018, doi: 10.1016/j.chemosphere.2018.02.037.

[46] X. Liu, S. You, F. Ma, and H. Zhou, "Characterization of electrode fouling during electrochemical oxidation of phenolic pollutant," *Front Environ Sci Eng*, vol. 15, no. 4, p. 53, Aug. 2021, doi: 10.1007/s11783-020-1345-7.

[47] P. Alfonso-Muniozguren, S. Cotillas, R. A. R. Boaventura, F. C. Moreira, J. Lee, and V. J. P. Vilar, "Single and combined electrochemical oxidation driven processes for the treatment of slaughterhouse wastewater," *J Clean Prod*, vol. 270, p. 121858, Oct. 2020, doi: 10.1016/j.jclepro.2020.121858.

[48] N. D. Mu'azu, M. Al-Yahya, A. M. Al-Haj-Ali, and I. M. Abdel-Magid, "Specific energy consumption reduction during pulsed electrochemical oxidation of phenol using graphite electrodes," *J Environ Chem Eng*, vol. 4, no. 2, pp. 2477–2486, Jun. 2016, doi: 10.1016/j.jece.2016.04.026.

[49] E. Gengec, "Treatment of highly toxic cardboard plant wastewater by a combination of electrocoagulation and electrooxidation processes," *Ecotoxicol Environ Saf*, vol. 145, pp. 184–192, Nov. 2017, doi: 10.1016/j.ecoenv.2017.07.032.

[50] A. S. Fajardo *et al.*, "Electrochemical oxidation of phenolic wastewaters using a batch-stirred reactor with NaCl electrolyte and Ti/RuO2 anodes," *Journal of Electroanalytical Chemistry*, vol. 785, pp. 180–189, Jan. 2017, doi: 10.1016/j.jelechem.2016.12.033.

[51] T. Đuričić, H. Prosen, A. Kravos, S. Mićin, G. Kalčíková, and B. N. Malinović, "Electrooxidation of Phenol on Boron-doped Diamond and Mixed-metal Oxide Anodes: Process Evaluation, Transformation By-products, and Ecotoxicity," *J Electrochem Soc*, vol. 170, no. 2, p. 023503, Feb. 2023, doi: 10.1149/1945-7111/acb84b.

[52] J. Zambrano and B. Min, "Comparison on efficiency of electrochemical phenol oxidation in two different supporting electrolytes (NaCl and Na2SO4) using Pt/Ti electrode," *Environ Technol Innov*, vol. 15, p. 100382, Aug. 2019, doi: 10.1016/j.eti.2019.100382.

[53] D. Gümüş and F. Akbal, "Comparison of Fenton and electro-Fenton processes for oxidation of phenol," *Process Safety and Environmental Protection*, vol. 103, pp. 252–258, Sep. 2016, doi: 10.1016/j.psep.2016.07.008.

[54] D. Amado-Piña *et al.*, "Synergic effect of ozonation and electrochemical methods on oxidation and toxicity reduction: Phenol degradation," *Fuel*, vol. 198, pp. 82–90, Jun. 2017, doi: 10.1016/j.fuel.2016.10.117.

[55] M. Radwan, M. Gar Alalm, and H. Eletriby, "Optimization and modeling of electro-Fenton process for treatment of phenolic wastewater using nickel and sacrificial stainless steel anodes," *Journal of Water Process Engineering*, vol. 22, pp. 155–162, Apr. 2018, doi: 10.1016/j.jwpe.2018.02.003.

[56] N. D. Mu'azu, M. Al-Yahya, A. M. Al-Haj-Ali, and I. M. Abdel-Magid, "Specific energy consumption reduction during pulsed electrochemical oxidation of phenol using graphite electrodes," *J Environ Chem Eng*, vol. 4, no. 2, pp. 2477–2486, Jun. 2016, doi: 10.1016/j.jece.2016.04.026.

[57] A. S. Fajardo *et al.*, "Electrochemical oxidation of phenolic wastewaters using a batch-stirred reactor with NaCl electrolyte and Ti/RuO2 anodes," *Journal of Electroanalytical Chemistry*, vol. 785, pp. 180–189, Jan. 2017, doi: 10.1016/j.jelechem.2016.12.033.

[58] J. Zambrano, H. Park, and B. Min, "Enhancing electrochemical degradation of phenol at optimum pH condition with a Pt/Ti anode electrode," *Environ Technol*, vol. 41, no. 24, pp. 3248–3259, Oct. 2020, doi: 10.1080/09593330.2019.1649468.

MANAS Journal of Engineering
ISSN 1694-7398 | e-ISSN 1694-7398

Volume 13, Issue 1, (2025) Pages 64-78
https://doi.org/10.51354/mjen.1699996

A Numerical Analysis of the Effect of Corrugated Surface Profile on Heat Transfer in Turbulent Flow Through a Rectangular Mini-Channel

Muhammet Kaan Yeşilyurt[1,2,*], Mansur Mustafaoğlu[1,2]

[1] Deparment of Mechanical Engineering, Faculty of Engineering, Atatürk University, Erzurum, Türkiye, kaan.yesilyurt@atauni.edu.tr ORCID: 0000-0002-7207-1743

[2] Deparment of Mechanical Engineering, Faculty of Engineering, Atatürk University, Erzurum, Türkiye, mansour@atauni.edu.tr ORCID: 0000-0003-2976-0196

ABSTRACT

Mini channels have the potential to provide high heat transfer efficiency in a variety of applications. However, due to their small size, higher pressure drop occurs. Therefore, a balance needs to be established between heat transfer improvement and pumping power requirements. In the present study the effect of corrugated surface profile on heat transfer and flow characteristics were numerically investigated under turbulent flow conditions in a rectangular cross-section mini-channel through Computational Fluid Dynamics (CFD) simulations using the ANSYS Fluent 2019 software. The study employed. The mini-channel had a total length of 26 mm, with the left and right side walls consisting of 3 mm straight sections at the inlet and outlet, and a 19 mm corrugated section in the middle while the top and bottom sides are straight end to end. Optimum values for heat transfer and pressure drop were investigated through CFD analyses by varying the profile of the corrugated section of the side walls between 0.5, 1 and 2 mm for air and water fluids. It was determined that the pressure drop for air varied between approximately 850-1250 Pa whereas for water it varied between 1300-1900 Pa. The Nusselt number increased by 3.27% for air, from 12.2 to 12.6, and for water, it increased by 2.17%, from 13.36 to 13.65. Results showed that the corrugated surface improved heat transfer by increasing turbulence and mixing with the flow, but also significantly increases the pressure drop.

ARTICLE INFO

Research article

Received: 15/05/2025
Accepted: 17/06/2025

Keywords:
Mini-Channel,
Heat Transfer,
Pressure Drop,
Corrugation

**Corresponding author*

1. Introduction

In various systems, such as heat exchangers, nuclear reactors, and distillation units, mass and heat transfer occur along the walls of ducts where fluids flow. The fluid passage medium can be influenced by the cross-section of the channel as the volumetric flow passes over it, affecting the transfer processes. The utilization of smaller-sized channels, such as mini- and micro-channels, presents a significant opportunity to enhance heat transfer efficiency in various applications [1]. Mini-channels are channels that are larger than micro-channels, but with a hydraulic diameter typically between 0.1 mm and 6mm. They offer a balance between the high efficiency of micro-channels and the easier manufacturing of larger channels. Mini-channels play a crucial role in enhancing heat transfer efficiency in various applications. While smaller channels offer improved heat transfer efficiency, they also result in a higher pressure drop per unit length. It is therefore necessary to keep a balance between heat transfer enhancement and pumping power requirements [2].

In automotive applications, as a result of miniaturization, the size of radiators and evaporators has become crucial to achieving an optimal balance between the pumping power requirements, heat transfer efficiency, and cleaning of the entire system. Specifically, the dimensions of these components are often reduced to the millimeter scale to maximize cooling performance while minimizing energy consumption. Similarly, in building air conditioning applications, advancements in thermal management systems now allow for the integration of electronic and microelectronic cooling solutions with centralized HVAC systems. Such integrations have been particularly important

for the equipments where a stable thermal environment is critical for operational efficiency, such as server rooms [3]. These developments and associated integrations increase the demand for compact and efficient cooling technologies across various applications.

Increased power density along with minituarization of electronic devices brought on the need for an effective thermal management in electronic components as high temperatures have great negative impact on performance and life of electronic devices [4]. Therefore, compact cooling systems, especially those made using micro and mini channels, have become an important research topic since they offer higher heat transfer efficiency compared to traditional air-cooled methods [5].

Mini channels typically have hydraulic diameters ranging from 1 to 10 mm and provide effective heat transfer thanks to their high surface-to-volume ratio [6]. In this study, a mini channel array with straight and reversely arranged semicircular bends was investigated as a heat sink for cooling electronic components. The reason for choosing this particular configuration is that the vortices formed with the change of direction of the flow increase the heat transfer coefficient and provide a more homogeneous temperature distribution.

Many studies have been conducted in the literature on the heat transfer of mini channels with similar structures. For example, Kandlikarand Grande [7], in their studies examining the effect of mini channel geometry on heat transfer, showed that the flow regime in micro-scale channels exhibits different characteristics compared to traditional channels. In addition, Leeand Garimella [8] presented a detailed analysis of the flow and heat transfer characteristics in cooling systems using mini channel arrays.

Harley et al. [9] measured the friction factor (C_f) in multi-sided and square-section micro-channels. Experimentally, they found that C_f was 49 for square channels and 512 for multilateral channels. Pengand Peterson [10] experimentally revealed that the transition to turbulent flow starts in the range of Reynolds 200–700, and the full turbulent transition is reached at Reynolds 400–1500. They also observed that Reynolds decreases as the microchannel becomes smaller. Pengand Wang [11] concluded that this feature is due to the thermo-physical properties of the fluid due to the high heat flux in the micro-channels.

Shahand London [12] demonstrated that equilateral triangular cross-section micro-channels can lead to a 17% reduction in the friction factor for developed laminar flow at constant heat flux, despite a 27% penalty in the Nusselt number. This finding highlights the trade-off between friction factor reduction and Nusselt number in micro-channels with specific geometries. Additionally, Steinkeand Kandlikar [13] discussed the ongoing research on the validity of friction factor theory for microchannel flows based on conventional-sized passages. This suggests that there is still active exploration and debate regarding the applicability of traditional friction factor theories to microscale flows. Moreover, research by Wang et al. [14] indicated that adding ribs to micro-channels can enhance heat transfer performance but inevitably increases the friction factor. The study found that the friction factor increased significantly for micro-channels with rectangular, triangular, and semicircular ribbed configurations compared to smooth micro-channels. This emphasizes the impact of channel modifications on friction factor values.

Comparison of numerical calculations of flow in trapezoidal channels for flows with Reynolds numbers below 600 showed a good match between numerical and experimental results, although inflow effects can be seen in very short channels [15].

Heat transfer research on mini-channels has received significant interest due to the potential for enhanced heat transfer efficiency in compact systems. Mini-channels improve heat transfer in two primary ways: by increasing the heat transfer coefficient through their small dimensions and reducing resistance on airflow due to their flat orientation [16]. Research has explored various aspects of mini-channel heat transfer, including the impact of different geometrical designs on heat transfer rates, with a particular emphasis on the use of different fluids to improve heat transfer efficiency [17]. Additionally, investigations into the effects of roughness on laminar heat transfer in additive manufactured mini-channels have shown that roughness can indeed enhance heat transfer performance [18].

Alterations to channel walls, such as the introduction of ribs or wavy patterns, can significantly influence heat transfer processes. Research has shown that the integration of ribbed surfaces in heat exchangers has been widely adopted to enhance convective heat transfer and overall thermal efficiency [19]. The addition of ribs can also lead to a substantial increase in the friction factor [20]. Furthermore, ongoing research explores the validity of traditional friction factor theories for mini- and micro-channel flows, highlighting the intricate relationship between channel geometry, modifications, and their impact on friction factors and heat transfer performance in diverse fluid systems. On the other hand, the incorporation of porous inserts in channels can significantly enhance convective heat transfer while moderately increasing flow resistance [21]. The application of nanofluids and unique channel geometries, such as triangular wavy channels, under pulsating flow conditions has been investigated to understand their impact on heat transfer and pressure drop characteristics [22].

Alhamid et al. [23] conducted a study on the effect of turbulators on thermal flow and heat performance in a 3D pipe, exploring different concavity diameters with corrugation and twisted tape configurations. This research aimed to improve heat transfer efficiency through innovative design modifications. Similarly, Al-Obaidi et al. [24] studied flow

field and heat transfer enhancement using a combination of corrugated tubes with a twisted tape within a 3D circular tube based on different dimple configurations.

Mezaache et al. [25] investigated mixed convection and entropy production of nanofluid flow in a corrugated channel using a two-phase mixture model, exploring corrugation profiles with trapezoidal, sinusoidal, and triangular shapes. Additionally, Haj Maideenand Somu [26] analyzed the design and performance of a double-pipe heat exchanger with new arrangements of corrugated tubes using honeycomb arrangements, focusing on convective heat transfer and friction factor of Al_2O_3-water nanofluid in helically corrugated tubes.

Choudharyand Ray [27] conducted a numerical study on combined convection heat transfer flow in a porous corrugated enclosure, investigating the influence of the Grashof number on heat transfer efficiency. Sruthi et al. [28] performed a comparative analysis of the corrugation effect on the thermohydraulic performance of double-pipe heat exchangers, focusing on the effectiveness of helically corrugated tubes in enhancing convective heat transfer.

Songand Wang [29] have emphasized the importance of secondary flows to enhance heat transfer performance while minimizing pumping power requirements and thermal resistance. Additionally, specialized channel designs, such as corrugated channels, has been shown to significantly enhance heat transfer.

Microelectronic equipment with various applications, such as personal computers, servers, general diodes, etc., has been proposed to increase the intensity of the transmitted heat flow to higher values, thus increasing the once very large and unattainable figure of 200 watts per square centimeter of transmitted heat, has now become a normal or even small amount. As a matter of fact, heat transfer rate is over 600 watts per square centimeter today. In addition, the temperature difference required to carry out the heat transfer process is also decreasing by a few degrees Celsius. These high amounts of heat transfer require that the dimensions of the micro-channels be greatly reduced so that they can be well matched to the components of the cooling system and thus improve the movement of the fluid from the heat source [30].

In this research, therefore, a 26-mm-long mini-channel was designed with a 3 mm straight upstream part, a 20-mm central part with corrugated side walls, and another 3mm straight downstream part. These channels are capable of being coupled with each other, by being putting together one straight and one reversed, to form wider arrays of mini-channels to function as a heat sink as shown in Figure 1.

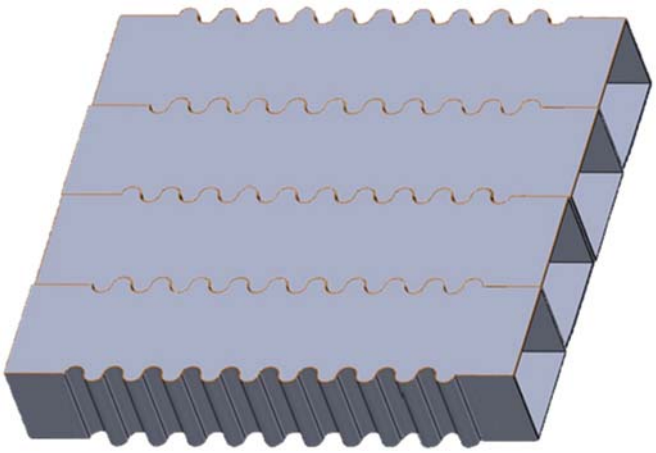

Figure 1. *Heat sink consisting of array or mini-channels*

In this respect, the effect of a channel geometry on the flow characteristics and cooling performance was numerically investigated for certain input parameters and boundary conditions. While previous research has explored the influence of various geometric modifications on thermal performance, the channel configuration is unique in terms of wall structure, dimensions, arrangement, and profile. Computational Fluid Dynamics (CFD) simulations were conducted using ANSYS Fluent software to evaluate the impact of these modifications on pressure drop, Nusselt number, and velocity distributions for both air and water as working fluids. The findings contribute to a deeper understanding of how surface profiling can enhance heat transfer efficiency while minimizing energy losses in practical engineering applications.

2. Materials and Methods

2.1. Governing Equations

The integral form of continuity laws is valuable for analyzing the overall behavior of flow fields, while a deeper understanding of flow field specifics necessitates the use of the differential form of fluid motion equations. The governing equations for heat transfer in differential form involve conservation of mass, momentum and energy [31; 32]. First, the assumptions governing the problem are examined:

Turbulent flow.

- The physical properties of the fluids are constant.
- The fluid is incompressible, Newtonian and viscous.
- No-slipwall condition was applied to the computational domain to ensure that the velocity at the solid-fluid interface is zero, in accordance with the standard assumptions of viscous flow [33].
- Constant heat flux to the bottom wall without corrugation.
- No heat loss from external surfaces

Considering the flow in mini-channels of rectangular cross-section, similar to the flow between two parallel planes, the equations governing the flow are simplified to the following forms.

The continuity, momentum and energy equations governing the problem are as follows [34]:

$$\frac{\partial \rho}{\partial t} + \frac{\partial (\rho u_j)}{\partial x_j} = 0 \tag{1}$$

$$\frac{\partial (\rho u_i)}{\partial t} + \frac{\partial (\rho u_j u_i)}{\partial x_j} = -\frac{\partial P}{\partial x_i} + \frac{\partial \tau_{ij}}{\partial x_j} + S_{ui}$$

which can be expanded as:

$$\frac{\partial}{\partial x_j}(\rho u_i u_j) = -\frac{\partial p}{\partial x_i} + \frac{\partial}{\partial x_j}\left[\mu\left(\frac{\partial u_i}{\partial x_j} + \frac{\partial u_j}{\partial x_i} - \frac{2}{3}\delta_{ij}\frac{\partial u_i}{\partial x_j}\right)\right] + \frac{\partial}{\partial x_j}\left(-\rho\overline{u'_i u'_j}\right) \tag{2}$$

The energy equation is:

$$\frac{\partial}{\partial x_i}(\rho u_i c_p T) = \frac{\partial}{\partial x_j}\left[\left(k + \frac{c_p \mu_t}{Pr_t}\right)\frac{\partial T}{\partial x_j} + u_i\left(\mu_{eff}\left(\frac{\partial u_j}{\partial x_i} + \frac{\partial u_i}{\partial x_j}\right) - \frac{2}{3}\mu_{eff}\frac{\partial u_i}{\partial x_j}\delta_{ij}\right)_{eff}\right] \tag{3}$$

This model is well suited for confined flows. It is also suitable for deceleration and sudden separation flows with pressure gradients. The concept of turbulent viscosity is also used in the solution.

$$\frac{\rho \partial k}{\partial t} + \rho u_j k_j = \left(\mu + \frac{\mu_t}{\sigma_t} k_j\right) + G + B - \rho\omega k \tag{4}$$

$$\frac{\rho \partial \omega}{\partial t} + \rho u_j \omega_j = \left(\mu + \frac{\mu_t}{\sigma_t}\omega_j\right) + \frac{c_1 \omega}{k} G + \frac{c_1 \omega}{k}(1 - C_3)B - C_2 \rho \omega^2 \tag{5}$$

2.2. Geometric Model and Boundary Conditions

The geometric model consists of a rectangular mini-channel with corrugated side walls. The geometric parameters of the model used in this study is given in Table 1.

Table 1. Design parameters

Parameter	Notion	Value
Height of the channel	H	5mm
Width of the channel	W	6mm
Corrugation radius	r	0.5mm
Corrugation pitch	λ	1 mm
Upstream section	U	3mm
Corrugated Central section	C	20mm
Downstream section	D	3mm
Pitch-to-width ratio	λ/W	0.200
Pitch-to-length ratio	λ/H	0.167

The drawing of the duct geometry to be analyzed was drawn with the Solidworks program and then these geometries were exported to the ANSYS Workbench program and the mesh structure was created in this program. Since the duct geometry examined in this study is symmetrical, the channel geometries were drawn square and the mesh structure was created accordingly. Figure 3 shows the mesh structure created for the analysis of the channel geometry. A symmetry boundary condition was applied at the mid-plane of the mini-channel to reduce computational cost and ensure an accurate representation of flow characteristics. The symmetric plane divides the geometry into two equal halves along the longitudinal axis, assuming identical flow behavior on both sides of the plane [35].

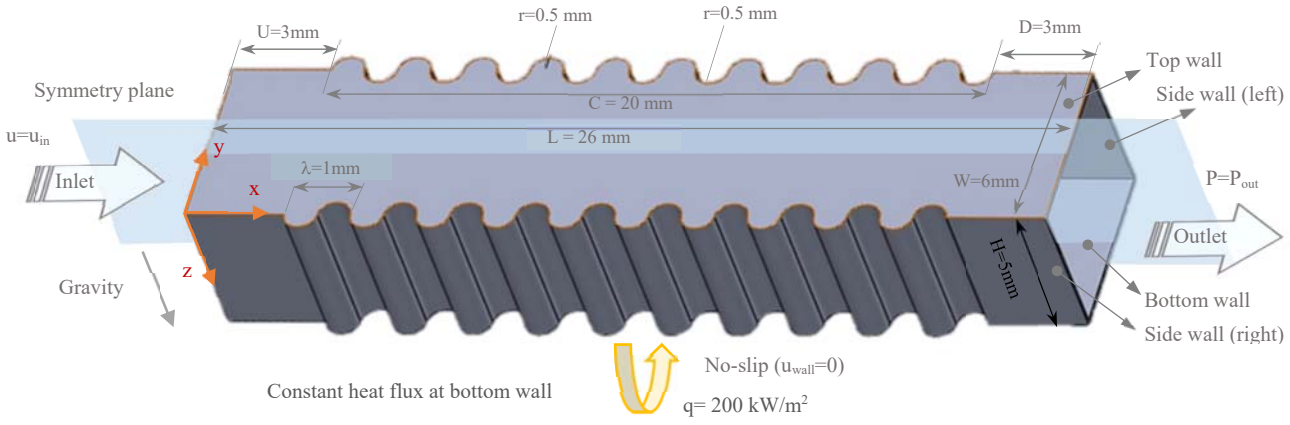

Figure 2. *Channel geometry and boundary conditions*

Figure 2 illustrates the computational domain of the mini-channel, including all relevant boundary conditions and dimensions. The total length of the mini-channel is 26 mm, with a 3 mm straight section at the inlet, a 20 mm corrugated section in the middle, and another 3 mm straight section at the outlet. The corrugated wall introduces periodic disturbances to the flow, enhancing turbulence and heat transfer.

The boundary conditions for the computational domain were adopted as follows:

Inlet boundary conditions	Wall boundary conditions	Outlet boundary conditions
$u = u_{in}$	u = 0	$\frac{\partial \emptyset}{\partial n} = 0,$ $\emptyset = u, v, p, k, \omega$
v = w = 0	v = 0	$\frac{\partial u}{\partial x} = \frac{\partial v}{\partial x} = \frac{\partial w}{\partial x} = 0$
T_{in} = 293.15k	$q = q_{wall}$	$\frac{\partial T_f}{\partial x} = 0$
$k = k_{in}$		$\frac{\partial k}{\partial x} = 0$
$\omega = \omega_{in}$		$\frac{\partial \omega}{\partial x} = 0$

In order to reduce the computational cost and also maintain accuracy, a symmetry boundary condition is applied along the mid-plane of the channel, effectively. The walls are treated as no-slip boundaries, and a constant heat flux of 200 kW/m^2 is imposed on the bottom wall to evaluate heat transfer performance.

2.3. Meshing and Numerical Solution

In this study, tetrahedral mesh elements were used during the creation of the examined duct geometry. The meshed model consisted of about 8 million elements. In order to calculate the distance of the first mesh element from the wall, the value of (y^+) was initially chosen as 5. After finding the distance of the first mesh element from the wall, twenty layers were drawn in the regions close to the wall with a growth rate of 1.2. Thus, in order to calculate and examine the regions close to the wall more precisely, the mesh structure was densified in the regions close to the wall.

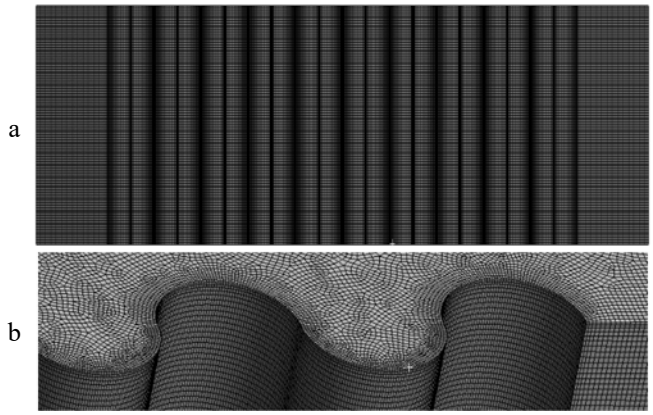

Figure 3. *(a) Meshed model in top view of the right side-wall (b) Close-up view of near wall zone with mesh refinement*

As seen in Figure 4, a grid independence test was conducted to verify that the results were not sensitive to mesh refinement. Five different mesh sizes (coarse, medium, fine, finer, and extra fine) were tested, and the variation in the Nusselt number and maximum temperature was monitored. The deviation was found to be within 1.2%, confirming the adequacy of the selected grid resolution.

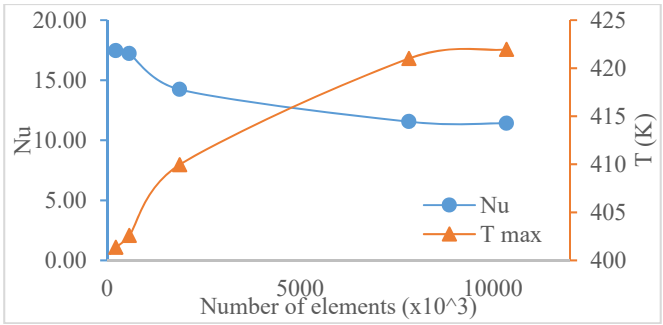

Figure 4. *Grid independence based on variation of Nu and T at different meshes at Re 2300*

The flow near the wall is analyzed according to the general characteristics of our geometry. Since the Reynolds range is small and the flow is limited, the k-ω and k-ε methods give the best response.

The flow structure in the created duct geometry was analyzed using numerical calculation techniques. No data were obtained with any experimental setup. Computational fluid dynamics (CFD) simulations and data were obtained using the ANSYS FLUENT CFD software. The geometries analyzed using the ANSYS FLUENT program were first drawn with the Solidworks CAD software, and then the mesh structures for these geometries were created in the Mesh Structure Creation module of the ANSYS Workbench in accordance with ANSYS FLUENT.

Turbulent fluid motion represents a dynamic flow state characterized by random variations in flow quantities across both space and time, such that a statistically significant mean can hardly be distinguished [36]. Notably, the k-ω turbulence models, developed primarily for aerospace applications involving intricate geometries and phenomena, offer a more straightforward foundation compared to the k-ε turbulence model pioneered by Wilcox. These models present a key advantage in that they allow for the resolution of equations down to the viscous substrate, a capability not always achievable with k-Ɛ models. Among the widely utilized k-ω turbulence models are the standard k–ω turbulence model and the SST k-ω turbulence model, each offering unique insights into turbulent flow behavior. k - ω models are said to be based on much simpler foundations than the k-ε turbulence model [37]. The k-ω turbulence models were originally developed for aerospace applications with very complex geometries and phenomena. An important advantage of k-ω turbulence models over k-ε turbulence models is that the equations can be solved down to the viscous sub layer [38; 39]. The most widely used k-ω turbulence models are the standard k–ω turbulence model and the k-ω SST turbulence model.

The standard k-ω turbulence model incorporates the effects of low Reynolds number and compressibility effects into the calculations. The standard k-ω turbulence model is an empirical model based on the transport equations related to the turbulent kinetic energy (k) and the specific energy dissipation (ω). As the k-ω turbulence model has been evolving over the years, production terms have been added to the transport equations for k and ω that improve the prediction of free shear flows [40].

Due to its proven ability to accurately predict flows involving adverse pressure gradients and flow separation, which are likely to occur in corrugated or duct-like geometries, the k–ω SST model offers superior near-wall treatment by blending the k–ω model near walls with the k–ε model in the free stream, thus providing improved accuracy for wall-bounded turbulent flows. This makes it particularly suitable for the present study where capturing wall effects and pressure-induced separations is critical. The model has also been widely validated in similar studies involving duct flows and heat transfer enhancement with surface irregularities.

Transport equation for turbulence kinetic energy (k);

$$\frac{\partial(\rho k)}{\partial t}+\frac{\partial(\rho k u_i)}{\partial x_i}=\frac{\partial}{\partial x_i}\left[\Gamma_k\frac{\partial k}{\partial x_j}\right]+P_k-Y_k-S_k \quad (6)$$

Transport equation for specific energy dissipation (ω):

$$\frac{\partial(\rho\omega)}{\partial t}+\frac{\partial(\rho\omega u_i)}{\partial x_i}=\frac{\partial}{\partial x_i}\left[\Gamma_\omega\frac{\partial k}{\partial x_j}\right]+P_\omega-Y_\omega-S_\omega \quad (7)$$

In Equations (5) and (6), P_k is the production of turbulence kinetic energy (k), P_ω is the production of specific energy dissipation (ω), Γ_k and Γ_ω are the effective propagation power terms of turbulence energy (k) and specific energy dissipation (ω), respectively. The terms Y_k and Y_ω are the turbulence-induced dissipation of the turbulence kinetic energy (k) and the specific energy (ω), respectively.

In the study a steady-state turbulent flow condition was considered through the mini-channel, time-dependent terms were not included in the final numerical formulation. The solution was obtained using the SIMPLE algorithm for pressure-velocity coupling, and second-order upwind discretization was applied to convective terms to enhance accuracy.

Therefore, the k and ω equations can be re-written for the steady-state solution as follows:

$$\frac{\partial(\rho k u_i)}{\partial x_i}=\frac{\partial}{\partial x_i}\left[\Gamma_k\frac{\partial k}{\partial x_j}\right]+P_k-Y_k-S_k \quad (8)$$

$$\frac{\partial(\rho\omega)}{\partial t}+\frac{\partial(\rho\omega u_i)}{\partial x_i}=\frac{\partial}{\partial x_i}\left[\Gamma_\omega\frac{\partial k}{\partial x_j}\right]+P_\omega-Y_\omega-S_\omega \quad (9)$$

The convergence criteria were set to ensure numerical stability and solution accuracy. The residual values for continuity, momentum, and energy equations were monitored throughout the iterations, with a convergence threshold of 10^{-6} for the energy equation and 10^{-4} for other governing equations. The solution was considered converged when the residuals fell below these limits and when the temperature and velocity fields no longer exhibited significant variations between consecutive iterations.

The representation of the results of solution as well as the flow characteristics and heat transfer, some parameters and variables are needed. For a comprehensive analysis of the thermal and hydrodynamic performance of the mini-channel independent of geometric and operating conditions, key dimensionless parameters are handy.

The Reynolds number is a fundamental parameter that determines the flow regime within the mini-channel. It is defined as [41]:

$$Re=\frac{\rho U D_h}{\mu} \quad (10)$$

For the present study, the entrance velocity and fluid properties define the Reynolds number, which determines whether the flow is laminar (Re<2300), transitional (2300≤Re≤4000), or turbulent (Re>4000).

Since mini-channels often operate near transitional conditions, special care must be taken in selecting appropriate heat transfer correlations.

The Nusselt number quantifies the convective heat transfer enhancement relative to conduction across the fluid. It is given by [42]:

$$Nu = \frac{hD_h}{k} \tag{11}$$

where h is the convective heat transfer coefficient, k is the thermal conductivity, and D_h is the hydraulic diameter calculated by [43]:

$$D_h = 4\frac{A}{P} = \frac{2WH}{W+H} \tag{12}$$

A higher Nu value indicates more efficient convective heat transfer. Turbulent flow conditions require empirical correlations such as Gnielinski's [44] or Petukhov's [45].

For hydrodynamically and thermally developing flow in a duct or channel, Shahand London [12] proposed a correlation for the Nusselt number:

$$Nu = 3.66 + \frac{0.0668 \cdot (D/L) \cdot Re \cdot Pr}{1 + 0.04 \cdot [(D/L) \cdot Re \cdot Pr]^{2/3}} \tag{13}$$

Where Prandtl number is [34]:

$$\mathrm{Pr} = \frac{\mu c_p}{\lambda} \tag{14}$$

Since the mini-channel modeled in this study has micro-scale features, modified correlations are better for accounting for entrance effects, wall roughness, and scale-dependent thermal effects. Another approach is to modify the Gnielinski correlation by interpolating between the laminar and turbulent regimes:

$$Nu = \left(\frac{Nu_{\text{laminar}} + Nu_{\text{turbulent}}}{2}\right) \times \left(1 + \left(\frac{Re - 2300}{4000 - 2300}\right)^2\right) \tag{15}$$

In mini-channels, Nu also depends on surface roughness and flow acceleration effects. Until Coulomb's experiments in 1800, the effect of surface roughness on frictional resistance was not known. Later, Prandtl's student Nikuradse simulated roughness by gluing uniform grains of sand onto walls of pipes, measured pressure drops and flow rates in these pipes, and examined the variation of the coefficient of friction with Reynolds number. According to Nikoradze's results, it can be concluded that flows in the approximate range (Y^+) between 12 and 250 have a strong relationship with the geometry of the channel and the best place to investigate the geometry is in this range. As a result of his investigations, he found that the coefficient of friction is not affected in laminar flow, but in turbulent flow, friction increases with the relative roughness ε/d after a certain initial point and can be calculated as follows [46]:

$$\frac{1}{f^{0.5}} = -2log\left[\frac{\varepsilon/d}{3.7} + \frac{2.51}{Re\, f^{0.5}}\right] \tag{16}$$

The Fanning friction factor, which is used in heat transfer and CFD studies, characterizes the pressure loss due to viscous effects and is defined as [47; 48]:

$$f = \frac{\Delta P D_h}{2\rho U^2 L} \tag{17}$$

For laminar flow, the theoretical friction factor for a smooth duct is:

$$f = 16/Re \tag{18}$$

In turbulent conditions, however, empirical relations such as the Blasius equation apply.

Considering the relative roughness coefficient ε/d and Reynolds number, the effect of surface roughness is not a matter of discussion in the present study. Nonetheless, the corrugation profile on the sidewalls of the mini-channel act as surface roughness, and can cause turbulent flow to occur by strengthening instability in the flow.

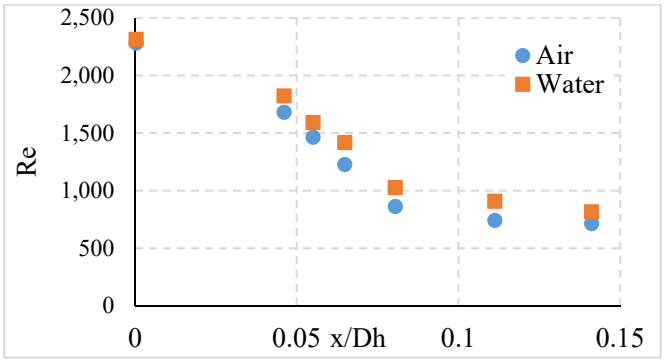

Figure 5. *Effective roughness in the channel*

Figure 5 shows critical Reynolds diagram against normalized channel length. With the help of different results obtained from experimental solutions, it is seen that the more the roughness in the channels, the less Reynolds reaches the turbulent flow. Besides, mini-channels exhibit entrance effects and possible micro-scale flow deviations that also induce turbulence in smaller Reynolds numbers.

As seen in Figure 5, corrugated surfaces can lower the critical Re significantly from about 2300 to some 700 depending on the amplitude, wavelength and shape of the corrugation as well as the type of the fluid and flow geometry.

A validation of numerical results is often necessary due to these mentioned peculiarities of mini-channels.

The pressure drop for the flow in the corrugated mini-channel is:

$$\Delta p = P_{in} - P_{out} = f\frac{(x_e - x_s)\rho u_{in}^2}{2D_h} \tag{19}$$

To assess the combined impact of heat transfer enhancement and pressure drop, the thermal performance factor is used [41; 43]:

$$\eta = \frac{(Nu/Nu_0)}{(f/f_0)^{1/3}} \quad (20)$$

where Nu0, and f0 are the baseline Nusselt number and friction factor for a conventional smooth channel. Thermal performance factor accounts for heat transfer enhancement relative to the increase in pressure drop through comparison across studies by normalizing against a baseline case, typically a smooth channel. This metric is best for comparing channels with different enhancement techniques but similar Reynolds numbers. A value of η>1 indicates that the proposed mini-channel geometry provides an overall thermal improvement.

As stricter version of η, Performance Evaluation Criterion (PEC), which penalizes pressure drop more than η, is also used when comparing energy-efficient cooling solutions across different studies [49; 50]:

$$PEC = \frac{(Nu/Nu_0)}{(f/f_0)} \quad (21)$$

Another metric is Bejan number (Be) which evaluates the heat transfer enhancement against frictional losses. Greater Be indicates greater entropy generation due to friction and hence less efficiency. It is mostly preferred in analyzing heat transfer irreversibility in micro- or mini-channels and is best for comparing cooling strategies in thermodynamic optimization

$$Be = \frac{f}{Re \cdot Pr} \quad (22)$$

For a more flow-sensitive way of evaluation that accounts for both convective heat transfer and pressure drop, Modified Thermal-Hydraulic Factor (Θ) is often preferred to compare studies with different flow conditions or cases where Re varies significantly:

$$\Theta = \frac{Nu}{\sqrt{fRe}} \quad (23)$$

For small-sized thermal systems such as compact heat exchangers, Colburn Factor-to-Friction Factor Ratio (j/f) is used to evaluate heat transfer efficiency per unit pressure drop [34; 51]:

$$\frac{j}{f} = \frac{Nu}{RePr^{1/3}f} \quad (24)$$

3. Results and discussion

This study investigates how turbulence intensity and turbulence length scale affect heat transfer and flow characteristics for different geometries and different flow types using computational fluid mechanics. In many real flows, long and flat surfaces are encountered. Examples of situations where the boundary layer is formed on long and flat surfaces are flow over a ship hull, flow over a submarine hull, flow over aircraft wings, atmospheric flow over flat terrain. The flow characteristics over long and flat surfaces in engineering problems are similar to the flow over a flat plate. Therefore, understanding the flow on a flat plate is important for understanding the flow characteristics on long and flat surfaces in engineering problems.

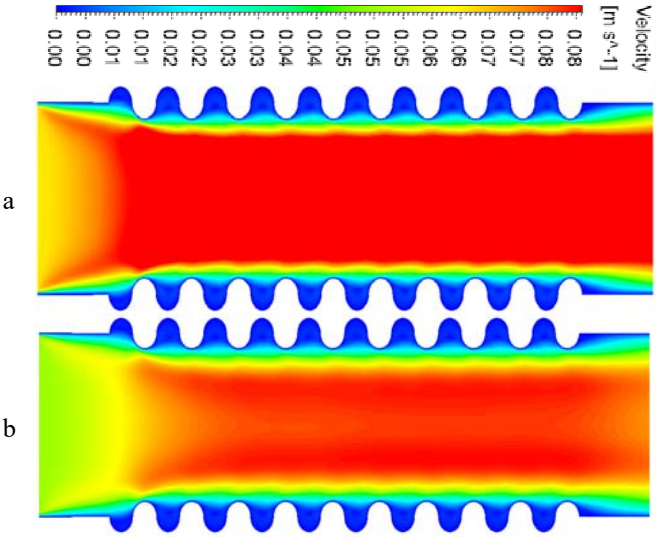

Figure 6. *Turbulent flow velocity profile in the channel at Re 2300 a) air b) water*

The standard k-ε, k-ω, RNG k-ε and SST models are compared among themselves and it can be concluded that the k-ω turbulence model gives better results than the other models, although the RNG k-ε model shows close performance. The velocity profile obtained from the graph for Reynolds 2300 and lambda 1000 micrometer range can be seen as follows. The longitudinal curvature in the velocity contours through the channel can also be seen below.

When the CFD velocity profiles for turbulent flow through the channel, given in Figure 6, are compared for air and water; it is clearly visible that the velocity profile for air shows a high-velocity core region (in red) concentrated in the longitudinal center part of the channel and that the velocity gradually decreases towards the walls, with blue regions indicating low-velocity zones at the pits (valleys) and relatively-higher low-velocity zones at the hills (crests). Flow is relatively uniform in the central region but shows deceleration near the corrugated surfaces, which suggests that the presence of corrugation creates higher resistance to the flow.

The fluid temperature distribution is shown as shown in Figure 7.

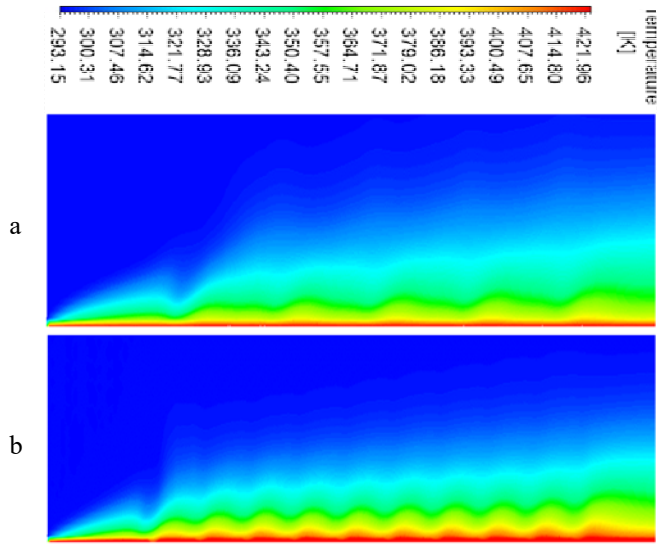

Figure 7. *Fluid temperature distribution through the channel at Re 2300 a) air b) water*

Comparing air and water, the transition of the profile from high- to low-velocity is more gradual for water than air and the deceleration near the walls is less steep than that of air. It is also notable that the effects at the entrance and exit are less pronounced for water and it could maintain a relatively-stable flow profile despite the corrugated surfaces, which indicates that water has a higher momentum due to its greater density and therefore the effect of corrugation on the flow profile is less. Likewise, air is more susceptible to flow disturbances and exhibits sharper gradients due to its lighter density and viscosity as manifested by sharper velocity gradient near the walls.

As seen in Figure 7, the temperature distribution for air shows a high-temperature region near the corrugated wall (in red) and a gradual transition to lower temperatures towards the centerline (in blue). The temperature gradient is steeper in air due to having lower thermal conductivity, lower specific heat capacity, and lower density. Air heats up more rapidly than water and exhibits a steeper temperature gradient which implies rapid cooling of the air as it moves through the channel. The high-temperature zone in water is more extensive and the temperature gradient is gentler due to its higher specific heat capacity, which suggests that water absorbs and distributes heat more uniformly and therefore maintains a higher temperature over a larger area. These findings clearly show the critical importance of fluid properties in determining thermal performance in corrugated channels.

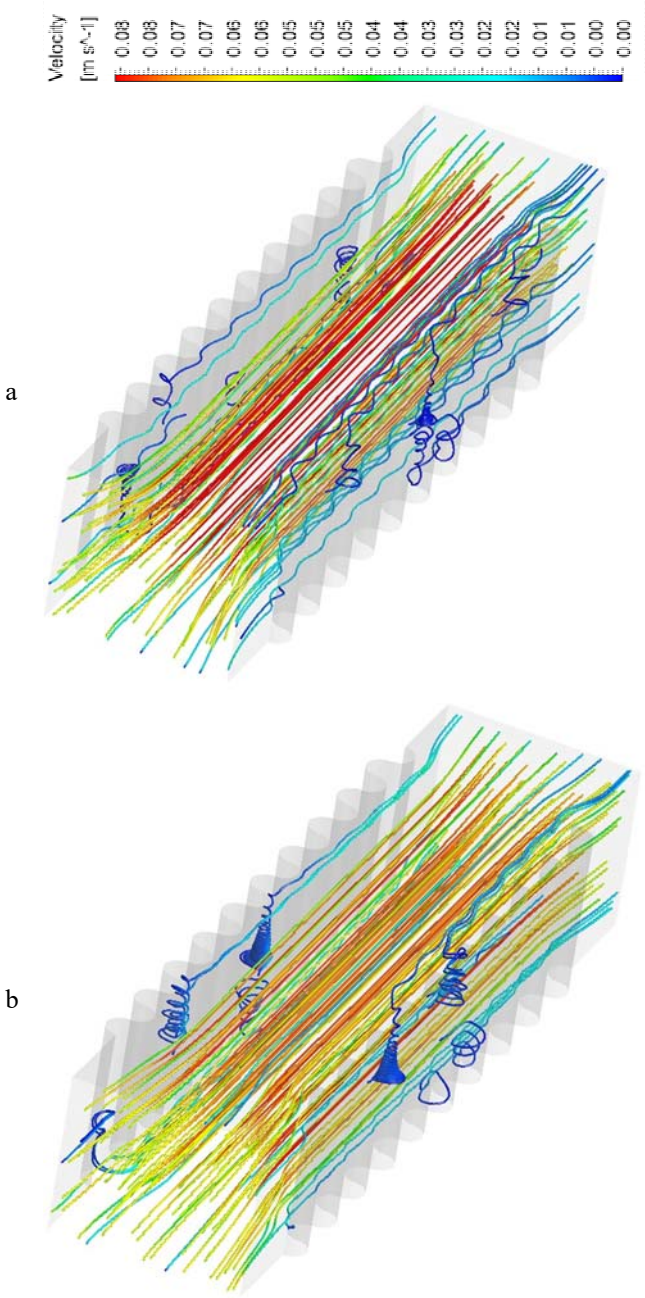

Figure 8. *Streamlines through the channel at Re 2300 a) air and b) water*

The streamlines of flow through the channel, shown in Figure 8, is also important to evaluate the distinct flow behaviors for air and water. With streamlines maintaining a relatively straight path, both fluids exhibit a high-velocity, undisturbed core region (red and yellow) through the central part of the channel. However, near the corrugated walls, both air and water show significant distortion of streamlines and the presence of secondary flow zones with recirculation. These recirculation zones, in blue (lower velocity), indicate areas of

turbulence and mixing induced by the interaction with the corrugated surfaces.

For air flow, the high-velocity core remains largely undisturbed, ensuring efficient flow through the channel's center. However, the interaction with the walls generates vortices and turbulence, which could enhance mixing and heat transfer efficiency but also increase flow resistance. Water flow demonstrates similar characteristics, with a stable high-velocity core and pronounced recirculation zones near the walls. While secondary flows occurred in both air and water, stronger and more complex secondary flow patterns occurred in water due to its higher viscosity and density. While this might seem counterintuitive as air was mentioned above as more susceptible to flow disturbances, higher density leads to stronger inertial forces that contribute to the development of secondary flows and higher viscosity promote secondary flows due to increased shear stresses at the tube walls.

The most important comparison and validation parameter for ducts is the pressure drop. The Reynolds number is 2300 and the results of the pressure drop obtained from ANSYS Fluent are shown as follows

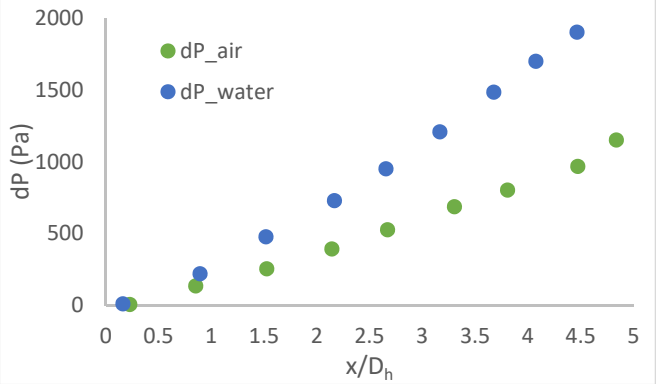

Figure 9. *Variation of pressure drop through the normalized channel length*

Pressure drop increases with the size of wall roughness. As can be seen in Figure 9, the values of pressure drop reaches approximately to 1150 Pa for air and 1900 Pa for water, with an uptrend along the normalized channel length. The pressure drop that water experiences is significantly higher compared to air due to higher density and viscosity of water, which result in greater shear stress, hence greater resistance to flow. The increased pressure drop for water indicates a higher energy requirement for pumping the fluid through the channel, which is an important consideration.

In their smooth walled micro-channel with a D_h of 1mm, Quand Mudawar [6] reported a pressure drop ranging between 0.5 to 1.5 kPa.

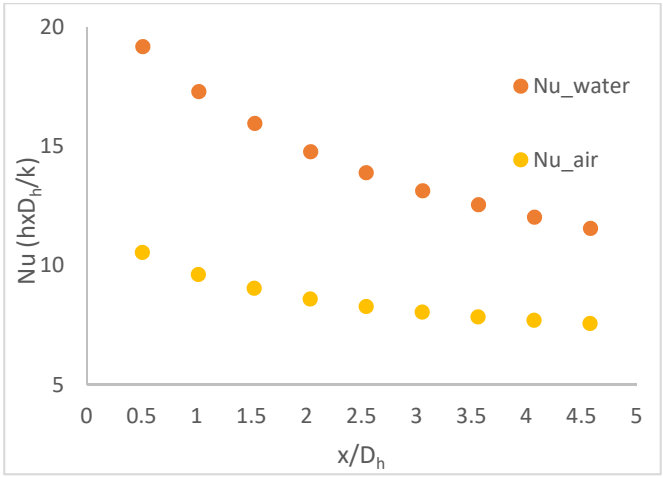

Figure 10. *Variation of Nusselt number through normalized channel length*

From Figures 9 and 10, it can be seen that the Nusselt number for both air and water show a slight decrease along the channel length that corresponds to the gradual increase in the development of flow, decreasing by 28% from about 10.54 to 7.56. While the Nusselt number for water is consistently higher than that for air, ranging from about 19.17 to 11.55, corresponding to a 65% decrease. In the upstream section, both water and air exhibit relatively high Nusselt numbers thanks to the strong convective heat transfer due to thin thermal boundary layer. As the fluid progresses downstream, the Nusselt number gradually decreases as a result of the grow in thermal boundary layer that induce a reduction in the overall heat transfer efficiency. The periodic corrugation along the sidewalls improves heat transfer by disrupting the boundary layer and enhancing local mixing. However, as the flow develops, the influence weakens and Nusselt number approaches to a stable figure.

Comparing the two fluids, water exhibits consistently higher Nusselt numbers than air, which is attributed to its superior thermal conductivity and Prandtl number. Despite this difference in magnitude, both fluids follow a similar trend in heat transfer behavior, suggesting that the enhancement mechanism due to corrugation affects them in a comparable manner. The steeper decline in the Nusselt number near the channel entrance implies that the flow is in the thermal entrance region, where boundary layer development is still in progress. As the normalized channel length increases, the boundary layer thickens, and the flow transitions toward a more thermally developed state, where the Nusselt number stabilizes.

As shown in Figure 11, the Nusselt number and pressure drop data obtained in a rectangular mini channel with corrugated side walls at different Reynolds numbers clearly demonstrate the effects of the flow regime and fluid properties on heat transfer and flow resistance.

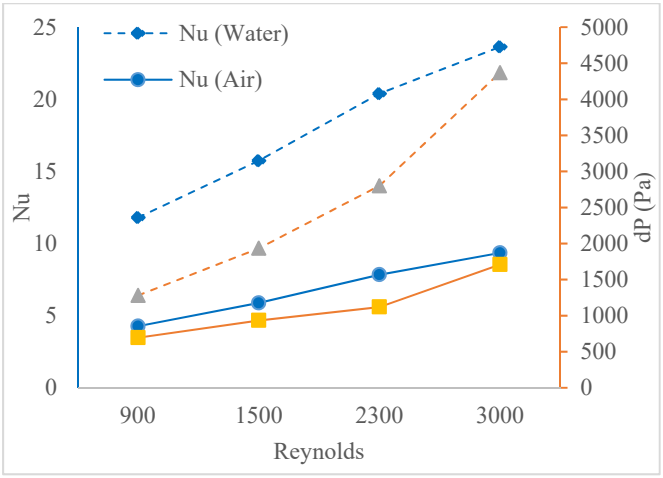

Figure 11. *Variation of Nusselt number through normalized channel length*

The results show that the Nusselt number for both water and air increase significantly with the increase in Reynolds number. This increase can be explained by the thinning of the thermal boundary layer and the strengthening of convective heat transfer due to the intense interaction of the fluid with the channel walls at higher flow rates. Water showed higher Nusselt numbers than air at all Reynolds numbers. This is related to the higher thermal conductivity and Prandtl number of water and shows that the heat transfer capacity of water is more effective than air. On the other hand, the pressure drop for both air and water increased significantly with the increase in Reynolds number. Water causes more pressure loss than air due to its low viscosity and high density. Especially at Re=3000, ΔP for water reaches approximately 4500 Pa, while this value remains around 1800 Pa for air. This situation causes the need for more pumping power in return for the high heat transfer advantage.

As a result, while the heat transfer enhancing effect of the corrugated sidewall structure becomes especially evident at low and medium Reynolds numbers, increased pressure losses at high Reynolds numbers can become a factor that can limit the overall efficiency of the system. Therefore, it is clear that in systems where such structures will be applied, pump costs should be taken into consideration in addition to the targeted cooling performance. In this context, the use of non-dimensional parameters such as performance evaluation criteria (PEC) can provide a balanced optimization of both the thermal and hydraulic efficiency of the system.

The results demonstrated that corrugated sidewalls in mini-channels can be an effective strategy for enhancing convective heat transfer while maintaining an acceptable pressure drop. These findings contribute to the design of high-performance heat sinks for electronic cooling applications, where compact and efficient heat dissipation is crucial.

To ensure the accuracy and reliability of the numerical simulations, the results were compared with experimental and numerical studies in the literature detailed in Table 2. The Nusselt number and pressure drop values were compared with the findings of Karabulut [52] and Sadighi Dizaji et al. [53].

Sadighi Dizaji et al. [53] experimentally investigated the tubes with corrugated surface profile in double pipe heat exchangers. They evaluated the inner and outer tubes as concave and convex separately (Figure 12) and reported that corrugated tubes provide significant increase in the performance of the heat exchanger compared to straight tubes. These results support the findings obtained in our study.

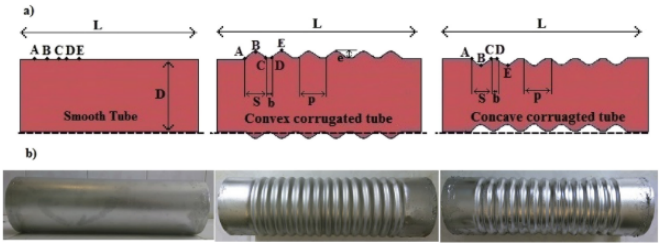

Figure 12. *Smooth and corrugated pipes used in a DPHE [53]*

Both studies examine the effects of surface geometry on heat transfer and flow properties. Both studies show that corrugated surfaces and surface roughness improve heat transfer by increasing flow mixing, but this also significantly increases pressure drop. In this context, both studies emphasize the need to strike a balance between increased heat transfer and pumping power requirements.

When various groove profiles are compared (Figure 13), it is seen that the cylindrical groove geometry maintains high thermal performance coefficients, especially at high Reynolds values.

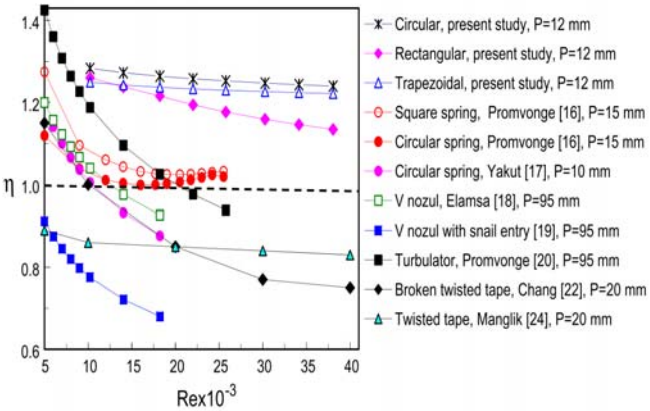

Figure 13. *Thermal performances of various grooved pipes and channels [54]*

Considering Bilen et al. [54] and our study, both investigate the effects of surface geometry on heat transfer and flow properties under turbulent flow conditions. Both studies emphasize the importance of optimizing the balance between

heat transfer enhancement and energy losses and reveal the critical role of surface geometry on thermal performance.

Similarly, the results obtained by Sui et al. [55], who investigated the fluid flow in microchannels with different wave profiles, show that microchannels provide better heat transfer performance compared to straight channels.

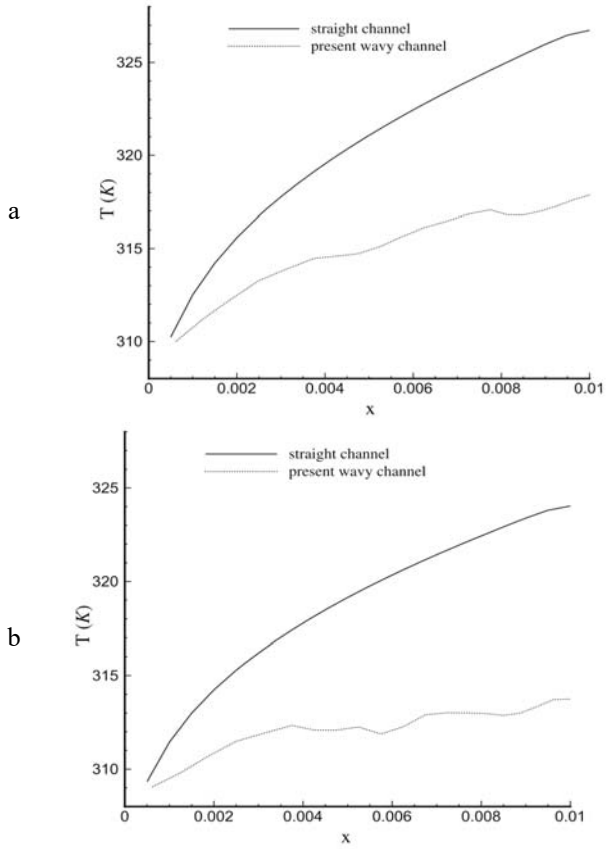

Figure 14. *Temperature distribution along the wavy micro channels (a) Re=300, (b) Re=400 [55]*

Sui et al. [55] and the present study, both of which investigated the effect of surface geometry on heat transfer and flow characteristics in small-scale mini channels, emphasize that optimized surface geometry is a critical design element to improve heat transfer while reducing energy losses. As can be seen in Figure 14, the temperature profile is very similar to what observed in the numerical simulation presented in Figure 14.

Harikrishnanand Tiwari [56] studied the fluid flow in the streamwise and spanwise corrugated channels for fixed channel width and height and compared them in terms of Nu and friction coefficients. The results showed that the turbulent kinetic energy occurs at higher values in the YZ plane in the transverse corrugated channel. (Figure 15).

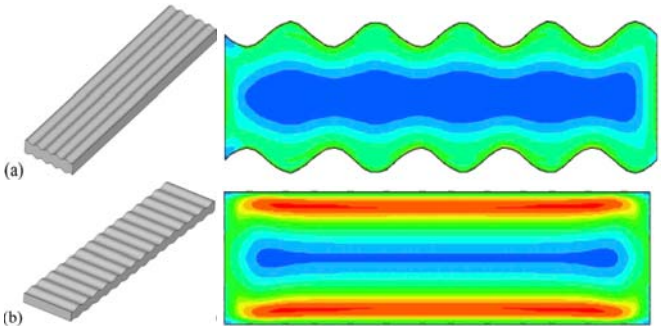

Figure 15. *Turbulent kinetic energy in the YZ-plane in fluid flow in (a) streamwise and (b) spanwise wavy channels [56]*

Harikrishnanand Tiwari [56] also investigated the effects of corrugated surface geometries on flow and heat transfer using numerical methods. Both studies pointed out that the surface geometry increases heat transfer by creating turbulence and secondary flows in the flow field, and emphasized that these geometric arrangements can increase energy efficiency with design optimization.

Begag et al. [57], who investigated the effects of corrugated surfaces on flow and heat transfer with numerical methods, as in the present study, analyzed the heat transfer and pressure drop performance of a channel with trapezoidal-shaped corrugations at different inclination angles under constant heat flux and for turbulent flow. In the present proposed study, the effects of corrugated surface profile and surface roughness on heat transfer and flow characteristics in a rectangular cross-section mini-channel were investigated. Both studies revealed that corrugated surfaces significantly improved heat transfer by increasing turbulence and mixing in the flow field, but this caused a higher pressure drop. It was also emphasized that the surface geometry increased heat transfer through the breaking and destabilization of the thermal boundary layer. These results indicate that the surface geometry should be carefully designed to increase energy efficiency and optimize pumping power requirements.

4. Conclusion

This numerical analysis investigated the impact of a corrugated surface profile on heat transfer and fluid flow characteristics in a turbulent flow through a rectangular mini-channel, considering both air and water as working fluids. The heat transfer characteristics in mini-channels are different from the experimental results of conventional sized channels. In experiments on flow and heat transfer in mini-channels, it is difficult to accurately measure some parameters such as channel dimensions, average roughness, local heat convection, local value of static pressure along the channel, etc. The study comprehensively examined velocity and temperature profiles, streamline patterns, pressure drop, and Nusselt number variations in order to provide a thorough understanding of the flow behavior of these fluids through the channel. By studying the surface roughness, it was observed

that the important effect of this steady flow on local heat transfer can be understood.

The velocity and temperature profiles revealed that both air and water exhibit a high-velocity core with significant deceleration near the corrugated walls. Air showed a more abrupt velocity gradient and pronounced entrance and exit effects due to its lower density and viscosity. In contrast, water maintained a more uniform flow profile and absorbed heat more efficiently due to its higher density and specific heat capacity. Streamline analysis highlighted the formation of vortices and recirculation zones near the corrugated walls for both fluids, with water exhibiting more pronounced turbulence and mixing. These interactions suggest that the corrugated design effectively enhances turbulence and heat transfer, particularly for water. The evaluation of pressure drop and Nusselt number demonstrated that both parameters increase with the size of wall roughness. Water experienced significantly higher pressure drops compared to air, reflecting greater flow resistance due to its physical properties. However, water consistently achieved higher Nusselt numbers, indicating superior heat transfer performance.

In conclusion, the corrugated surface profile enhances heat transfer by promoting turbulence and mixing near the walls. While water provides better heat transfer performance, it also incurs higher pressure drops, necessitating a careful balance between thermal efficiency and energy consumption in practical applications. This study underscores the importance of fluid properties and surface design in optimizing the thermal performance of heat exchangers and similar systems, offering a foundation for future research and development in this field. As a suggestion for the future of this research, other changes in geometry and flow, such as fluid velocity and the height of the inlet and outlet openings of the channel, as well as the use advanced heat transfer fluids or nanofluids, can be used.

References

[1] Pettersen, J., 2004. Flow vaporization of CO2 in microchannel tubes, *Experimental thermal and fluid science*, *28*(2-3), pp.111–121.

[2] Siddique, W., El-Gabry, L., Shevchuk, I.V., Hushmandi, N.B., and Fransson, T.H., 2012. Flow structure, heat transfer and pressure drop in varying aspect ratio two-pass rectangular smooth channels, *Heat Mass Transfer*, *48*(5), pp.735–748.

[3] Kandlikar, S.G., and Upadhye, H.R., 2005. Extending the heat flux limit with enhanced microchannels in direct single-phase cooling of computer chips, *Semiconductor Thermal Measurement and Management IEEE Twenty First Annual IEEE Symposium*.

[4] Tuckerman, D.B., and Pease, R.F.W., 1981. High-performance heat sinking for VLSI, *IEEE Electron device letters*, *2*(5), pp.126–129.

[5] Kandlikar, S.G., 2005. Heat transfer mechanisms in microchannels and their engineering applications, *J. Heat Transfer*, *127*(1), pp.8–16.

[6] Qu, W., and Mudawar, I., 2002. Experimental and numerical study of pressure drop and heat transfer in a single-phase micro-channel heat sink, *International Journal of Heat and Mass Transfer*, *45*(12), pp.2549–2565.

[7] Kandlikar, S.G., and Grande, W.J., 2004. Evolution of microchannel flow passages–thermohydraulic performance and fabrication technology, *Heat Transfer Engineering*, *25*(3), pp.3–17.

[8] Lee, P.S., and Garimella, S.V., 2006. Thermally developing flow and heat transfer in rectangular microchannels of different aspect ratios, *International Journal of Heat and Mass Transfer*, *49*(17-18), pp.3060–3067.

[9] Harley, J., Bau, H., Zemel, J.N., and Dominko, V., 20-22 Feb. 1989. "Fluid flow in micron and submicron size channels", in: *IEEE Micro Electro Mechanical Systems, , Proceedings, 'An Investigation of Micro Structures, Sensors, Actuators, Machines and Robots',* IEEE, pp. 25–28.

[10] Peng, X.F., and Peterson, G.P., 1996. Convective heat transfer and flow friction for water flow in microchannel structures, *International Journal of Heat and Mass Transfer*, *39*(12), pp.2599–2608.

[11] Peng, X.-F., and Wang, B.-X., 1998. "Forced-convection and boiling characteristics in microchannels", in: *International Heat Transfer Conference Digital Library,* Begel House Inc.

[12] Shah, R.K., and London, A.L., 1978. "Rectangular Ducts", in: Shah, R.K., and London, A.L., eds., *Laminar flow forced convection in ducts,* Acad. Pr, New York, pp. 196–222.

[13] Steinke, M.E., and Kandlikar, S.G., 2006. Single-phase liquid friction factors in microchannels, *International Journal of Thermal Sciences*, *45*(11), pp.1073–1083.

[14] Wang, M., Zhang, W., Xin, G., Li, F., Pu, J.H., and Du, M., 2023. Improved thermal–hydraulic performance of a microchannel with hierarchical honeycomb porous ribs, *Can J Chem Eng*, *101*(2), pp.1083–1094.

[15] Flockhart, S.M., Dhariwal, R.S., 1998. Experimental and numerical investigation into the flow characteristics of channels etched in〈100〉 silicon.

[16] Cisneros-Ramírez, C.-A., 2022. Review of the calculation of the boiling heat transfer coefficient in mini-channels and micro-channels, *TSE*, *4*(1), pp.1.

[17] Anwar, M., Tariq, H., Shoukat, A., Ali, H., and Ali, H., 2020. Numerical study for heat transfer enhancement

using CuO water nanofluids through mini-channel heat sinks for microprocessor cooling, *Therm sci*, *24*(5 Part A), pp.2965–2976.

[18] Kadivar, M., Tormey, D., and McGranaghan, G., 2022. CFD of roughness effects on laminar heat transfer applied to additive manufactured minichannels, *Heat Mass Transfer*.

[19] Lin, Y.-L., Shih, T.I.-P., Stephens, M.A., and Chyu, M.K., 2001. A Numerical Study of Flow and Heat Transfer in a Smooth and Ribbed U-Duct With and Without Rotation, *Journal of Heat Transfer*, *123*(2), pp.219–232.

[20] Akbarzadeh, M., Rashidi, S., Karimi, N., and Omar, N., 2019. First and second laws of thermodynamics analysis of nanofluid flow inside a heat exchanger duct with wavy walls and a porous insert, *J Therm Anal Calorim*, *135*(1), pp.177–194.

[21] Al-Hadhrami, L., Griffith, T., and Han, J.-C., 2003. Heat Transfer in Two-Pass Rotating Rectangular Channels (AR=2) With Five Different Orientations of 45 Deg V-Shaped Rib Turbulators, *Journal of Heat Transfer*, *125*(2), pp.232–242.

[22] Herman, C., and Kang, E., 2001. An Experimantal Study of Convective Heat Transfer Enhancement in a Grooved Channel Using Cylindrical Eddy Promoters, *JEH(T)*, *8*(6), pp.353–371.

[23] Alhamid, J., Al-Obaidi, A.R., and Towsyfyan, H., 2022. A numerical study to investigate the effect of turbulators on thermal flow and heat performance of a 3D pipe, *Heat Trans*, *51*(3), pp.2458–2475.

[24] Al-Obaidi, A.R., Alhamid, J., and Hamad, F., 2021. Flow felid and heat transfer enhancement investigations by using a combination of corrugated tubes with a twisted tape within 3D circular tube based on different dimple configurations, *Heat Trans*, *50*(7), pp.6868–6885.

[25] Mezaache, A., Louhichi, K., and Bessaïh, R., 2023. Numerical investigation of mixed convection and entropy production of nanofluid flow in a corrugated channel using a two-phase mixture model, *Heat Trans*, *52*(1), pp.734–758.

[26] Haj Maideen, R.B., and Somu, S., 2020. Design and analysis of double-pipe heat exchanger with new arrangements of corrugated tubes using honeycomb arrangements, *Thermal Science*, *24*(1 Part B), pp.635–643.

[27] Choudhary, P., and Ray, R.K., 2022. MHD natural convection in a corrugated enclosure with discrete isothermal heating, *Heat Trans*, *51*(6), pp.5919–5951.

[28] Sruthi, B., Sasidhar, A., Surendra Kumar, A., and Sahu, M.K., 2021. Comparative analysis of corrugation effect on thermohydraulic performance of double-pipe heat exchangers, *Heat Trans*, *50*(5), pp.4622–4642.

[29] Song, K.-W., and Wang, L.-B., 2013. The Effectiveness of Secondary Flow Produced by Vortex Generators Mounted on Both Surfaces of the Fin to Enhance Heat Transfer in a Flat Tube Bank Fin Heat Exchanger, *Journal of Heat Transfer*, *135*(4).

[30] Kandlikar, S.G., 2005. Characterization of surface roughness effects on pressure drop in single-phase flow in minichannels, *Physics of Fluids*, *17*(10).

[31] Badruddin, I.A., Ahmed N. J., S., Al-Rashed, A.A.A.A., Nik-Ghazali, N., Jameel, M., Kamangar, S., Khaleed, H.M.T., and Khan, T.M.Y., 2015. Conjugate Heat Transfer in an Annulus with Porous Medium Fixed Between Solids, *Transp Porous Med*, *109*(3), pp.589–608.

[32] Tao, W.-Q., 1987. Conjugated Laminar Forced Convective Heat Transfer From Internally Finned Tubes, *Journal of Heat Transfer*, *109*(3), pp.791–795.

[33] Morrison, F.A., 2001. *Understanding rheology,* Oxford University Press, New York, xiii, 545.

[34] Qin, S.-C., Zhang, Y.-C., Jiang, W., Zhang, X.-C., and Tu, S.-T., 2025. Structure optimization and design of zigzag mini-channel for printed circuit heat exchanger, *Applied Thermal Engineering*, *262,* pp.125207.

[35] Patankar, S.V., 1980. *Numerical Heat Transfer and Fluid Flow.tif,* Hemisphere Publishing Corporation, 200 p.

[36] Hinze, J.O., 1967. Secondary Currents in Wall Turbulence, *The Physics of Fluids*, *10*(9), S122-S125.

[37] Zeng, L., Pan, D., Ye, S., and Shao, X., 2019. A fast multiobjective optimization approach to S-duct scoop inlets design with both inflow and outflow, *Proceedings of the Institution of Mechanical Engineers, Part G: Journal of Aerospace Engineering*, *233*(9), pp.3381–3394.

[38] Chen, D., Müller-Eschner, M., Tengg-Kobligk, H. von, Barber, D., Böckler, D., Hose, R., and Ventikos, Y., 2013. A patient-specific study of type-B aortic dissection: evaluation of true-false lumen blood exchange, *Biomedical engineering online*, *12,* pp.65.

[39] Robinson, A., Eastwick, C., and Morvan, H., 2010. "Further Computational Investigations Into Aero-Engine Bearing Chamber Off-Take Flows", in: *ASME Turbo Expo 2010,* ASME, [Place of publication not identified], pp. 209–217.

[40] Bai, G., Armenante, P.M., Plank, R.V., Gentzler, M., Ford, K., and Harmon, P., 2007. Hydrodynamic

investigation of USP dissolution test apparatus II, *Journal of pharmaceutical sciences*, *96*(9), pp.2327–2349.

[41] Noui, Z., Si-Ameur, M., Bessanane, N., Djebara, A., Ibrahim, A., Ishak, M.A.A.B., Ajeel, R.K., and Dol, S.S., 2025. Comparative study of thermohydraulic performance in mini-channel heat sink systems: Multi-objective optimization and exergy considerations, *Case Studies in Thermal Engineering*, *66,* pp.105722.

[42] Karabulut, K., 2024. The effects of rectangular baffle angles and heights on heat transfer and pressure drop performance in cross-triangular grooved rectangular flow ducts, *International journal of heat and fluid flow*, *105,* pp.109260.

[43] Liang, S., Nie, J., Liu, J., Wang, Z., Li, Z., Hu, Z., Yuan, D., Zhang, J., and Feng, Z., 2025. Effect of longitudinal vortex induced by double square wire coils on the hydrothermal performance and entropy generation in the mini-channel heat sink, *Thermal Science and Engineering Progress*, *57,* pp.103162.

[44] Gnielinski, V., 1976. New Equations for Heat and Mass Transfer in Turbulent Pipe and Channel Flow, *International Chemical Engineering*, *16*(2), pp.359–367.

[45] Petukhov, B.S., 1970. Heat Transfer and Friction in Turbulent Pipe Flow with Variable Physical Properties, *Advances in Heat Transfer*, *6,* pp.503–564.

[46] Rhim, Y.C., and White, F.M., 2016. *Fluid mechanics,* McGraw-Hill education, New York, NY, 773 p.

[47] Alkhazaleh, A., Alnaimat, F., and Mathew, B., 2023. Fluid flow and heat transfer behavior of a liquid based MEMS heat sink having wavy microchannels integrating circular pin-fins, *International Journal of Thermofluids*, *20,* pp.100480.

[48] Liu, X., Zhang, H., Wang, F., Zhu, C., Li, Z., Zhao, D., Jiang, H., Liu, Y., and Zhang, Z., 2022. Thermal and hydraulic performances of the wavy microchannel heat sink with fan-shaped ribs on the sidewall, *International Journal of Thermal Sciences*, *179,* pp.107688.

[49] Li, W., Kadam, S., and Yu, Z., 2023. Heat transfer enhancement of tubes in various shapes potentially applied to CO2 heat exchangers in refrigeration systems: Review and assessment, *International Journal of Thermofluids*, *20,* pp.100511.

[50] Ji, W.-T., Fan, J.-F., Zhao, C.-Y., and Tao, W.-Q., 2019. A revised performance evaluation method for energy saving effectiveness of heat transfer enhancement techniques, *International Journal of Heat and Mass Transfer*, *138,* pp.1142–1153.

[51] Mohammed, H.A., Abed, A.M., and Wahid, M.A., 2013. The effects of geometrical parameters of a corrugated channel with in out-of-phase arrangement, *International Communications in Heat and Mass Transfer*, *40,* pp.47–57.

[52] Karabulut, K., 2020. Heat transfer and pressure drop evaluation of different triangular baffle placement angles in cross-corrugated triangular channels, *Therm sci*, *24*(1 Part A), pp.355–365.

[53] Sadighi Dizaji, H., Jafarmadar, S., and Mobadersani, F., 2015. Experimental studies on heat transfer and pressure drop characteristics for new arrangements of corrugated tubes in a double pipe heat exchanger, *International Journal of Thermal Sciences*, *96,* pp.211–220.

[54] Bilen, K., Cetin, M., Gul, H., and Balta, T., 2009. The investigation of groove geometry effect on heat transfer for internally grooved tubes, *Applied Thermal Engineering*, *29*(4), pp.753–761.

[55] Sui, Y., Teo, C.J., Lee, P.S., Chew, Y.T., and Shu, C., 2010. Fluid flow and heat transfer in wavy microchannels, *International Journal of Heat and Mass Transfer*, *53*(13-14), pp.2760–2772.

[56] Harikrishnan, S., and Tiwari, S., 2019. Heat transfer characteristics of sinusoidal wavy channel with secondary corrugations, *International Journal of Thermal Sciences*, *145,* pp.105973.

[57] Begag, A., Saim, R., Öztop, H.F., and Abboudi, S., 2021. Numerical Study on Heat Transfer and Pressure Drop in a Mini-Channel with Corrugated Walls, *Journal of Applied and Computational Mechanics*, *7*(3), pp.1306–1314.